



UNIVERSIDAD
DE MÁLAGA

ESCUELA DE INGENIERÍAS INDUSTRIALES

Departamento de Ingeniería Mecánica, Térmica y de Fluidos

Área de Mecánica de Fluidos

TESIS DOCTORAL

Fundamental aspects of electrospray operations. Applications to the production of microdroplets, nanoparticles and emulsions.

Author: Antonio Jesús Hijano Reyes

Doctoral advisor: Dr. Ignacio González Loscertales

Thesis tutor: Dr. Carlos del Pino Peñas

Ph.D. program: Doctorado en Ingeniería Mecatrónica


MÁLAGA, ESPAÑA
JANUARY 2018





UNIVERSIDAD
DE MÁLAGA

AUTOR: Antonio Jesús Hijano Reyes

 <http://orcid.org/0000-0003-0816-6147>

EDITA: Publicaciones y Divulgación Científica. Universidad de Málaga



Esta obra está bajo una licencia de Creative Commons Reconocimiento-NoComercial-SinObraDerivada 4.0 Internacional:

<http://creativecommons.org/licenses/by-nc-nd/4.0/legalcode>

Cualquier parte de esta obra se puede reproducir sin autorización pero con el reconocimiento y atribución de los autores.

No se puede hacer uso comercial de la obra y no se puede alterar, transformar o hacer obras derivadas.

Esta Tesis Doctoral está depositada en el Repositorio Institucional de la Universidad de Málaga (RIUMA): riuma.uma.es



Agradecimientos

En primer lugar, quiero expresar mi agradecimiento a los compañeros del grupo que ha formado Yflow por todos los conocimientos que he adquirido en su entorno, así como por el ambiente de compañerismo y cooperación que ha reinado durante esta etapa.

En segundo lugar agradecer a mi director de Tesis, Ignacio González Loscertales, su consejo y guía para la realización de la misma, así como por la posibilidad que me ofreció de comenzar la carrera investigadora en un campo tan rico e interesante como el de la electrohidrodinámica. Igualmente ha sido enormemente estimable la ayuda del Profesor Francisco Higuera, de la Universidad Politécnica de Madrid, porque siempre ha sido un referente ante los diferentes desafíos encontrados. Y no puedo olvidarme de mi Tutor, Carlos del Pino, por su apoyo continuo, ni del resto de profesores y compañeros del Área de Mecánica de Fluidos de la Universidad de Málaga.

Agradecer también al Ministerio de Economía y Competitividad el apoyo económico a la línea de investigación a través de los Proyectos No. DPI2010-20450-C03 y No. DPI2013-47372-C02.

No ha sido menos importante la dirección recibida, y la disponibilidad mostrada, por parte de los Profesores Alberto Fernández-Nieves, del *Georgia Institute of Technology* en Atlanta (USA), y Dominique Legendre, del *Institut de Mécanique des Fluides de Toulouse* en Toulouse (Francia), durante las dos estancias realizadas a lo largo del desarrollo de la presente Tesis.

Ha sido también de agradecer la ayuda de Imma Sánchez en el montaje de algunos trabajos de laboratorio para medir la carga eléctrica de las gotas generadas. Así como la ayuda de Eduardo Dueñas en la realización de las figuras con modelos tridimensionales que aparecen en los anexos del presente texto.

Para la realización de las simulaciones numéricas de los Capítulos 3 y 5, han sido primordiales los recursos ofrecidos por el Centro de Supercomputación y Bioinnovación de la Universidad de Málaga.

En último lugar, no puedo menos que manifestar una enorme gratitud hacia mi familia por su apoyo constante.

Abstract

The present Ph.D Thesis investigates the formation of monodisperse droplets from an electrified meniscus of a low viscosity, highly conductive liquid in the periodic electric microdripping regime, termed Axial Spray Mode II by Juraschek & Röllgen (1998).

The meniscus of a highly conductive liquid is attached to the tip of a metallic capillary tube, is fed with a constant flow rate, and is connected to continuous high voltage relative to a flat counterelectrode at a certain distance in front of the tube. Within a certain range of flow rates and in a narrow range of applied voltages, the meniscus sets in the microdripping regime, in which its tip periodically elongates forming a ligament that ultimately detaches as a droplet. This mode produces monodisperse droplets whose diameter depends on the flow rate and may be one tenth of the diameter of the capillary tube.

The process is governed, mainly, by two dimensionless parameters: the dimensionless flow rate, and the electric Bond number. The flow rate, nondimensionalized with the capillary flow rate, is small, and it can be varied by a factor of about 100 within the microdripping regime, whereas the Electric Bond number, which represents the ratio between electrical and capillary stresses, is bound to a narrow range of order unity.

A second type of emission appears in the microdripping regime different from the droplet emitted in each oscillation of the meniscus. From the moment in which the meniscus adopts a quasi-conical shape, in the stage just before the ligament formation, until the ligament detachment from the meniscus in each oscillation, a fine jet is emitted from the tip of the meniscus. This jet breaks to droplets and forms a spray of very small droplets, with a total mass emitted per oscillation that is negligible in comparison with the mass of the main droplet, as long as highly conductive liquids are used. Nevertheless, the electric charge of the droplets in the spray represent almost all the electric charge emitted per oscillation from the meniscus.

An experimental study is done, where high speed video recordings are used to analyze the dynamics of the meniscus, and the electric charge carried by the emitted droplets is measured. At very low flow rates, the period of the meniscus oscillation is of the order of the capillary time. After reaching its maximum elongation, the meniscus recedes with a velocity of the order of the capillary velocity, except for a region around its tip that is pinned by strong electric stresses and develops into a ligament. The life time of this ligament is of the order of its pinch-off time. This condition, together with the condition that the volume of the ligament at detachment should be equal to the volume of liquid injected during a cycle of the oscillation, determines power laws of the dimensionless flow rate for the dimensions of the ligament and the frequency of the oscillation. These power laws fail at higher flow rates, when the ligament's length ceases to be small compared to the tube's diameter, and the life time of the ligament is now of the order of the oscillation period. Then, the balance of dynamic pressure, electric stress and surface tension stress, together with the volume conservation condition and the condition that, according to the experimental results, the electric charge at the ligament surface (which ends up in the detached droplet) is of the order of the Rayleigh's limit charge, determine new power laws for the frequency of the oscillation and ligament size.

Numerical simulations are performed under the assumption of axisymmetric motion of an inviscid liquid of infinite conductivity. The flow of the liquid is then irrotational and the velocity potential satisfies Laplace's equation. The Laplace's equation for the electric potential is also satisfied outside the liquid, and both Laplace equations are solved using boundary

element methods. The numerical results are compared with experimental results, where a highly conductive water solution is used to enforce the equipotential assumption in the simulations. A good agreement between simulations and experiments is found for high values of the flow rate, for which the model captures the dependence of the mean meniscus volume and oscillation frequency with the dimensionless flow rate and the Electric Bond number. However, the numerical results depart from the experiments for low flow rates, when the rounded tip predicted numerically differs from the pointed quasi conical tip observed experimentally, which can not be correctly computed by the model used in the simulations.

To study the potential use of the microdripping regime to generate emulsions, a glass capillary microfluidic device is manufactured, where droplets of ethylene glycol are emitted from the meniscus attached at the tip of a stretched capillary glass tube. An outer flow of silicone oil is used to drive the generated droplets away from the meniscus, in a coflow configuration. And an electric field is created between the meniscus of the inner liquid and a liquid counter-electrode that is used to discharge and collect the generated droplets. In this electro-coflow configuration, a phase diagram of emission regimes is obtained experimentally when the inner and outer flow rates, and the voltage applied to the inner liquid, are swept. For a range of the governing parameters, an emission regime is found that resembles the microdripping regime in air, where droplets are emitted periodically when the elongated tip of the oscillating meniscus detaches. Like in the experiments in air, the frequency of the meniscus oscillation increases linearly with the applied voltage. The outer flow rate is useful to drive away the generated droplets from the meniscus and from the walls of the device, and to form a liquid collector in a counterflow configuration. Nevertheless, the variation of the outer flow rate has little influence on the oscillation frequency of the meniscus, which is mainly controlled by the inner flow rate and the applied voltage. While the oscillation frequency for microdripping in air is of the order of the capillary frequency, in the case of electro-coflow the corresponding oscillation frequencies are two orders smaller than the capillary frequency. This suggests that other stresses must be involved in the process. Estimates of the importance of the viscous stresses due to the outer and the inner liquid suggest that the viscous effect of the outer liquid on the dynamics of the ligament is responsible for slowing down the oscillation frequency, in comparison with what is observed in air. This leads to an estimate of the frequency in terms of the viscosity of the outer liquid, the interfacial tension and the length and diameter of the ligament that provides the correct order of magnitude of the oscillation frequency. Considering the viscous effect of the outer liquid on the ligament dynamics, approximate scaling laws are worked out for the ligament length and width when the inner flow rate increases, assuming that the period of the meniscus oscillation is of the order of the formation time of the ligament, and observing that the frequency of the oscillation scales as a power of the inner flow rate.

In the case of the microdripping regime in air, if the voltage applied to the meniscus is reduced, a pulsed microdripping regime appears, the Axial Spray Mode I of Juraschek & Röllgen (1998), and when the voltage is reduced even more, pointed tips no longer appear on the meniscus surface. In this case, the oscillation of the meniscus is related to such of an electrified pinned droplet, when the flow rate tends to zero. It is numerically studied then, at the end of the present Dissertation, the resonance of electrified and non electrified inviscid pinned droplets that present an infinite electrical conductivity. For the case of pinned droplets with a volume lower than that of a hemisphere pinned to the same surface, we found that the natural frequency of the droplet scales as a power of the volume when the droplet is supported on a flat surface, in a different way than the analytical solutions presented in the literature, which are valid when the droplets are supported on a concave surface. Furthermore, the first natural frequency of sub-hemispheric droplets strongly depends on the supporting surface where they are pinned. When supported on a tube's tip, the tendency of the natural frequency of the droplets when the dimensionless volume tends to zero is a function of the thickness of the tube's wall.

Resumen

En la presente Tesis Doctoral se investiga el proceso que da lugar a la formación y emisión de gotas monodispersas desde un menisco electrificado de un líquido de baja viscosidad y elevada conductividad eléctrica en el régimen de *microdrizzling* eléctrico periódico, conocido como *Axial Spray Mode II* por Juraschek & Röllgen (1998).

El menisco está anclado a la punta de un tubo capilar metálico, y se alimenta con caudal constante de líquido mientras se conecta a un voltaje constante referenciado a un contraelectrodo, conectado a tierra, que está colocado a una cierta distancia de la punta del tubo. Dentro de un cierto rango de caudales, y un estrecho rango de voltajes, la dinámica del menisco se encuadra en el régimen de *microdrizzling*, en el que se establece un movimiento periódico del mismo, donde su punta se alarga formando un filamento que finalmente se desprende, dando lugar a una gota. Este modo de emisión produce gotas monodispersas cuyo diámetro depende del caudal con que se alimenta el menisco, y puede ser de hasta una décima parte del diámetro del tubo capilar.

El proceso está gobernado, principalmente, por dos parámetros adimensionales: el caudal adimensional y el número de Bond Eléctrico. El caudal, adimensionalizado con el caudal capilar, es pequeño aunque puede variarse en tres órdenes de magnitud dentro del régimen de *microdrizzling*, mientras que el número de Bond Eléctrico, que representa el ratio entre esfuerzos eléctricos y capilares, puede solo variarse en un rango estrecho de orden unidad.

Un segundo tipo de emisión aparece en el régimen de *microdrizzling*, diferente de la emisión de la gota a la que da lugar el ligamento estirado. Desde que el menisco adopta una forma cuasiconica, en la etapa anterior a la formación del ligamento, hasta que se desprende la gota del mismo en cada oscilación, se produce una emisión de spray desde la punta del menisco. Este spray supone una emisión despreciable de masa, en el caso de líquidos muy conductores, comparado con la masa de la gota principal emitida, pero sin embargo transporta la mayor parte de la carga eléctrica emitida desde el menisco.

Se realizó un estudio experimental donde se graban vídeos con cámara de alta velocidad para analizar la dinámica del menisco, y se mide, asimismo, la carga eléctrica transportada por las gotas emitidas. Para caudales pequeños el período de las oscilaciones del menisco es del orden del tiempo capilar. Después de alcanzar el menisco su posición más estirada, la base de este retrocede a una velocidad del orden de la velocidad capilar, mientras que la punta permanece en la misma posición por acción del intenso campo eléctrico en esta zona, dando como resultado la formación de un ligamento en la punta del menisco. La vida de este ligamento es del orden de su tiempo de rotura. Esta condición, junto con la condición de que el volumen del ligamento en el momento de la rotura es igual al volumen de líquido inyectado al menisco durante un período de la oscilación, da lugar a diferentes potencias del caudal adimensional con las que escalan el tamaño del ligamento y frecuencia de la oscilación. Estas leyes de escala dejan de ser válidas para caudales elevados, cuando la longitud del ligamento deja de ser pequeña comparada con el diámetro del tubo, y la vida del ligamento es ahora del orden del período de la oscilación del menisco. El equilibrio entre la presión dinámica, esfuerzos eléctricos y esfuerzos de tensión superficial, junto con la condición de conservación de masa, y la condición de que, de acuerdo con los resultados experimentales, la carga eléctrica en la superficie del ligamento (que da lugar a la gota emitida) es del orden de la carga de Rayleigh, determina nuevas potencias del caudal con que escalan la frecuencia de la oscilación y el tamaño del ligamento.

Cuando el menisco se alimenta con un caudal pequeño, dentro del régimen de *microdrizzling*,

el volumen medio del mismo durante un período de oscilación es del orden del cubo del diámetro del tubo capilar donde se encuentra anclado, su frecuencia de oscilación es del orden de la inversa del tiempo capilar, y el ancho y longitud característicos del ligamento que se desarrolla en la punta del menisco, justo antes de la emisión de la gota, escala con potencias del caudal adimensional de $2/7$ y $3/7$, respectivamente. Para caudales mayores las tendencias cambian y al aumentar el caudal el volumen del menisco se incrementa con la raíz cuadrada del caudal, la frecuencia adimensional disminuye como el caudal adimensional elevado a $-1/2$, y el ancho y largo característicos del ligamento justo antes de su desprendimiento del menisco se incrementan ambos como la raíz cuadrada del caudal adimensional.

En el régimen de *microdrizzling* se obtienen experimentalmente gotas de $50 \mu\text{m}$ para meniscos anclados a tubos capilares de $500 \mu\text{m}$. Y si el caudal adimensional es suficientemente pequeño, se emite una única gota por oscilación del menisco y éstas son monodispersas. Si se emplean tubos capilares más pequeños, en torno a las $100 \mu\text{m}$ se pueden producir gotas monodispersas de tamaño inferior a $10 \mu\text{m}$ y a unas frecuencias alrededor de 10.000 gotas por segundo.

El trabajo experimental se completa con simulaciones numéricas, suponiendo el movimiento axilimétrico de un líquido no viscoso infinitamente conductor. El flujo del líquido es irrotacional y el potencial de velocidad satisface, por tanto, la ecuación de Laplace. La ecuación de Laplace para el potencial eléctrico también se satisface en el dominio exterior al líquido, y ambas ecuaciones se resuelven mediante el uso de elementos de contorno. Los resultados numéricos se comparan con los experimentos, donde se usó una solución acuosa muy conductora, lo que justifica las hipótesis de líquido no viscoso e infinitamente conductor. Las simulaciones coinciden razonablemente bien con los resultados experimentales para caudales grandes, en lo que a frecuencias de oscilación del menisco se refiere. Para estos casos se encuentran las mismas tendencias de la frecuencia de oscilación o del volumen medio del menisco respecto del caudal adimensional y el número de Bond Eléctrico. Sin embargo, los resultados numéricos difieren de los experimentales para caudales pequeños, donde la punta redondeada que se obtiene en las simulaciones difiere de la punta cuasi cónica que se observa experimentalmente en la punta del menisco, la cual no puede ser simulada correctamente con el modelo usado.

Para estudiar el potencial uso del régimen de *microdrizzling* para generar emulsiones, se fabrica un dispositivo de microfluídica usando capilares de vidrio, donde se emiten gotas de etilenglicol desde el menisco anclado a la punta estirada de un capilar de vidrio. Se hace uso de un flujo externo de aceite de silicona para conducir las gotas lejos del menisco desde el que se emiten, en una configuración de coflujo. Se crea un campo eléctrico entre el menisco del líquido interior y un contraelectrodo líquido usado para descargar las gotas generadas. En esa configuración de electro-coflujo se realiza un diagrama de fase de los diferentes regímenes de emisión cuando se barren los caudales de los líquidos interior y exterior, así como el potencial eléctrico aplicado al líquido interior. Para un rango de los parámetros que gobiernan el proceso, se encuentra un régimen de emisión parecido al *microdrizzling* en aire, donde se emiten gotas de forma periódica cuando se desprende el ligamento formado en la punta de un menisco oscilante. De la misma forma que en los experimentos en aire, la frecuencia de oscilación del menisco aumenta linealmente con el voltaje aplicado. El caudal exterior se utiliza para llevarse las gotas generadas lejos del menisco y las paredes del dispositivo, así como para formar un colector líquido en una configuración de contraflujo. Sin embargo, la variación del caudal exterior tiene poca influencia en la frecuencia de oscilación del menisco, que está principalmente controlada por el caudal del líquido interior y el voltaje aplicado. Mientras que la frecuencia de oscilación del *microdrizzling* en aire es del orden de la frecuencia capilar, en el caso de electro-coflujo la frecuencia de oscilación es varios órdenes de magnitud inferior a la frecuencia capilar correspondiente. Esto sugiere que otros esfuerzos deben de influir en la dinámica del menisco, diferentes de los que se dan en aire. Estimaciones de la importancia de los esfuerzos viscosos debidos a los líquidos interior y exterior indican que los efectos viscosos del líquido exterior en la dinámica del ligamento, que se forma en la punta del menisco, es responsable de la diferencia de la frecuencia de oscilación respecto de la capilar. Esto conduce a la estimación de una frecuencia de oscilación en términos de la viscosidad del medio exterior, la tensión interfacial, y la longitud y diámetro del ligamento que

proporciona el orden de magnitud adecuado para la frecuencia de oscilación. Considerando el efecto de la viscosidad del líquido exterior en la dinámica del ligamento, se obtienen leyes de escala aproximadas de la longitud y ancho del ligamento cuando el caudal interior aumenta, asumiendo que el período de oscilación del menisco es del orden del tiempo de formación del ligamento, y observando que la frecuencia de oscilación escala como una potencia del caudal interior.

En el caso del régimen de *microdripping* en aire, si se reduce el voltaje aplicado al menisco, éste da lugar a un régimen de *microdripping* pulsado, el *Axial Spray Mode I* de Juraschek & Röllgen (1998); si se sigue reduciendo el voltaje, dejan de producirse emisiones de espray desde la superficie del menisco. En este caso, la oscilación del menisco está relacionada con la resonancia de gotas electrificadas ancladas, cuando el caudal tiene a cero. Se estudia numéricamente, por tanto, al final de la presente Tesis Doctoral, la resonancia de gotas ancladas no viscosas electrificadas y no electrificadas, que presentan una conductividad eléctrica infinita. Para el caso de gotas ancladas con un volumen inferior al de una semiesfera anclada a la misma superficie, se ha encontrado que la frecuencia natural de las gotas escala como una potencia del volumen de la gota cuando la gota está soportada en una superficie plana, de forma diferente a las soluciones analíticas que para tal caso aparecen en la literatura, que son válidas para gotas soportadas en una superficie cóncava. Además, la primera frecuencia natural de gotas sub-hemiesféricas depende fuertemente de la geometría donde se anclan dichas gotas. Cuando están ancladas en la punta de un tubo, la tendencia de la frecuencia natural respecto del volumen depende del espesor de la pared del tubo, cuando el volumen de la gota tiende a cero.

Contents

1	Introduction motivation and outline	1
1.1	Introduction	1
1.1.1	Microdripping regime	1
1.1.2	Generation of emulsions in electro-coflow	3
1.1.3	Droplet's resonance	4
1.2	Motivation	6
1.3	Thesis Outline	6
	References	7
2	Microdripping emissions in air	13
2.1	Introduction	13
2.2	Problem description and experiments	14
2.2.1	Setup and measurement techniques	14
2.2.2	Oscillation regimes	17
2.2.3	Dimensionless variables and results	19
2.3	Results	22
2.3.1	Dimensionless frequency and mean volume	22
2.3.2	Scale disparity. Small q and domain of existence	22
2.3.3	Comments on the tip emission of electrospray	23
2.3.4	Ligament characterization	24
2.3.5	High q trends and droplet diameter	26
2.3.6	Comparisons with other results in the literature	26
2.4	Conclusions	27
	References	28
3	Perfect conductor liquid model simulations	29
3.1	Introduction	29
3.2	Mathematical model	31
3.2.1	Equations	31
3.2.2	Non-dimensionalization	32
3.2.3	Perfect conductor assumption	32
3.2.4	Inviscid liquid assumption	33
3.3	Numerical procedure	33
3.3.1	Global mass conservation, pinch-off condition and tip treatment	34
3.3.2	Electrical and capillary stresses on the meniscus surface	36
3.4	Comparison with experiments	38
3.5	Conclusions and future works	43
	References	45



4	Electro-coflowing emissions	47
4.1	Introduction	47
4.2	Problem description and experiments	48
4.3	Results	49
4.3.1	Phase diagram in electro-coflow	49
4.3.2	Effect of the viscosity of the outer liquid.	52
4.3.3	Oscillatory regime in electro-coflow and comparison with microdripping regime in air	53
4.3.3.1	Time scale of the meniscus oscillations	55
4.3.3.2	Ligament characterization	57
4.4	Conclusions and future works	59
	References	60
5	Resonance of electrified and non electrified pinned droplets	61
5.1	Introduction	61
5.2	Equations	62
5.3	Numerical approach	63
5.4	Experimental setup	65
5.5	Results	66
5.5.1	Vibrations of non-electrified pinned droplets	66
5.5.2	Vibrations of electrified pinned droplets	69
5.6	Conclusions	72
	References	72
6	Conclusions and future work	75
6.1	Conclusions	75
6.2	Future work	77
	References	78
A	Equipment description	79
A.1	Microdripping experiments in air	79
A.2	Coflowing experiments	80
B	Image processing and measurement procedure	83
B.1	Contour detection in images	83
B.2	Subpixel detection algorithm	84
B.3	Region classification	85
B.4	Extraction of characteristics and measurements	88
	References	88
C	Boundary Element Method and validation of the simulations	89
C.1	Laplace's equation for the velocity potential	89
C.2	Laplace's equation for the electric potential	92
C.3	Validation	93
	References	94
D	Adaptive Runge-Kutta method	95
	References	97
E	Resonance frequency of a inviscid droplet pinned to a circle	99
E.1	Non electrified droplets	99
E.2	Electrified droplets	101
	References	102

List of Figures

2.1	Scheme of the experimental setup	14
2.2	Interface tracking for periodic microdripping emission with $\hat{q} = 2.1$ mL/h, $\hat{\phi}_0 = 3.39$ kV, $L = 9$ mm and $D = 500$ μ m.	15
2.3	Detection of the ligament dimensions.	16
2.4	Setup used to measure the droplets electric charge.	17
2.5	Snapshots of the microdripping regime for $\hat{\phi}_0 = 3.39$ kV, $L = 9$ mm and $D = 500$ μ m.	18
2.6	Current recorded at the collector electrode.	18
2.7	Dimensionless mean volume and oscillation frequency respect to dimensionless flow rate.	20
2.8	Dimensionless diameter of the droplet, $d_d = \hat{d}_d/D$, as a function of the dimensionless flow rate for $B_E = 0.20$ (circles), 0.27 (triangles) and 0.37 (squares). The dashed line at the left-hand side has slope $1/3$, and the dashed line at the right-hand side has slope $1/2$	20
2.9	Square of the dimensionless oscillation frequency as a function of the Electric Bond number for $q = 8 \times 10^{-4}$, 2×10^{-3} , 4×10^{-3} , 1.47×10^{-2} and 3.4×10^{-2} , increasing from top to bottom (filled symbols). Empty inverted triangles show data from Fig. 6 of Juraschek et al. 1998 for $q = 1.42 \times 10^{-3}$. The dashed line stands for the expression $f \sim B_E^{3/4}$ proposed by Choi et al. 2008.	21
2.10	Dimensionless electric charge of the droplets, \hat{C}_d/C_R , as a function of B_E for $q = 1.6 \times 10^{-3}$ (circles), 4.1×10^{-3} (squares) and 1.2×10^{-2} (diamonds).	21
2.11	Dimensionless frequency, f , as a function of the mean dimensionless volume of the meniscus in each oscillation, v_M , for $B_E = 0.20$ (circles), 0.27 (triangles) and 0.37 (squares). The dashed line stands for the relation $f v_M \approx 0.32$	22
2.12	Contours of constant q in the (v_M, B_E) plane. Contours shown are for $q = 1.93 \times 10^{-3}$ (circles), $q = 3.86 \times 10^{-3}$ (squares) and $q = 1.43 \times 10^{-2}$ (diamonds), increasing from bottom to top.	23
2.13	Dimensionless length and width of the ligament immediately before detachment as functions of the dimensionless flow rate for $B_E = 0.20$ (circles), 0.27 (squares) and 0.37 (diamonds).	25
3.1	Definition Sketch.	31
3.2	Minimum radius of the neck, r_{min} , prior pinch-off versus the time to pinch-off, $(t_p - t)$ for $q = 4.56 \times 10^{-2}$ and $B_E = 0.2$. The dashed line stands for $r_{min} \sim (t_p - t)^{1/3}$	35
3.3	Dimensionless meniscus profile at different stages during its oscillation for two different flow rates. $B_E = 0.2$ and $B = 6 \times 10^{-2}$	37
3.4	Dimensionless capillary and electric stresses on the meniscus surface just before and after the ligament detachment. $q = 5.79 \times 10^{-2}$, $B_E = 0.2$ and $B = 6 \times 10^{-2}$	37
3.5	Dimensionless capillary and electric stresses on the meniscus surface in different stages during its retraction. $q = 5.79 \times 10^{-2}$, $B_E = 0.2$ and $B = 6 \times 10^{-2}$	38
3.6	Dimensionless capillary and electric stresses on the meniscus surface in different stages during its elongation. $q = 5.79 \times 10^{-2}$, $B_E = 0.2$ and $B = 6 \times 10^{-2}$	38



3.7	Temporal evolution of the meniscus volume and the axial position of the tip for $q = 7.35 \times 10^{-2}$, $B_E = 0.2$ and $B = 6 \times 10^{-2}$. Solid line for experiments and dashed line for simulations.	39
3.8	Temporal evolution of the axial position of the tip for $q = 5.79 \times 10^{-2}$, $B_E = 0.2$ and $B = 6 \times 10^{-2}$. Solid line for experiments and dashed line for simulations. . .	40
3.9	Temporal evolution of the dimensionless velocity of the tip, v_{tip} , in a cycle of the meniscus oscillation for $q = 5.79 \times 10^{-2}$, $B_E = 0.2$ and $B = 6 \times 10^{-2}$. A pentagon symbol indicates the moment at which an electrospray starts to be emitted from the meniscus tip. T is the dimensionless period of the oscillation.	40
3.10	Temporal evolution of the dimensionless velocity of the tip, v_{tip} , in a cycle of the meniscus oscillation for different dimensionless flow rate. Darker solid lines are for higher flow rates, and pentagon symbols indicate the moment at which an electrospray starts to be emitted from the meniscus tip. $B_E = 0.2$ and $B = 6 \times 10^{-2}$. T is the dimensionless period of the oscillation.	41
3.11	Evolution of the dimensionless frequency of the oscillation and the dimensionless mean volume of the meniscus versus the dimensionless flow rate. $B_E = 0.2$ and $B = 6 \times 10^{-2}$	42
3.12	Dimensionless ligament length ℓ_s and ligament mean diameter d_s versus the dimensionless flow rate q . Circles for the experiments and squares for the simulations. $B_E = 0.2$ and $B = 6 \times 10^{-2}$	43
3.13	Equivalent diameter of liquid emission per meniscus oscillation. Circles for the experiments and crosses for the simulations. Squares represent the equivalent diameter of the volume emitted in the main ligament developed in each period. $B_E = 0.2$ and $B = 6 \times 10^{-2}$	44
4.1	Experimental setup in electro-coflow.	49
4.2	Phase diagram of the emissions in electro-coflow for different inner flow rates, \hat{q}_i and voltage applied to the inner liquid, $\hat{\phi}_0$. The outer medium is silicone oil, with a viscosity of 9.3×10^{-3} Pa s. Zone I for electrodrizzling, zone II for oscillating meniscus, and zones III and IV for jet emissions.	50
4.3	Emissions in electro-coflow: electrodrizzling and transition to a oscillating meniscus.	50
4.4	Emissions in electro-coflow: oscillating meniscus and transition to jetting.	51
4.5	Emissions in electro-coflow: Emission of jets.	51
4.6	Phase diagram of the emissions in electro-coflow for different inner flow rates, \hat{q}_i and voltages applied to the inner liquid, $\hat{\phi}_0$. The outer liquid is hexamethyldisiloxane with a viscosity of 0.5×10^{-3} Pa s and the outer flow rate, \hat{q}_o , is 16 mL/h. Zone I for electrodrizzling, zone II for oscillating meniscus, and zones IV and V for jet emissions.	52
4.7	Jetting, zone V. $\hat{q}_o = 16$ mL/h, $\hat{q}_i = 346$ μ L/h, $\hat{\phi}_0 = 800$ V, and $D = 50$ μ m.	53
4.8	Whipping, zone IV. Viscosity of the outer liquid, 0.5×10^{-3} Pa s. $\hat{q}_o = 16$ mL/h, $\hat{q}_i = 346$ μ L/h, $\hat{\phi}_0 = 1000$ V, and $D = 50$ μ m.	53
4.9	Frequency of the meniscus oscillation, \hat{f} , in zone II, versus voltage, $\hat{\phi}_0$, for constant inner flow rate, \hat{q}_i . Different symbols are for different outer flow rates, \hat{q}_o , from 50 μ L/h up to 300 mL/h. The viscosity of the outer liquid is $\mu_o = 9.3 \times 10^{-3}$ Pa s.	54
4.10	Frequency of the meniscus oscillation, \hat{f} , in zone II, versus voltage, $\hat{\phi}_0$, for constant outer flow rate, \hat{q}_o . Different symbols are for different inner flow rates, \hat{q}_i , from 16 μ L/h up to 220 μ L/h. The viscosity of the outer liquid is $\mu_o = 9.3 \times 10^{-3}$ Pa s.	54
4.11	Ligament formation in oscillating meniscus regime, zone II, in electro-coflow. Viscosity of the outer liquid, 9.3×10^{-3} Pa s. $\hat{q}_o = 48$ mL/h, $\hat{q}_i = 188$ μ L/h, $\hat{\phi}_0 = 700$ V, and $D = 50$ μ m.	56

4.12	Ligament formation time, \hat{t}_s , versus inner flow rate, \hat{q}_i . Viscosity of the outer liquid, 9.3×10^{-3} Pa s. $\hat{\phi}_0 = 700$ V, and $D = 50 \mu\text{m}$. Circles for the values measured in the videos, squares for the values from Equation 4.1. The results corresponding to different outer flow rates are represented in this figure, due to the little effect that this flow has in oscillating regimes.	57
4.13	Frequency of the meniscus oscillation, \hat{f} , in zone II, versus inner flow rate, \hat{q}_i for a outer flow rate $\hat{q}_o = 51 \pm 7$ mL/h and outer viscosity $\mu_o = 9.3 \times 10^{-3}$ Pa s. Circles for $\hat{\phi}_0 = 900$ V, squares for $\hat{\phi}_0 = 850$ V, triangles for $\hat{\phi}_0 = 800$ V, and diamonds for $\hat{\phi}_0 = 750$ V. The dashed lines have slope $-1/3$	58
4.14	Length and width of the ligament immediately before detachment as a function of the inner flow rate. $\hat{\phi}_0 = 700$ V, and $D = 50 \mu\text{m}$. The results corresponding to different outer flow rates are represented in this figure, due to the little effect that this flow has in oscillating regimes.	58
5.1	Definition Sketch.	63
5.2	Peaks representing the natural frequencies obtained from the simulations after applying the Fourier transform to the evolution over time of the axial position of the droplet's tip, z_{tip} . This case is for a non-electrified sub-hemispheric droplet of volume $v_{ol} = 1.12$ supported on a tube of wall thickness $e/a = 0.3$	64
5.3	Experimental setup.	65
5.4	Information obtained from high-speed recordings of vibrated droplets.	66
5.5	First dimensionless eigenfrequency versus droplet dimensionless volume of pinned droplets. The solid red line represents analytical solution 5.7 (for l_2) and the dashed lines its trends in the regions where $v_{ol} \rightarrow 0$, $v_{ol} \sim 2$ (hemispherical droplets) and $v_{ol} \gg 1$. Circles indicates the simulations supporting the droplets on a bowl (Strani's geometry) whereas the triangles represents simulations of droplets supported on a flat surface. The frequency is made dimensionless with the capillary time associated to the anchoring radius a . The numbers in (a) corresponds to the cases shown in figure 7.	67
5.6	Evolution of the first dimensionless eigenfrequency versus the droplet dimensionless volume of pinned droplets. Solid red line for simulations of droplets supported on a bowl with $B = 0$, solid green line for simulations of droplets supported on the tip of a tube without thickness and with $B = 0$, solid blue line for simulations of droplets supported on a flat surface and with $B = 0$, solid magenta line for simulations of droplets supported on the tip of a tube with dimensionless thickness $e/a = 0.3$ and with $B = 0$, dashed magenta line for simulations of droplets supported on the tip of a tube with dimensionless thickness $e/a = 0.3$ and with $B = 2.04$, and diamonds for experiments of droplets supported on the tip of a tube with dimensionless thickness $e/a = 0.33$ and with $B = 2.04$	68
5.7	Dimensionless first eigenfrequency versus Electric Bond number and droplet's volume for the first vibration mode, $l = l_2$. For the case of droplets supported on a flat surface.	69
5.8	Deformed interface, solid line, for a droplet supported on a bowl (Strani's geometry), left, and a droplet supported on a flat surface, right. For the case $l = l_2$	71
A.1	Configuration of the inner, outer and collector tubes in the glass microdevices used in the experiments of Chapter 4.	81
B.1	Recorded images of the meniscus and droplet emission during a period of the oscillation in electric microdripping regime for different flow rates.	84

B.2	Contour detection. Tube's outer diameter $D = 500 \mu\text{m}$, flow rate $\hat{q} = 1.0 \text{ mL/h}$, voltage $\hat{\phi}_0 = 2.95 \text{ kV}$, and tube tip to collector distance $L = 9 \text{ mm}$. As a reference, the normalized arc length, s , with values from 0 to 1, is represented (circles) in the images.	85
B.3	Detection subpixel.	86
B.4	Region classification during an oscillation period of the microdripping regime for different flow rates. Region detected as meniscus are marked with white line, those detected as droplet are marked with red line and the regions without interest are marked with green line.	87
B.5	Characteristics extracted from video analysis. Tube's outer diameter $D = 500 \mu\text{m}$, flow rate $\hat{q} = 10 \text{ mL/h}$, voltage $\hat{\phi}_0 = 2.95 \text{ kV}$, and tube tip to collector distance $L = 9 \text{ mm}$	87
C.1	Boundary of the domain discretized with linear elements, where the Laplace equation for the velocity potential is solved.	90
C.2	Discretization.	91
C.3	Domain where the Laplace's equation is solved for the electric potential. Boundary C_2 includes the tube and the interface	92
C.4	Validation. Resonance of free charged droplets.	93
D.1	Simulations flow chart.	96
E.1	Sketch of a droplet of radius R pinned to a circle or radius $a = 1$	100
E.2	Sketch of an electrified droplet of radius R pinned to a circle or radius $a = 1$. . .	102

List of Tables

4.1	Properties of ethylene glycol, Scharlau 99.5 %, and silicone oil 10 cSt, Sigma-Aldrich, at ⁽¹⁾ 20°C, ⁽²⁾ 25°C. Viscosity, μ , density, ρ , and conductivity, K . The interfacial tension between the ethylene glycol and silicone oil is $\gamma = 17.5 \pm 0.4$ mN/m, measured at 20°C.	49
4.2	Properties of Sigma-Aldrich hexamethyldisiloxane 0.65 cSt at ⁽¹⁾ 20 °C, ⁽²⁾ 25 °C. Viscosity, μ , density, ρ , and conductivity, K	52
A.1	List of equipment used in experiments of Chapter 2.	79
A.2	List of equipment used in experiments of Chapter 4.	80





List of Symbols

B_E	Electric Bond number
Re	Reynolds number
B	Bond number
Oh	Ohnesorge number
a	Tube's outer radius, or anchoring radius
D	Tube's outer diameter, or anchoring diameter
L_N	Tube's length
D_i	Tube's inner diameter
\hat{C}_d	Electric charge of the droplet or meniscus
C_d	Dimensionless electric charge of the droplet or meniscus
\hat{C}_s	Surface charge of the droplet or meniscus interface
C_s	Dimensionless surface charge of the droplet or meniscus interface
C_R	Rayleigh limit charge for a droplet
\hat{r}	Radial coordinate of the meniscus interface
r	Dimensionless radial coordinate of the meniscus interface
\hat{z}	Axial coordinate of the meniscus interface
z	Dimensionless axial coordinate of the meniscus interface
\hat{v}_z	Axial velocity of the interface
v_z	Dimensionless axial velocity of the interface
\hat{v}_r	Radial velocity of the interface
v_r	Dimensionless radial velocity of the interface
$\hat{\mathbf{v}}$	Velocity vector of the interface
\mathbf{v}	Dimensionless velocity vector of the interface
\hat{p}	Pressure
p	Dimensionless pressure
R	Radius of the droplet pinned to the tube
\hat{v}_{ol}	Droplet or meniscus volume
v_{ol}	Dimensionless volume of the droplet or meniscus
γ	Interfacial tension
μ	Viscosity
K	Electrical conductivity
ρ	Density
ϵ_0	Dielectric permittivity of vacuum
ϵ	Relative permittivity
t_e	Electrical time
t_c	Capillary time
v_c	Capillary velocity
q_c	Capillary flow rate

\hat{f}	Frequency of meniscus/droplet oscillation
f	Dimensionless frequency of meniscus/droplet oscillation
\hat{q}	flow rate
q	Dimensionless flow rate
T	Period of meniscus/droplet oscillation
\hat{t}	Time
t	Dimensionless time
n	Oscillation mode of the droplet
$\hat{\phi}_0$	Voltage applied to the droplet or meniscus
$\hat{\phi}_e$	Electric potential
ϕ_e	Dimensionless electric potential
$\hat{\phi}$	Velocity potential
ϕ	Dimensionless velocity potential
g	Gravity
\mathbf{n}	Normal vector to the interface
\mathbf{T}_e	Maxwell tensor
\hat{k}_u	Local curvature of the interface
k_u	Dimensionless local curvature of the interface
$\hat{\mathbf{E}}$	Electric field
\mathbf{E}	Dimensionless electric field
\hat{E}_n	Normal electric field
E_n	Dimensionless normal electric field
E_c	Characteristic electric field
\hat{v}_n	Normal velocity to the interface
v_n	Dimensionless normal velocity to the interface
\hat{v}_s	Tangential velocity to the interface
v_s	Dimensionless tangential velocity to the interface
\hat{s}	Arc length
s	Dimensionless arc length
θ	Slope angle of a tangent to a given point of the interface
\hat{d}_d	Diameter of the emitted droplet
d_d	Dimensionless diameter of the emitted droplet
\hat{v}_M	Mean volume of the meniscus per oscillation
v_M	Dimensionless mean volume of the meniscus per oscillation
\hat{l}_s	Meniscus ligament length
l_s	Dimensionless length of the meniscus ligament
\hat{d}_s	Meniscus ligament width
d_s	Dimensionless width of the meniscus ligament
\hat{v}_d	Velocity of the emitted droplet
v_d	Dimensionless velocity of the emitted droplet
\hat{I}	Electric current
H	Length of the meniscus
\mathbf{I}	Identity matrix
ϕ_c	Characteristic velocity potential
ϕ_{ec}	Characteristic electric potential
$\hat{\rho}_e$	Volumetric charge density
ρ_e	Dimensionless volumetric charge density
D_f	Diffusion coefficient of electric charges
$\hat{\mathbf{J}}$	Current density
\mathbf{J}	Dimensionless current density
k_B	Boltzmann constant

m_e	Ions' mobility
z_e	Charge of the ions
G	Green function
C_1	Boundary of the domain where is solved the Laplace's equation for the velocity potential
C_2	Boundary of the domain where is solved the Laplace's equation for the electric potential
\hat{q}_i	Flow rate of the inner liquid
\hat{q}_o	Flow rate of the outer liquid
\hat{q}_{col}	Flow rate of the collector liquid
B_E^{cr}	Critical Electric Bond number

Chapter 1

Introduction motivation and outline

Contents

1.1	Introduction	1
1.1.1	Microdripping regime	1
1.1.2	Generation of emulsions in electro-coflow	3
1.1.3	Droplet's resonance	4
1.2	Motivation	6
1.3	Thesis Outline	6
	References	7

1.1 Introduction

This thesis tries to add light on some aspects of the electro-hydrodynamic atomization (EHD) that are relevant to processes that require the generation of monodisperse droplets, in the micron size regime, in a host media that may be a gas or vacuum, or a liquid, but avoiding the use of micron sized nozzles, tubes or holes. In particular, this work focuses in regimes where an electrified meniscus anchored to a tube oscillates periodically that, for the appropriate parametrical range, in each oscillation it emits a single droplet, substantially smaller than the diameter of the tube holding de oscillating meniscus. Therefore, the body of the manuscript considers different problems where oscillating, electrified meniscus are involved. Those are described in what follows.

1.1.1 Microdripping regime

Atomization of liquid menisci by means of electric fields has been known for a long time. The evolution of the meniscus interface during this breaking process (and so its outcome) may be quite different depending on the values of the liquid properties, electric field strength, etc., a circumstance that has led to the classification of the electro-hydrodynamic (EHD) atomization in different modes. Comprehensive reviews of the main modes have been given by Cloupeau et al. 1994 and by Jaworek et al. 1999. The former considers modes appearing in situations where the liquid is continuously fed at a constant rate to a meniscus attached at the tip of a capillary tube. Possibly, the most studied mode among these is the so-called steady cone-jet, in which a meniscus subjected to an intense electric field adopts a conical shape from whose tip a very thin, highly charged, steady liquid jet is issued. The breakup of this jet yields a spray of highly charged droplets. The success of this particular mode came across when Fenn et al. 1989 discovered that this simple process provides a means to transfer very large ions from the liquid to the gas phase, making them suitable for their posterior weighting in a mass spectrometer. However, the interest on cone-jet electrosprays was already ignited before, when it was realized



that this mode allows the generation of monodisperse sprays of droplets whose diameter bear no relation with the diameter of the meniscus. The study of the cone-jet electrospray (Fernández de la Mora 2007) led to the conclusion that, as the liquid electric conductivity increases, the liquid flow rate has to be decreased and the droplet size decreases as well. Quantitatively, liquids with moderate conductivities, in the order of 10^{-3} S/m, produce monodisperse droplets in the size range of a few microns, whereas liquids with larger conductivities, in the order of 1 S/m or above, yield monodisperse droplets in the nanometer range, regardless of the size of the capillary tip. This is a very interesting option to generate ultrafine monodisperse droplets. Therefore, the potential applications of cone-jets as a monodisperse particle generator have been focused into the sub-micron and nanometric size ranges (Wang et al. 2012; Larriba et al. 2011; Miao et al. 2002).

There are, however, numerous technological applications in which the droplets, although monodisperse in size, do not need to be so small. A typical example is printing, where the droplet size is in the range of 20–100 μm , see Basaran et al. 2013 for a recent review, but there are many others. Combinatorial chemistry, micro-mixing or micro-tritiation (Schober et al. 1993; Tisone 1998; Litborn et al. 1998) already focus on monodisperse drop-on-demand systems that yields micron sized droplets, where the small volumes of the same and the rapid dispensing capabilities make possible an efficient and rapid testing of tens of thousands of mixtures in very short times. Not only that, but performing reactions in airborne microdrops reduces potential contamination from substrates. Analytical tools, such as MALDI TOF spectroscopy, also benefit from using microdroplets, not just by saving the use of very expensive compounds but also from the increase in sensitivity brought about when small volumes of samples are used (Allmaier 1997; Kling 2001). Biotechnology is also an active area in which microdrops play a very important role. Already commercially available systems for sorting cells are based on generation of drops of some 10 to 20 microns in diameter, the size needed to contain a single cell (Hulett et al. 1969). Bio-analysis based on interactions with tagged DNA fragments also require the use of very small volumes of dissolutions containing the DNA fragments, a very expensive material, something made through generation of microdrops (Gabriel 1999; Theriault et al. 1999; Englert 2000). The same requirements apply in drug discovery experiments for medical applications (Schober et al. 1993; Tisone 1998), without forgetting the direct delivery through lung deposition via monodisperse aerosols of droplets with diameters between 3 and 5 microns. Other applications include optics (Cox et al. 2000a,b), where the microdrops are used as lenses themselves, manufacturing of complex composite solids, such as directional asymmetric metal-ceramic matrices (Gao et al. 1994; Ashley 1995), direct soldering (Wallace 1989; Hayes et al. 2001, 1999; Orme et al. 2000), thin film coatings and many more.

Almost all of the technologies operating in industry to produce droplets in this size range resort to hydrodynamic processes where the liquid is forced through a hole with a similar diameter. The forcing stimulus is typically a thermally formed bubble or a piezoelectrically driven moving wall. EHD atomization might be an alternative, but the modes so far reported in the literature either yield monodisperse droplets that are too small, particularly if the liquid is highly conductive, or produce droplets in the right range of sizes but with a size distribution that is too broad (Udey et al. 2013; Steijn et al. 2013; Patrascioiu et al. 2011). It would be interesting to look for an EHD mode that might fulfill both requirements: size and size distribution, maybe relaxing the requirement of using holes of similar sizes.

Attempts at using EHD for printing have been focused in the so called microdripping regime, in which the electrified meniscus oscillates and emits certain amounts of mass and charge in each oscillation. The first study, by Juraschek et al. 1998, relates to unsteady modes that may appear while trying to setup steady cone-jets. For a given liquid flow rate, as the voltage increases they identify two pulsating axial modes, I and II, before reaching the steady cone-jet mode, the axial mode III. Briefly, in mode I the meniscus undergoes bursts of fast pulsed emissions (KHz) at rather low frequencies (tens of Hz), whereas in mode II the emissions are periodic and proceed at much higher frequencies (tens of KHz). Although Juraschek et al. 1998 do not refer explicitly to the microdripping regime, their axial mode II corresponds with the microdripping regime when

a liquid with a high electrical conductivity is used, according to their experiments.

For the sake of clarity, it is important to note that the regime termed microdripping might differ depending on the authors. Jaworek et al. 1999 defined as microdripping the pulsating regime in which the electrified meniscus of a highly conducting liquid oscillates and, in each oscillation, its tip develops a short ligament (with a length of the order of its diameter) that eventually detaches to form a droplet whose diameter is much smaller than that of the tube from which the meniscus hangs; during a certain part of the oscillation a fine jet of electro-spray is emitted from the meniscus tip. On the other hand, they termed spindle regime that in which ligaments much larger were formed. Cloupeau et al. 1994 also used the term spindle for the cases in which large ligaments were stretched out from the meniscus, although they called microdripping a regime that they observed with a liquid of a low electrical conductivity in which no electro-spray were emitted from the oscillating meniscus as droplets were formed. The main motivation to study the microdripping regime in the present thesis is because of its particular feature of producing one droplet per meniscus oscillation, with a diameter much smaller than the tube. We shall see that this occurs when the flow rate feeding the meniscus is low enough to produce short ligaments, so throughout this thesis the term microdripping regime is understood as defined by Jaworek et al. 1999).

More recent investigations of pulsating Taylor cones have been carried out by Marginean et al. 2006a, Chen et al. 2006, and Choi et al. 2008, who proposed different scaling laws for the pulsation frequency and the masses delivered, while Marginean et al. 2007 introduced a classification of axial modes based on three periodic and stationary regimes interspersed with two chaotic regimes. Kim et al. 2008, Kang et al. 2011 and Lee et al. 2012 achieved improved control of the size and emission frequency of the droplets by using pulsed electric fields, and partially classified the new dripping modes that appear in these conditions. Further steps toward the practical implementation of these techniques for high speed and drop-on-demand EHD printing have been taken by Mishra et al. 2010 and Sutanto et al. 2012.

Many of the works mentioned here are based on the periodic emission of a single liquid jet from the electrified meniscus. This jet is unstable under varicose disturbances and breaks into drops whose diameter is similar to that of the jet. This type of emission is useful for direct printing, that is, for applications in which the flowing jet lands on a spot on the target before breaking into droplets, thus forming a single drop of a given volume. However, if the objective is to form drops that must remain airborne for a later use, such as in material forming processes, this type of microdripping is seldom useful. A recent use of EHD to generate nanodroplets for printing of nanostructures is that of Galliker et al. 2012, where micron-sized nozzles were used to eject monodisperse droplets, with diameters between 80 and 100 nanometers, of a colloidal suspension of gold nanoparticles. At landing on a substrate, the volatile solvent evaporated thus leaving a dense residue formed by a compact agglomeration of the gold nanoparticles. As nanodroplets were continuously landing/evaporating on the same spot tiny nanopillars, made of agglomerated gold nanoparticles, could be formed. Although these authors could not follow the droplet formation dynamics, their experiments undoubtedly demonstrate that the periodic EHD microdripping can be used to generate monodisperse nano-sized droplets from nozzles some 10 to 15 times larger in diameter. Finally, the microdripping regime can be used to produce microdroplets when relatively low conductive liquids are used (electrical conductivities around 1×10^{-6} S/m) by special nozzle designs, such that described by Lee et al. 2008, or by the combined use of conductive liquids, such that used by Larriba et al. 2011, thus broadening the potential classes of liquids that may be used.

1.1.2 Generation of emulsions in electro-coflow

The generation of emulsions has numerous interesting applications (Basaran 2002; Barrero et al. 2007), such as in medical and pharmaceutical technology, where emulsions have been widely used for the administration of drugs or as a vehicle for vaccines to control infectious diseases (Gallier-Beckley et al. 2015). Other fields of applications includes the encapsulation of materials or the

generation of oil-water emulsions, for example in agriculture (Li et al. 2013; ElShafei et al. 2010), cosmetic (Glampedaki et al. 2014; Krasodomaska et al. 2015) and food industries (Galus et al. 2015; Jiménez-Colmenero 2013).

Different techniques, based on hydrodynamic forces implemented in microfluidic devices, can be found in the literature to generate emulsions (Basaran 2002), such as coaxial coflow (Castro-Hernández et al. 2009), selective withdrawal techniques (Cohen 2001) or hydrodynamic flow focusing (Calvo et al. 2001), microfluidic techniques (Stone et al. 2004) or mechanical disruption, as well as different combinations among them (Castro-Hernández et al. 2011). These techniques have demonstrated their effectiveness in producing emulsions of droplets or bubbles of tens of microns, although for the case of droplets it is rather difficult to attain sizes of few microns or slightly below, except by using fluids with very high viscosity to pull the liquid to be atomized. This comes, however, with a high cost of pumping.

Electrical forces can be also used to generate emulsions and capsules (Barrero et al. 2004; Alexander 2008), (Chen et al. 2005)). Recently, Gundabala2010 (Guerrero et al. 2014), developed a glass-based microfluidic setup for combining hydrodynamic (i.e. coflow) and electric forces capable of forming, for the first time, steady electrosprays inside a microfluidic channel. This new process, termed electro coflow by their discoverers, allows reducing notably the size of the droplets of the disperse phase inside the continuous one with no need of extra pumping. Therefore, it results a very attractive alternative to produce emulsions of monodisperse droplets whose size may be tailored between tens of microns and submicronic, with the advantage of the confinement of being run in a microfluidic device (Guillot et al. 2007).

Microfluidic devices can be generally classified as PDMS devices or glass capillary devices, attending to the material or fabrication process, or as microfluidic junctions or microfluidic chips devices (Vladislavljević 2015), depending on its geometry or number of circuits. In the case of PDMS devices, liquid PDMS, poly(dimethylsiloxane), is poured over a silicone wafer with a positive photolithographed version of the microfluidic circuit that serves as mold, and afterwards, once cured, the channels in the PDMS are sealed with a flat glass surface (Castro-Hernández et al. 2011). This technique offers a fast way to fabricate microfluidic devices, but the manufacture of the photolithographed silicone wafer is usually rather expensive. On the other hand, glass-based devices are made by inserting a glass tube, with a diameter in the millimeter range whose tip have been stretched down to a diameter of some tens of microns, inside another glass tube, such that different, immiscible liquids may flow through each of these tubes. Such couples of tubes are combined in different geometries to form the desired flow structures. These glass-based microfluidic devices are very cheap to fabricate, although they requires longer manufacturing times that PDMS devices. Nevertheless, they are very appropriate for a rapid design at almost no cost.

1.1.3 Droplet's resonance

The two previous sections consider the existence of an oscillating electrified menisci that emits mass and charge. However, electrified meniscus also exhibit oscillatory modes with no emission, so this problem will also be treated in Chapter 5 of this thesis.

The resonance of free droplets has been studied since the works of Rayleigh 1879 and Kelvin 1890 more than a century ago. They obtained an analytical expression for the natural frequency of inviscid droplets in free space. Later, Lamb 1932 extended the expression for the oscillation of free droplets inside an outer liquid under the assumptions of zero gravity and negligible viscous effects,

$$f^2 = \frac{1}{4\pi^2} \frac{n(n-1)(n+1)(n+2)}{(n+1) + n\rho_0/\rho}, \quad (1.1)$$

where ρ and ρ_0 are, respectively, the density of the inner and outer liquid, n is the oscillation mode, and f the different natural frequencies of the droplet, non-dimensionalized with the

capillary time referred to the droplet radius R . In other works (Prosperetti 1980 and Miller et al. 1968) studied the effect of viscosity on the resonance of free droplets.

For the case of constrained droplets there are numerous experimental works in the literature. Among them, Noblin et al. 2004 studied the oscillation of pinned sessile droplets as well as droplets with mobile contact line. They also highlighted the analogy between the oscillation of pinned droplets and the stationary wave on the surface of a liquid bath. By expanding the velocity potentials in series of Legendre polynomials, Strani et al. 1984 made an analytical study for the case of the oscillation of inviscid droplets supported by a solid bowl inside an outer inviscid liquid. And then, they complemented the work by considering viscous effects (Strani et al. 1988). Bostwick et al. 2009 extended the work of Strani et al. related to inviscid droplet oscillations with the difference that in the case of Bostwick et al. the droplet was pinned to a circle. They obtain the natural frequency of the droplet numerically truncating the eigenvalue problem using spectral methods. Celestini et al. 2006 studied the resonance of vibrated supported droplets in a direction parallel to the substrate, and established an analogy with a simple oscillator, obtaining a semi-analytical expression for the eigenfrequency and a scaling law for the dissipation energy.

For the case of the resonance of charged droplets, it was Rayleigh 1882 who first studied the effect of electric charge in the resonance of inviscid free droplets, considered as perfect conductor, incorporating a term to Equation 1.1 when there is no outer medium,

$$f^2 = \frac{1}{4\pi^2} (n(n-1)(n+2) - B_E n(n-1)), \quad (1.2)$$

where $B_E = \hat{C}_s^2 R / (\epsilon_0 \gamma)$ is the Electric Bond number, R the droplet's radius, γ the surface tension, \hat{C}_s the surface charge, and the oscillation frequency is nondimensionalized with the capillary time $t_c = \rho R^3 / \gamma$.

Rayleigh stated that the natural frequency decreases when the charge of the droplet increases until the Rayleigh limit is reached $C_R = \sqrt{8\pi(\epsilon_0 \gamma R^3)}$, in which case the frequency of the fundamental mode, $n = 2$, is $f = 0$ and the droplet become unstable. It is in this limit when pointed tips appears on the surface of the droplet giving rise to the emission of fine jets which eventually break into charged droplets to form a spray. This phenomena, which can be observed both in electrified droplets and electrified meniscus, was then studied by Taylor 1964 who particularly looked at the effect of electric fields on free space elongated droplets and soap films, as well as jet emissions from electrified meniscus (Taylor 1969). Different experimental studies, in which different methods are used to levitate the droplets, have confirmed the Rayleigh theory for the resonance of inviscid free droplets. In a more recent work, Hill et al. 2010 levitate diamagnetic water droplets using magnetic fields and they compare the frequency of resonance of the first seven modes with the Rayleigh theory. In a later paper, Hill et al. 2012 performed a similar work, but in this case they levitate electrically charged droplets.

The effect of charge relaxation was studied when Saville 1997 simulated the resonance of dielectric droplets in an insulating fluid making use of the leaky dielectric model, and imposing conservation of interfacial charge. Saville stated that for the case of droplets with a moderate viscosity inside an inviscid medium the Rayleigh criterion, Equation 1.2, continues being valid even in the cases in which charge relaxation is slow, although the damping rate is altered.

The resonance of electrified or charged pinned droplets was studied by Basaran and others for conducting (Basaran et al. 1990) and dielectric (Wohlhuter et al. 1992) sessile droplets when an electric field is created between two parallel plates. They studied the equilibrium shape and the limit of stability when the electric field is increased numerically, using Finite Element Methods, and experimentally, using soap bubbles. More specifically, the aspect ratio of the elongated droplets when the electric field increases was studied. Starting with hemispherical droplets, and increasing then the electric field, when the critical electric field was reached beyond which the droplet became unstable, they reported numerically and experimentally an aspect ratio of about 1.84. For dielectric droplets Wohlhuter et al. 1992 found a narrow parametrical range where hysteresis appears, so unstable droplets were reported for a range of electric fields and aspect

ratios. Ramos et al. 1994 also studied the limit of stability of dielectric droplets inside a dielectric medium between two parallel plates extending the works of Basaran et al., and including the case of fixed contact angle.

More recent works relating the stability of electrified sessile or pendant drops refer to the dynamic response to a sudden change in the electric potential applied to low conductivity droplets (Acero et al. 2013), the study of the droplet shape when an AC electric field is applied (Tran et al. 2011) or the influence of separation between plates on the elongation of the droplets (Tsakonas et al. 2014).

The study of the stability of pinned electrified droplets is of interest for applications such as electrowetting, the handling of droplets or cells, mass spectrometry, or printing. Roux et al. 2008 analyzed the non-wetting conditions of conducting droplets in a dielectric liquid pinned to a hydrophobic substrate to force the lift of the droplets. Vancauwenberghe et al. 2013 stated how electrified sessile drops can be used to enhance the evaporation rate through effects on contact angle and equilibrium shape when electric fields are used. In another application, Ren et al. 2010 used and electrified sessile droplet submerged inside a black liquid as an optical switch in which light pass through the system droplet-plates when an electric field is applied.

1.2 Motivation

The previous section mentioned some problems related to electrified oscillating meniscus whose understanding might contribute to technological applications, this being the motivation of the present thesis. Therefore, part of this thesis will be devoted to the investigation, experimental and numerical, of the electric periodic microdripping process in air of low viscosity, high electrical conductivity liquids, that produce a single droplet per oscillation, such that the droplet is substantially smaller than the typical size of the oscillating meniscus. The main object of this part is to obtain and understand the effect of the controlling parameters on the outcome, mainly on the droplets size and on the oscillation frequency. Also, glass capillary devices, similar to those described by Gundabala et al. 2010 and Utada et al. 2005, will be built to experimentally study the different regimes of EHD that appear in electro coflow in situations where the electric forces are dominant in the atomization process. Special attention will be paid to those modes in which oscillating electrified menisci appear, as potential candidates to generate monodisperse emulsions. The final part of this thesis will be devoted to the modeling of the oscillation of pinned non-electrified and electrified droplets of inviscid and highly conducting liquids. In particular, the effect on their oscillation frequencies of the shape of the solid holding the droplet will be investigated, as well as the effect of the electrode configuration in the case of electrified pinned droplets.

1.3 Thesis Outline

The present document is organized as follows. In Chapter 2 the electric microdripping regime, termed as Axial spray mode II by Juraschek et al. 1998, is studied experimentally for a highly conductive, low viscosity, water solution. A tube-plate configuration is used to generate the electric field by connecting the metallic tube to a continuous high voltage. The meniscus of the liquid at the tube's tip is fed through the tube at a constant flow rate. In these conditions, the dynamics of the meniscus and droplet emission are characterized by means of dimensional analysis. High speed recordings and computer video processing are crucial for the observation and analysis of the different stages that occur along each period of the meniscus oscillation. Oscillation frequency and droplet size are thus characterized as a function of the controlling parameters for the microdripping regime.

A numerical approach to the microdripping regime is performed in Chapter 3, assuming an inviscid perfect conductor liquid. The Laplace's equations for the velocity potential and for

the electric field are solved, respectively, inside and outside the liquid domain using Boundary Element Methods discretizing the boundary with linear elements and considering a constant potential in each element. A tube-plate configuration similar to that of the experiments is used to generate the electric field. The interface is advanced in time using an adaptive Runge-Kutta method where the step size is changed to maintain bounded the estimated local error of the numerical method. The numerical results are compared with the experimental results. The limits of the model are discussed.

In Chapter 4 the possibilities of generating emulsions using the microdripping regime are explored. Series of experiments are run within a glass microfluidic device to generate the emulsions in a coflow configuration. A liquid collector acts as counter electrode, in a configuration like that used by Gundabala et al. 2010, discharging and collecting the generated droplets. A phase diagram of the different emission regimes is also performed for different ranges of the controlling parameters. Some features of the oscillating regimes are explained using order of magnitude estimates.

The resonance of electrified and non electrified pinned droplets has been treated in Chapter 5. The same numerical scheme used to simulate the microdripping regime have been used to follow the time evolution of inviscid, and perfect conductor droplets, pinned to a surfaces with different shapes, once initially perturbed. The first natural frequency of the droplets is obtained after applying a Fourier Transformation to the position of a point of its surface. The results of uncharged droplets are compared with experiments for the case of sub-hemispherical droplets.

Finally the conclusions of the present dissertation are summarized in Chapter 6.

References

- Acero, A. et al. 2013. Experimental analysis of the evolution of an electrified drop following high voltage switching. *Eur. J. Mech. B* 38, 58–64.
- Alexander, M. S. 2008. Pulsating electro spray modes at the liquid-liquid interface. *Appl. Phys. Lett.* 92(14), 144102.
- Allmaier, G. 1997. Picoliter to nanoliter deposition of peptide and protein solutions for matrix-assisted laser desorption/ionization mass spectrometry. *Rapid Commun. Mass Spectrom.* 11, 1567–1569.
- Ashley, S. 1995. Rapid prototyping is coming of age. *Mech. Eng.* 117, 62–68.
- Barrero, A. & Loscertales, I. G. 2007. Micro- and nanoparticles via capillary flows. *Annu. Rev. Fluid Mech.* 39, 89–106.
- Barrero, a. et al. 2004. Steady cone-jet electro sprays in liquid insulator baths. *J. Colloid Interface Sci.* 272(1), 104–108.
- Basaran, O, Gao, H, & Bhat, P. 2013. Nonstandard inkjets. *Annu. Rev. Fluid Mech.* 45(1), 85–113.
- Basaran, O. A. 2002. Small-scale free surface flows with breakup: Drop formation and emerging applications. *AIChE Journal* 48(9), 1842–1848.
- Basaran, O. A. & Scriven, L. 1990. Axisymmetric shapes and stability of pendant and sessile drops in an electric field. *J. Colloid Interface Sci.* 140(1), 10–30.

- Bostwick, J. B. & Steen, P. H. 2009. Capillary oscillations of a constrained liquid drop. *Phys. Fluids* 21(3), 032108.
- Calvo, A. M. GAÑÁN & Gordillo, J. M. 2001. Perfectly monodisperse microbubbling by capillary flow focusing. *Phys. Rev. Lett.* 87(27), 274501.
- Castro-Hernández, E. et al. 2009. Scaling the drop size in coflow experiments. *New J. Phys.* 11(7), 075021.
- Castro-Hernández, E. et al. 2011. Microbubble generation in a co-flow device operated in a new regime. *Lab on a Chip* 11(12), 2023–2029.
- Celestini, F. & Kofman, R. 2006. Vibration of submillimeter-size supported droplets. *Phys. Rev. E: Stat., Nonlinear, Soft Matter Phys.* 73(2006), 1–6.
- Chen, C. H., Seville, D. a., & Aksay, I. a. 2006. Scaling laws for pulsed electrohydrodynamic drop formation. *Appl. Phys. Lett.* 89(12), 2005–2007.
- Chen, X. et al. 2005. Spraying modes in coaxial jet electrospray with outer driving liquid. *Phys. Fluids* 17(3), 032101.
- Choi, H. K. et al. 2008. Scaling laws for jet pulsations associated with high-resolution electrohydrodynamic printing. *Appl. Phys. Lett.* 92(12), 2006–2009.
- Cloupeau, M. & Prunet-Foch, B. 1994. Electrohydrodynamic spraying functioning modes: a critical review. *J. Aerosol Sci.* 25(6), 1021–1036.
- Cohen, I. 2001. Using Selective Withdrawal to Coat Microparticles. *Science* 292(5515), 265–267.
- Cox, W. R. et al. 2000a. “Micro-jet printing of refractive microlenses”. *OSA Diffractive Optics and Micro-Optics Topical Meeting, Kailua-Kona, Hawaii.*
- Cox, W. R. et al. 2000b. Microjet printing of micro-optical interconnects. *Int. J. Microcircuits Electronic Packaging* 23, 346–352.
- ElShafei, G. M. et al. 2010. Environmentally friendly pesticides: Essential oil-based w/o/w multiple emulsions for anti-fungal formulations. *Industrial Crops and Products* 31(1), 99–106.
- Englert, D. 2000. Production of microarrays on porous substrates using noncontacting piezoelectric dispensing. *Microarray Biochip Technology*, 231–246.
- Fenn, J. B. et al. 1989. Electrospray ionization for mass spectrometry of large biomolecules. *Science* 246, 64–71.
- Fernández de la Mora, J. 2007. The Fluid Dynamics of Taylor Cones. *Annu. Rev. Fluid Mech.* 39(1), 217–243.
- Gabriel, G. C. 1999. Microarrays: Existing and evolving genomic platforms. *Biomed. Prod.* 10, 26.
- Gallier-Beckley, A et al. 2015. Characterization of a novel oil-in-water emulsion adjuvant for swine influenza virus and Mycoplasma hyopneumoniae vaccines. *Vaccine* 33(25), 2903–2908.

- Galliker, P. et al. 2012. Direct printing of nanostructures by electrostatic autofocussing of ink nanodroplets. *Nat. Commun.* 3(May), 890.
- Galus, S. & Kadzińska, J. 2015. Food applications of emulsion-based edible films and coatings. *Trends in Food Science & Technology* 45(2), 273–283.
- Gao, F. Q. & Sonin, A. A. 1994. Precise deposition of molten microdrops: The physics of digital microfabrication. *Proc. R. Soc. London A* 444, 533–554.
- Glampedaki, P. & Dutschk, V. 2014. Stability studies of cosmetic emulsions prepared from natural products such as wine, grape seed oil and mastic resin. *Colloids Surf., A* 460, 306–311.
- Guerrero, J. et al. 2014. Whipping of electrified liquid jets. *Proc. Natl. Acad. Sci. U.S.A.* 111(38), 13763–13767.
- Guillot, P. et al. 2007. Stability of a jet in confined pressure-driven biphasic flows at low Reynolds numbers. *Phys. Rev. Lett.* 99(10), 104502.
- Gundabala, V. R., Vilanova, N., & Fernández-Nieves, A. 2010. Current-Voltage characteristic of electrospray processes in microfluidics. *Phys. Rev. Lett.* 105(October), 1–4.
- Hayes, D. J., Wallace, D. B., & Cox, W. R. 1999. “Microjet printing of solder and polymers for multi-chip modules and chip-scale packages”. *Proceedings IMAPS 99, Chicago*.
- Hayes, D. J., Cox, W. R., & Grove, M. E. 2001. Low-cost display assembly and interconnects using ink-jet printing technology. *J. Society Information Display* 9, 9–13.
- Hill, R. & Eaves, L. 2010. Vibrations of a diamagnetically levitated water droplet. *Phys. Rev. E: Stat., Nonlinear, Soft Matter Phys.* 81(5), 056312.
- Hill, R. & Eaves, L. 2012. Shape oscillations of an electrically charged diamagnetically levitated droplet. *Appl. Phys. Lett.* 100(11), 114106.
- Hulett, H. et al. 1969. Cell sorting: automated separation of mammalian cells as a function of intracellular fluorescence. *Science* 166, 747–749.
- Jaworek, a. & Krupa, A. 1999. Classification of the modes of EHD spraying. *J. Aerosol Sci.* 30(7), 873–893.
- Jiménez-Colmenero, F. 2013. Potential applications of multiple emulsions in the development of healthy and functional foods. *Food research international* 52(1), 64–74.
- Juraschek, R. & Röllgen, F. 1998. Pulsation phenomena during electrospray ionization. *Int. J. Mass Spectrom.* 177, 1–15.
- Kang, D. K. et al. 2011. Electrohydrodynamic pulsed-inkjet characteristics of various inks containing aluminum particles. *J. Aerosol Sci.* 42(10), 621–630.
- Kelvin, L. 1890. *Mathematical and physical papers.* 3, 384.
- Kim, J., Oh, H., & Kim, S. S. 2008. Electrohydrodynamic drop-on-demand patterning in pulsed cone-jet mode at various frequencies. *J. Aerosol Sci.* 39(9), 819–825.

- Kling, J. 2001. MALDI chip shot. *Anal. Chem.* 73, 68A–70A.
- Krasodomska, O. & Jungnickel, C. 2015. Viability of fruit seed oil O/W emulsions in personal care products. *Colloids Surf., A* 481, 468–475.
- Lamb, H. 1932. *Hydrodynamics*. Cambridge University Press, Cambridge, England.
- Larriba, C. & Fernández de la Mora, J. 2011. Production of monodisperse submicron drops of dielectric liquids by charge-injection from highly conducting liquids. *Phys. Fluids* 23(10), 102003.
- Lee, M. W. et al. 2012. A study of ejection modes for pulsed-DC electrohydrodynamic inkjet printing. *J. Aerosol Sci.* 46, 1–6.
- Lee, S. et al. 2008. Pole-type ground electrode in nozzle for electrostatic field induced drop-on-demand inkjet head. *Sensors Actuators A: Physical* 141, 506–514.
- Li, Y., Chen, P.-S., & Huang, S.-D. 2013. Water with low concentration of surfactant in dispersed solvent-assisted emulsion dispersive liquid–liquid microextraction for the determination of organochlorine pesticides in aqueous samples. *J. Chromatogr., A* 1300, 51–57.
- Litborn, E., Stjernström, M., & Roeraade, J. 1998. Nanoliter titration based on piezoelectric drop-on-demand technology and laser-induced fluorescence detection. *Anal. Chem.* 70, 4847–4852.
- Marginean, I., Nemes, P., & Vertes, A. 2007. A stable regime in electrosprays. *Phys. Rev. E* 76, 026320.
- Marginean, I. et al. 2006a. How much charge is there on a pulsating Taylor cone? *Appl. Phys. Lett.* 89(6), 064104.
- Miao, P., Balachandran, W., & Xiao, P. 2002. Formation of ceramic thin films using electrospray in cone-jet mode. *IEEE Trans. Ind. Appl.* 38(1), 50–56.
- Miller, C. a. & Scriven, L. E. 1968. The oscillations of a fluid droplet immersed in another fluid. *J. Fluid Mech.* 32(03), 417.
- Mishra, S. et al. 2010. High-speed and drop-on-demand printing with a pulsed electrohydrodynamic jet. *J. Micromech. Microeng.* 20, 095026.
- Noblin, X., Buguin, a., & Brochard-Wyart, F. 2004. Vibrated sessile drops: Transition between pinned and mobile contact line oscillations. *Eur. Phys. J. E* 14(4), 395–404.
- Orme, M. et al. 2000. Electrostatic charging and detection of nonconventional droplet streams formed from capillary stream breakup. *Phys. Fluids* 12, 2224–2235.
- Patrascioiu, A et al. 2011. Liquids microprinting through a novel film-free femtosecond laser based technique. *Appl. Surf. Sci.* 257(12), 5190–5194.
- Prosperetti, A. 1980. Free oscillations of drops and bubbles: the initial-value problem. *J. Fluid Mech.* 100(02), 333.

- Ramos, A & Castellanos, A. 1994. Equilibrium shapes and bifurcation of captive dielectric drops subjected to electric fields. *J Electrostat* 33(1), 61–86.
- Rayleigh, L. 1882. XX. On the equilibrium of liquid conducting masses charged with electricity. *Philos. Mag.* 14(87), 184–186.
- Rayleigh, L. 1879. “On the capillary phenomena of jets”. *Proc. R. Soc. London*. Vol. 29. 196–199, pp. 71–97.
- Ren, H. & Wu, S.-T. 2010. Optical switch using a deformable liquid droplet. *Opt. Lett.* 35(22), 3826–3828.
- Roux, J. M., Achard, J. L., & Fouillet, Y. 2008. Forces and charges on an undeformable droplet in the DC field of a plate condenser. *J Electrostat* 66(5), 283–293.
- Saville, D. A. 1997. ELECTROHYDRODYNAMICS: The Taylor-Melcher Leaky Dielectric Model. *Annu. Rev. Fluid Mech.* 29(1962), 27–64.
- Schober, A. et al. 1993. Accurate high-speed liquid handling of very small biological samples. *BioTechniques* 15, 324–329.
- Steijn, V. VAN et al. 2013. Block-and-break generation of microdroplets with fixed volume. *Biomicrofluidics* 7(2), 1–8.
- Stone, H. A., Stroock, A. D., & Ajdari, A. 2004. Engineering flows in small devices: microfluidics toward a lab-on-a-chip. *Annu. Rev. Fluid Mech.* 36, 381–411.
- Strani, M. & Sabetta, F. 1988. Viscous oscillations of a supported drop in an immiscible fluid. *J. Fluid Mech.* 189, 397–421.
- Strani, M. & Sabetta, F. 1984. Free vibrations of a drop in partial contact with a solid support. *J. Fluid Mech.* 141, 233.
- Sutanto, E. et al. 2012. A multimaterial electrohydrodynamic jet (E-jet) printing system. *J. Micromech. Microeng.* 22(4), 045008.
- Taylor, G. 1969. Electrically Driven Jets. *Proc. R. Soc. London A* 313(1515), 453–475.
- Taylor, G. 1964. “Disintegration of water drops in an electric field”. *Proc. R. Soc. London A*. Vol. 280. 1382. The Royal Society, pp. 383–397.
- Theriault, T. P., Winder, S. C., & Gamble, R. C. 1999. Application of ink-jet printing technology to the manufacture of molecular arrays. *DNA Microarrays: A Practical Approach*, 101–119.
- Tisone, T. C. 1998. Dispensing systems for miniaturized diagnostics. *IVD Technology* 4, 40–46.
- Tran, S. B. Q. et al. 2011. Semianalytical study of hemispherical meniscus oscillation with an anchored edge on a conductive flat plate under an ac electric field. *Phys. Fluids* 23(2), 022006.
- Tsakonas, C. et al. 2014. Electric field induced deformation of hemispherical sessile droplets of ionic liquid. *J Electrostat* 72(6), 437–440.

- Udey, R. N., Jones, A. D., & Farquar, G. R. 2013. Aerosol and Microparticle Generation Using a Commercial Inkjet Printer. *Aerosol Sci. Technol.* 47(4), 361–372.
- Utada, A. et al. 2005. Monodisperse double emulsions generated from a microcapillary device. *Science* 308(5721), 537–541.
- Vancauwenberghe, V., Di Marco, P., & Brutin, D. 2013. Wetting and evaporation of a sessile drop under an external electrical field: A review. *Colloids Surf., A* 432, 50–56.
- Vladislavljević, G. T. 2015. Recent advances in the production of controllable multiple emulsions using microfabricated devices. *Particuology*.
- Wallace, D. B. 1989. Automated electronic circuit manufacturing using ink-jet technology. *Trans. ASME J. Electronic Packaging* 111, 108–111.
- Wang, Y. et al. 2012. Electrospray cone-jet breakup and droplet production for electrolyte solutions. *Europhys. Lett.* 99(6), 64003.
- Wohllhuter, F. K. & Basaran, O. A. 1992. Shapes and stability of pendant and sessile dielectric drops in an electric field. *J. Fluid Mech.* 235, 481–510.

Chapter 2

Microdripping emissions in air

Contents

2.1	Introduction	13
2.2	Problem description and experiments	14
2.2.1	Setup and measurement techniques	14
2.2.2	Oscillation regimes	17
2.2.3	Dimensionless variables and results	19
2.3	Results	22
2.3.1	Dimensionless frequency and mean volume	22
2.3.2	Scale disparity. Small q and domain of existence	22
2.3.3	Comments on the tip emission of electrospray	23
2.3.4	Ligament characterization	24
2.3.5	High q trends and droplet diameter	26
2.3.6	Comparisons with other results in the literature	26
2.4	Conclusions	27
	References	28

2.1 Introduction

The generation of identical droplets of controllable size in the micrometer range is a problem of much interest owing to the numerous technological applications of such droplets. This work reports an investigation of the regime of periodic emission of droplets from an electrified oscillating meniscus of a liquid of low viscosity, and high electrical conductivity, attached to the end of a capillary tube, which may be used to produce droplets more than ten times smaller than the diameter of the tube. To attain this periodic microdripping regime, termed axial spray mode II by Juraschek et al. 1998, liquid is continuously supplied through the tube at a given constant flow rate, while a DC voltage is applied between the tube and a nearby counter electrode. The resulting electric field induces a stress at the surface of the liquid that stretches the meniscus until, in certain ranges of voltage and flow rate, it develops a ligament that eventually detaches forming a single droplet, in a process that repeats itself periodically. While it is being stretched, the ligament develops a conical tip that emits ultrafine droplets, but the total mass emitted is practically contained in the main droplet.

In the parametrical domain studied, the process depends mainly on two dimensionless parameters, the flow rate nondimensionalized with the diameter of the tube and the capillary time, q , and the Electric Bond number B_E , which is a nondimensional measure of the square of the applied voltage. The problem also depends on others dimensionless numbers like the Bond number, B , and the Ohnesorge number, Oh , that represent, respectively, the effect of gravity and



the liquid's viscosity, and their role is negligible due to the small size of the tube's diameter and the low viscosity of the liquid used; different geometrical relations are not considered because the geometry is maintained fixed in the experiments. At the minimum flow rate compatible with the periodic regime, the diameter of the droplets is smaller than one tenth of the tube diameter, which opens a way to use electro-hydrodynamic atomization to generate droplets of highly conducting liquids in the micron-size range, in marked contrast with the cone-jet electrospray whose typical droplet size is in the nanometric regime for these liquids. In contrast with other microdripping regimes where the mass is emitted upon the periodic formation of a narrow capillary jet, the present regime gives one single droplet per oscillation, except for the almost massless ultrafine aerosol emitted in the form of an electrospray.

2.2 Problem description and experiments

2.2.1 Setup and measurement techniques

The microdripping of the liquid has been studied in the experimental setup sketched in Fig. 2.1. A long capillary tube of stainless steel (outer diameter D) is placed vertically at a certain distance (L) in front of a circular metallic plate. Unless otherwise is noted, the dimensions of the tube used are outer diameter $D = 500 \mu\text{m}$, inner diameter $200 \mu\text{m}$, length 20 mm . The tube-to-collector distance is $L = 20 \text{ mm}$, and the radius of the collector is 31.5 mm . The liquid to be atomized is supplied at a known flow rate (\hat{q}) by a syringe pump. A constant voltage ($\hat{\phi}_0$) is applied between the metallic tube and the plate by means of a high voltage power supply. The time evolution of the meniscus sticking out of the capillary tube is recorded by a high speed camera with an optical system with magnification from $2.3 \mu\text{m}/\text{pixel}$ up to $12.5 \mu\text{m}/\text{pixel}$, and the image is monitored in a tv-screen. The electric current at the collector plate is measured as the voltage difference across a shunt resistor, logged with a data acquisition card, and the meniscus is illuminated by using a fiber optic illuminator with 4 mm flexible fiber optic light guide.

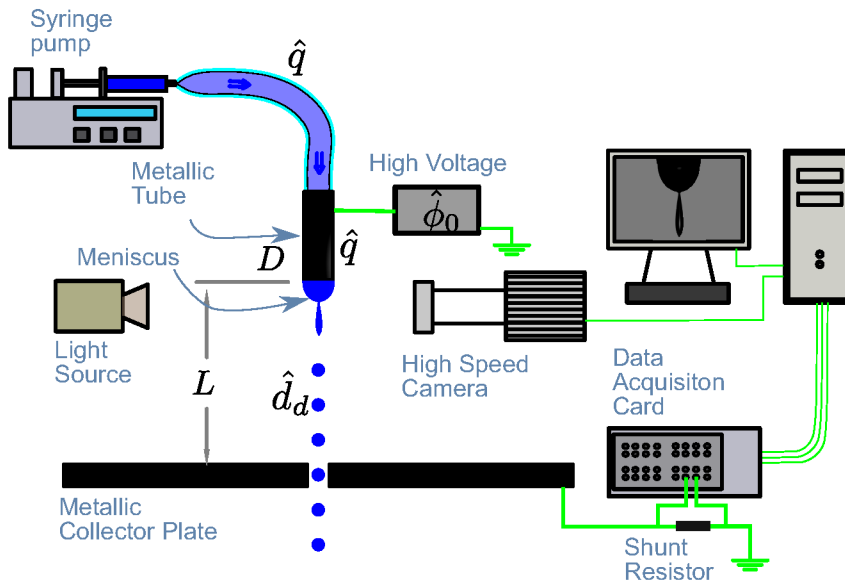
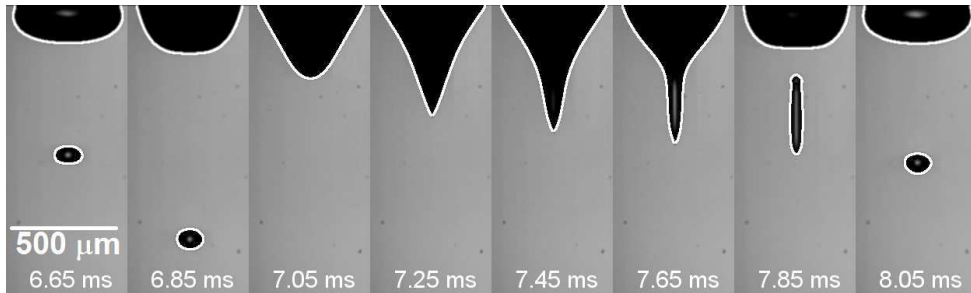


Figure 2.1: Scheme of the experimental setup

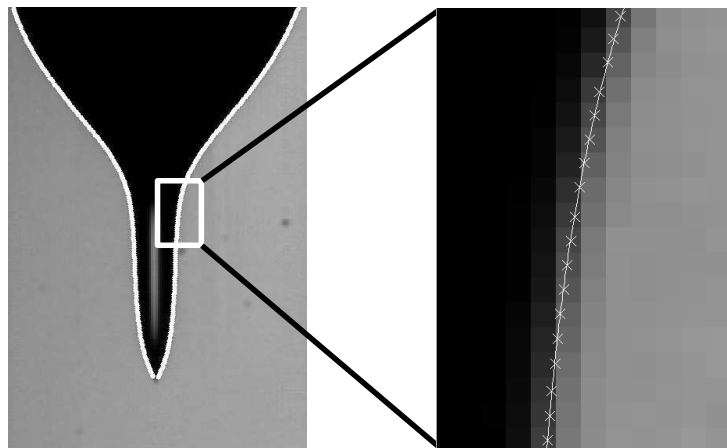
The liquid used is a mixture of 64 % water, 11 % ethanol and 25 % ethylene-glycol, with 1.7 mg/g hydrochloric acid. Unless otherwise is stated, the properties of the liquid, measured at 25°C , are as follows. The surface tension is $\gamma = 41.4 \pm 0.4 \text{ mN/m}$, measured with a ring

tensiometer. The electric conductivity is $K = 4.1 \pm 0.7$ mS/cm, measured with a conductimeter. Both surface tension and conductivity are measured before each experiment, and the uncertainty in their values is within the 95 % confidence interval of the different measurements. The dielectric constant of the mixture (ϵ) has not been measured; the mean value of the dielectric constants of their components has been arbitrarily taken as a first order approximation of the real value. The viscosity is $\mu = 2.3 \pm 0.2$ mPa s, measured with a custom-made Ostwald viscometer. The density is $\rho = 1065$ Kg/m³, measured with a pycnometer.

Minimizing the liquid spreading over the tube tip is essential to the robustness and reproducibility of the experiments. To do that a superhydrophobic stainless steel surface was generated at the tube tip by following a methodology similar to that presented in Li et al. 2012. First of all, the surface of the tube tip was cleaned with distilled water, ethanol and acetone, then it was dipped in a mixture of 50 % in weight of hydrochloric acid and nitric acid for 3 minutes to produce the acid etching and passivation of the surface, and rinsed afterwards in distilled water. Once dried the process is followed by the deposition of a hydrophobic film; a thin layer of a commercial anti-wetting agent (602A-FP and 602A-FS, Cytonix) was deposited on the outer part of the tube's tip to ensure that the oscillating meniscus is anchored at the tube's outer rim. The coating process consisted of dipping the tube's tip in the commercial anti-wetting solution and on thermally stabilizing the agent for 60 minutes in air at 150°C. After this, the coating cures at room temperature for 24 hours before using the tube.



(a) Collage of different frames, with recognition of different meniscus and droplet shapes. The shapes which are recognized are marked with a white border.



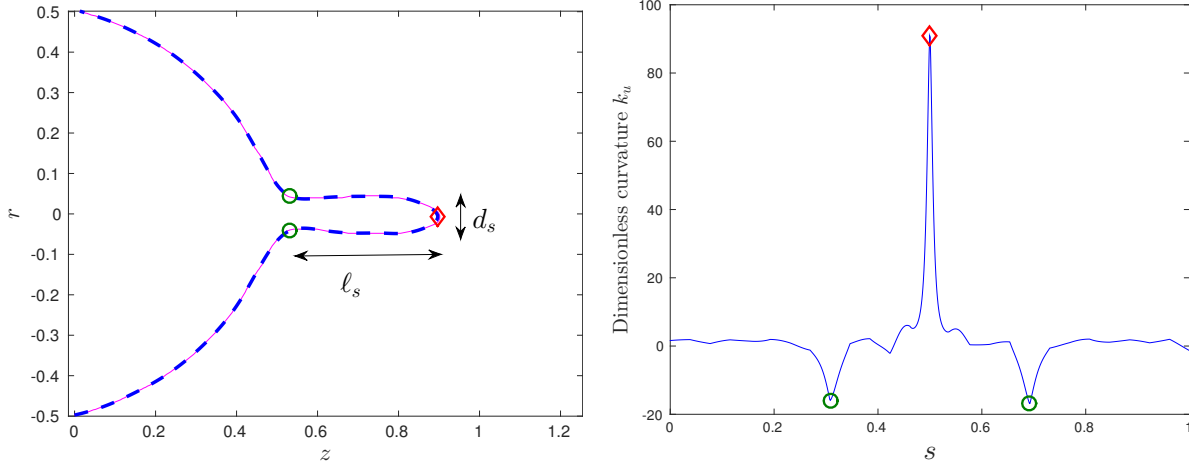
(b) Edge detection. The cross symbols correspond to the edge detection made by the Canny method after the subpixel correction. The white curve is the fitting of cubic splines to the position of the edges detected.

Figure 2.2: Interface tracking for periodic microdripping emission with $\hat{q} = 2.1$ mL/h, $\hat{\phi}_0 = 3.39$ kV, $L = 9$ mm and $D = 500$ μ m.

The volume of the detached droplets has been measured as follows. For a given microdripping situation, the oscillating meniscus and the emitted droplets have been continuously recorded using a high speed camera, so the time evolution of the meniscus and of an emitted droplet, as

it moves away from the meniscus, are obtained; see Fig. 2.2 for a few sample frames. Each frame of the emitted droplet, which is not spherical due to its own oscillations, has been processed with a custom-made software of interface tracking, see appendix B, which provides the droplet's contour in the visualization plane; say $\hat{r} = \hat{r}_d(\hat{z})$, where, ideally, \hat{z} and \hat{r} are distances along and normal to the axis of the tube. White curves in Fig. 2.2(a) show sample detected contours of the meniscus and the flying droplet. The volume of the droplet is calculated from its contour under the assumption of axisymmetry. A 95 % confidence interval is considered for the results, and hence the mean volume of the droplet, \hat{V}_{mean} , and its measurement uncertainty, $\delta\hat{V}_{mean}$, are calculated by processing a large number of frames. The measurement is accepted if the uncertainty is sufficiently small. The droplet equivalent diameter is then defined as $\hat{d}_d = (6\hat{V}_{mean}/\pi)^{1/3}$.

A similar approach has been used to measure the instantaneous meniscus volume. More precisely, the Canny algorithm (Canny 1986) has been used to detect the edges of droplets and meniscus in each frame. To increase precision, a sub-pixel detection method has also been implemented which consists of fitting a sigmoid function to the gray intensity level across the edge in each point, as in Acero et al. 2013 and Song et al. 1996. An example of how the algorithm works is shown in Fig. 2.2(b). The picture on the left shows a frame of the oscillating meniscus, where the ligament that eventually will form a droplet can be identified. The picture on the right shows a detail of the neck forming at its base. The cross symbols in this picture mark the edge defined by sequentially applying the sub-pixel and Canny algorithms. The white curve corresponds to the least square spline interpolation of the points defining the edge, using different cubic splines. Finally, the spline fitting is used to compute the instantaneous volume of the droplet and the meniscus. The relative variation of the meniscus volume during a cycle of the oscillation is always small when the flow rate is small, and increases when this parameter increases.



(a) *Meniscus profile in dimensionless coordinates $r = \hat{r}/D$, $z = \hat{z}/D$. The dashed line is the least square spline interpolation to the detected points of the meniscus from the images, using the subpixel algorithm. The circles and the diamond represent the position of the base and the tip of the ligament, respectively.*

(b) *Dimensionless meniscus curvature, $k_u = D\hat{k}_u$, as a function of arc length, s , calculated from splines fitted to the meniscus shape. The diamond represents the tip and the circles represent the base of the ligament.*

Figure 2.3: Detection of the ligament dimensions.

To measure the length $\ell_s = \hat{\ell}_s/D$ and the width $d_s = \hat{d}_s/D$ of the ligament at the tip of the meniscus (see Fig. 2.3), we have measured first the local mean curvature of the meniscus surface using the splines fitted to its contour; say $z(s)$ and $r(s)$, where s is the arc length on the meniscus contour. The curvature of the meniscus, assumed axisymmetric, in dimensionless form is

$$k_u(s) = \frac{z''(s)r'(s) - z'(s)r''(s)}{[z'(s)^2 + r'(s)^2]^{3/2}} - \frac{z'(s)}{r(s)[z'(s)^2 + r'(s)^2]^{1/2}}, \quad (2.1)$$

which is shown in Fig. 2.3(b) for a sample case. The base (circles) and tip (diamond) of the ligament are then readily located. The length ℓ_s of the ligament is defined as the axial distance between these points, while its width d_s is the maximum diameter of the ligament cross-section, when the arc length s varies between the values corresponding to the base and the tip. The curvature, \hat{z} , and \hat{r} have been non-dimensionalized with the tube's diameter D ; and the arc length \hat{s} , in such a way that $s = 0.5$ at the meniscus tip.

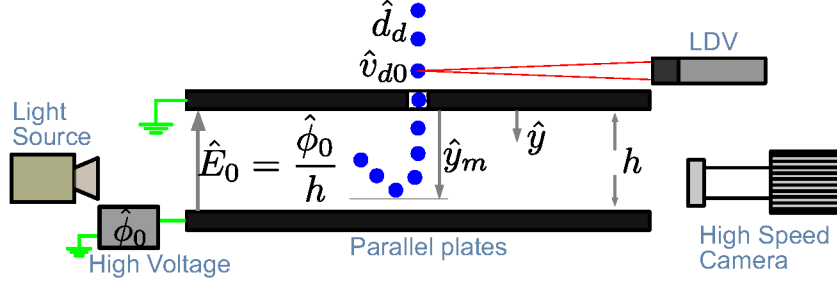


Figure 2.4: Setup used to measure the droplets electric charge.

The electric charge carried by the droplets has been measured using the device sketched in Fig. 2.4. The droplets emitted by the meniscus enter the space between two parallel metal plates separated a distance h through a small orifice drilled in the upper plate. This plate is grounded, as it is the collector electrode in Fig. 2.1. The lower plate is set to a voltage $\hat{\phi}_0$, which induces a uniform field $\hat{E}_0 = \hat{\phi}_0/h$ between the plates that pushes the droplets toward the upper plate. The velocity \hat{v}_{d0} with which the droplets enter the orifice is measured with a laser Doppler velocimeter, and the trajectory of a droplet between the plates is recorded with a high speed camera. The charge of the droplet \hat{C}_d is determined by comparing the recorded trajectory with the trajectory computed by solving the vertical equation of motion of the droplet,

$$m_d \hat{v}_d \frac{d\hat{v}_d}{d\hat{y}} = -\hat{C}_d \hat{E}_0 - \frac{\pi}{8} c_D \rho_a \hat{d}_d \hat{v}_d |\hat{v}_d|, \quad (2.2)$$

$$\text{with } \hat{v}_d = \hat{v}_{d0} \text{ at } \hat{y} = 0,$$

where m_d and \hat{v}_d are the mass and velocity of the droplet; ρ_a is the density of the air between the plates; and c_D is the drag coefficient, given by $c_D = (24/\text{Re})(1 + 0.15 \text{Re}^{0.687})$ in terms of the Reynolds number $\text{Re} = \rho_a |\hat{v}_d| \hat{d}_d / \mu_a$, with μ_a the viscosity of the air (Clift et al. 2005). The charge \hat{C}_d is determined from the condition that the lowest point of the droplet's trajectory computed from (2.2) coincide with that of the recorded trajectory. In many cases, the drag force turns out to be small compared to the electric force in equation 2.2, and then the lowest point of the trajectory is $\hat{y}_m \approx m_d \hat{v}_{d0}^2 / (2\hat{C}_d \hat{E}_0)$.

2.2.2 Oscillation regimes

The experiments were performed as follows. For a given setup geometry (needle size, needle-to-collector distance, collector geometry, etc.) a flow rate is selected and the voltage is sequentially increased. For zero voltage, the quasi-spherical meniscus grows until a single drop is detached by the effect of gravity. The diameter of this drop is larger than the diameter of the needle. As the voltage increases, the meniscus gets stretched along the needle axis, the detachment frequency increases and the size of the detached droplets decreases, although it is still of the order of the needle diameter. For a sufficiently large voltage, a periodic microdripping regime is suddenly attained, as the one shown in Fig. 2.5. This regime is identified by a jump in the meniscus oscillation frequency, by the appearance of a sharp conical tip on the stretched oscillating meniscus, and by a significant reduction of the diameter of the emitted droplets. The

motion is axisymmetric. The microdripping regime may be sustained within a certain voltage range. The same protocol is repeated for different flow rates. The voltage upper limit of this periodic microdripping is indicated by either the appearance of non-axisymmetric motions of the oscillating meniscus, when the flow rate is moderate, or by the emission of more than one droplet per oscillation, when it is larger.

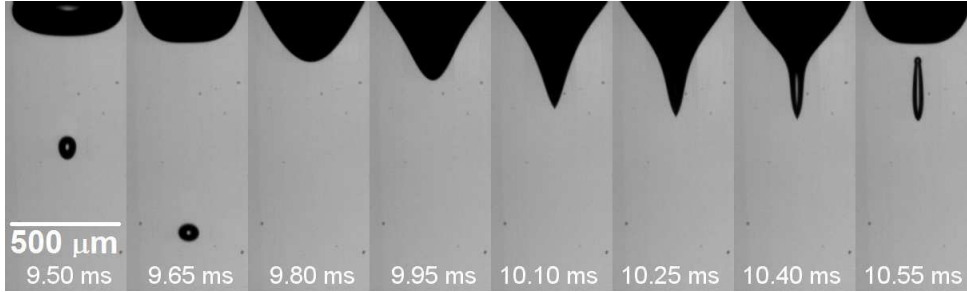
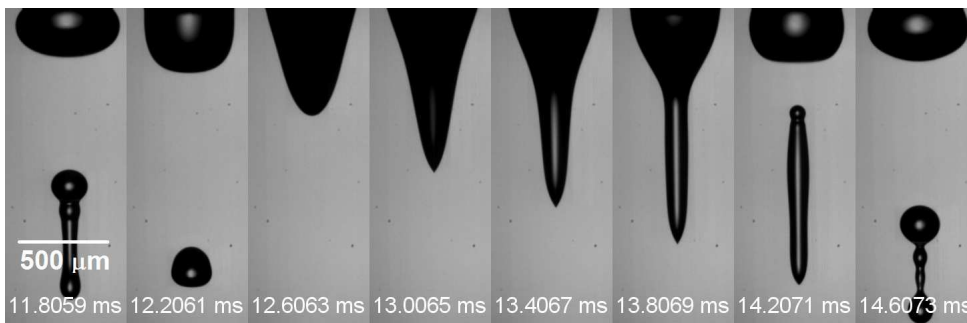
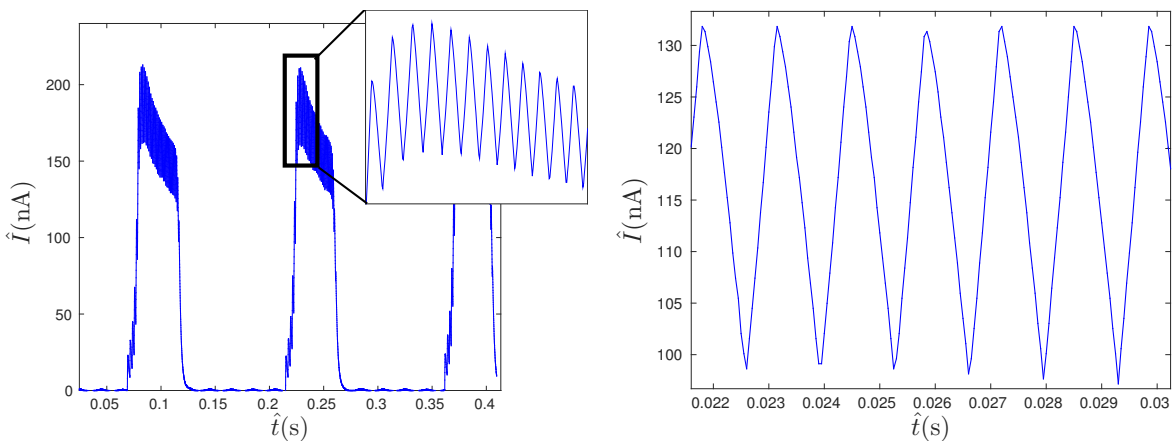
(a) $\dot{q} = 1.0 \text{ mL/h}$.(b) $\dot{q} = 10.0 \text{ mL/h}$.

Figure 2.5: Snapshots of the microdripping regime for $\hat{\phi}_0 = 3.39 \text{ kV}$, $L = 9 \text{ mm}$ and $D = 500 \mu\text{m}$.

Series of experiments have also been carried out in which the flow rate is increased at constant voltage, in order to characterize the range of flow rates compatible with the microdripping regime. For very low flow rates, not all the meniscus oscillations yield a droplet. As we shall see, the minimum flow rate for which periodic microdripping occurs also yields the minimum droplet diameter. The diameter of the emitted droplets increases with the flow rate until eventually the droplets cease to be small compared to the diameter of the capillary tube.



(a) *Non-periodic microdripping emission (axial spray mode I)* ($\dot{q} = 0.2 \text{ mL/h}$, $\phi_0 = 3.45 \text{ kV}$, $L = 9 \text{ mm}$, $D = 500 \mu\text{m}$).

(b) *Periodic microdripping emission (axial spray mode II)* ($\dot{q} = 0.5 \text{ mL/h}$, $\phi_0 = 2.95 \text{ kV}$, $L = 9 \text{ mm}$, $D = 500 \mu\text{m}$).

Figure 2.6: Current recorded at the collector electrode.

We have recorded the electric current induced at the collector electrode by the mass/charge emission from the oscillating meniscus, using a data acquisition card. The recorded current signal changes as the voltage applied to the needle increases, as shown in Fig. 2.6. Figure 2.6(a) shows a high frequency (KHz) charge emission that occurs intermittently at a much smaller frequency (tens of Hz), an electric non-periodic microdripping termed “axial spray mode I” by Juraschek et al. 1998. The oscillation of the meniscus becomes periodic for a larger voltage, giving an electric signal as the one shown in Fig. 2.6(b). This periodic microdripping is termed “axial spray mode II” by Juraschek et al. 1998. This behavior, in which the emission regime from the meniscus goes from electro-dripping to non-periodic microdripping (axial spray mode I) and then to periodic microdripping (axial spray mode II) as the voltage increases, only appears in our experiments when the liquid flow rate is small (the lowest value used in the experiments for each voltage). Otherwise, a direct transition from electro-dripping to periodic microdripping (axial spray mode II) occurs.

2.2.3 Dimensionless variables and results

The meniscus mean volume \hat{v}_M and oscillation frequency \hat{f} , and the electric charge \hat{C}_d and equivalent diameter \hat{d}_d of the detached droplets, have been measured for many values of the applied voltage and the flow rate. We shall use dimensional considerations and order-of-magnitude estimates to help organizing the large body of data thus gathered. In what follows, distances are scaled with the outer diameter of the needle, D , where the meniscus is attached, and times are scaled with the capillary time $t_c = (\rho D^3/\gamma)^{1/2}$. The dimensionless flow rate is

$$q = \frac{\hat{q}}{D^3/t_c} = \frac{\rho^{1/2}\hat{q}}{\gamma^{1/2}D^{3/2}}, \quad (2.3)$$

and the square of the voltage applied between needle and collector is measured by the Electric Bond number

$$B_E = \frac{\epsilon_0 E_c^2 D}{\gamma} \quad \text{with} \quad E_c = \frac{\hat{\phi}_0}{D \ln(4L/D)}. \quad (2.4)$$

Here ϵ_0 is the permittivity of vacuum, L is the needle-to-collector distance, and E_c is the characteristic electric field induced by the applied voltage around the end of the needle (Choi et al. 2008; Taylor 1969).

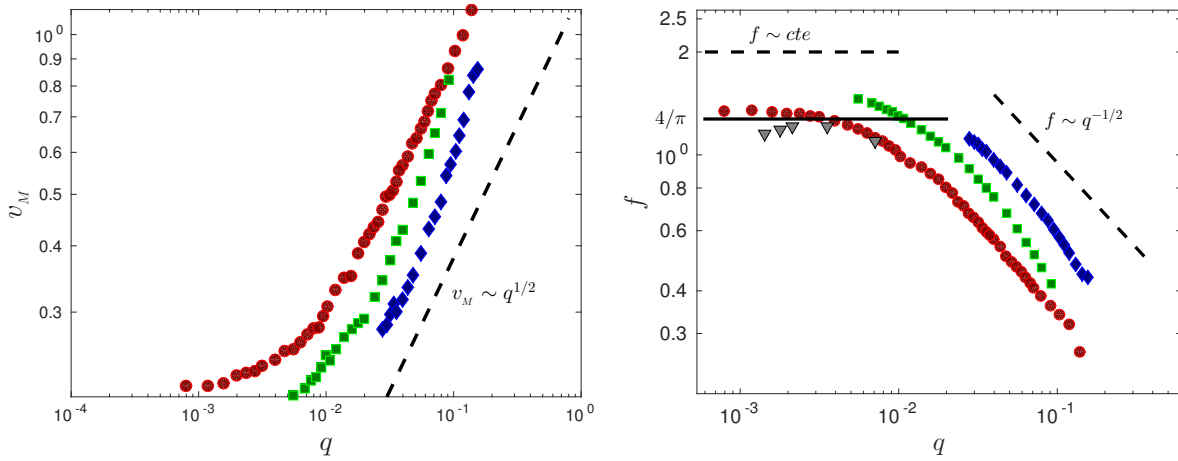
The needle-to-collector distance is large compared to the diameter of the needle; the ratio L/D is about 18 in the experiments. The length of the needle and the radius of the collector are even larger. In these conditions, the precise values of these two parameters are irrelevant, while L has only a weak effect that is accounted for using the expression of E_c in (2.4) above instead of the simpler expression $\hat{\phi}_0/D$.

The effect of the viscosity of the liquid, μ , is small in our experiments. Taking the capillary velocity $v_c = D/t_c$ as a characteristic liquid velocity, this effect is measured by the Ohnesorge number $Oh = \mu/(\rho v_c D) = \mu/(\rho \gamma D)^{1/2}$, which is small, of order 10^{-2} .

The effects of the electrical conductivity and the dielectric constant of the liquid, K and ϵ , are also small because the electric relaxation time $t_e = \epsilon_0 \epsilon / K$ is small compared to the capillary time, the ratio t_e/t_c being of order 10^{-7} . The electric relaxation time is the characteristic time required for the electric charge to reach the surface of the liquid by conduction and screen the liquid from the surrounding electric field; see, e.g. Fernández de la Mora et al. 1994. Its small value implies that the surface of the liquid is essentially at the potential of the needle in our experiments.

The effect of the gravity acceleration is also small because the Bond number $\rho g D^2/\gamma$ is small, of order 10^{-2} .





(a) Mean dimensionless volume of the meniscus, $v_M = \hat{v}_M/D^3$, as a function of the dimensionless flow rate for $B_E = 0.20$ (circles), 0.27 (squares) and 0.37 (diamonds). The dashed line has slope $1/2$.

(b) Dimensionless oscillation frequency, $f = \hat{f}t_c$, as a function of the dimensionless flow rate for $B_E = 0.20$ (circles), 0.27 (squares) and 0.37 (diamonds). The dashed line at the right-hand side has slope $-1/2$. Empty inverted triangles show data from Fig. 13 of Juraschek et al. 1998 for $B_E = 0.17$. The solid line stands for the expression $f = 4/\pi$ proposed by Marginean et al. 2006a.

Figure 2.7: Dimensionless mean volume and oscillation frequency respect to dimensionless flow rate.

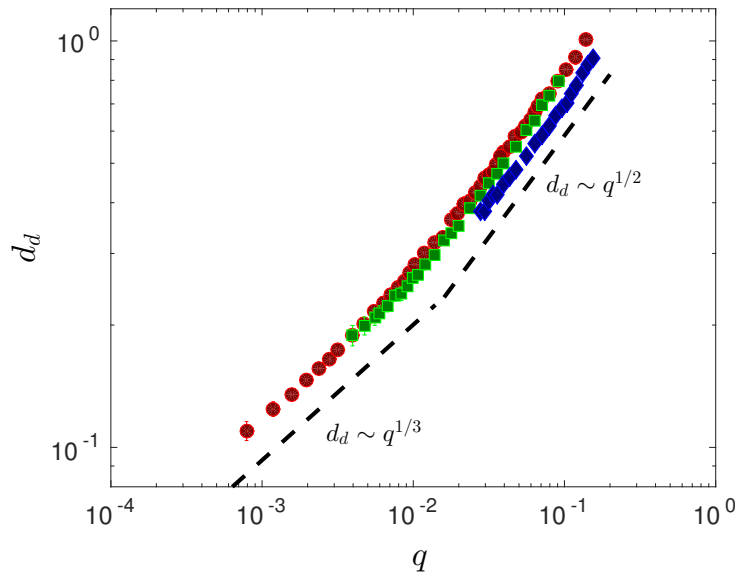


Figure 2.8: Dimensionless diameter of the droplet, $d_d = \hat{d}_d/D$, as a function of the dimensionless flow rate for $B_E = 0.20$ (circles), 0.27 (triangles) and 0.37 (squares). The dashed line at the left-hand side has slope $1/3$, and the dashed line at the right-hand side has slope $1/2$.

In these conditions, the only relevant control parameters are expected to be q and B_E . Figures 2.7(a), 2.7(b) and 2.8 show, respectively, the dimensionless volume of the meniscus averaged over a cycle of the oscillation, $v_M = \hat{v}_M/D^3$, the dimensionless frequency of the oscillation, $f = \hat{f}t_c$, and the dimensionless equivalent diameter of the droplets, $d_d = \hat{d}_d/D$, as functions of the dimensionless flow rate q for $B_E = 0.20$, 0.27 and 0.37 .

Figure 2.10 shows the electric charge of the droplet scaled with the charge given by the Rayleigh's limit at which a spherical droplet of diameter \hat{d}_d becomes unstable, \hat{C}_d/C_R with $C_R = (8\pi^2\epsilon_0\gamma\hat{d}_d^3)^{1/2}$ (see Rayleigh 1882) as a function of the Electric Bond number B_E for three

values of q . Figure 2.9 shows the square of the dimensionless frequency as a function of B_E for various values of q . All these results are for a needle of outer diameter $D = 500 \mu\text{m}$. Dimensionless data collected with capillary needles having different outer diameter also approximately collapse onto the same curves.

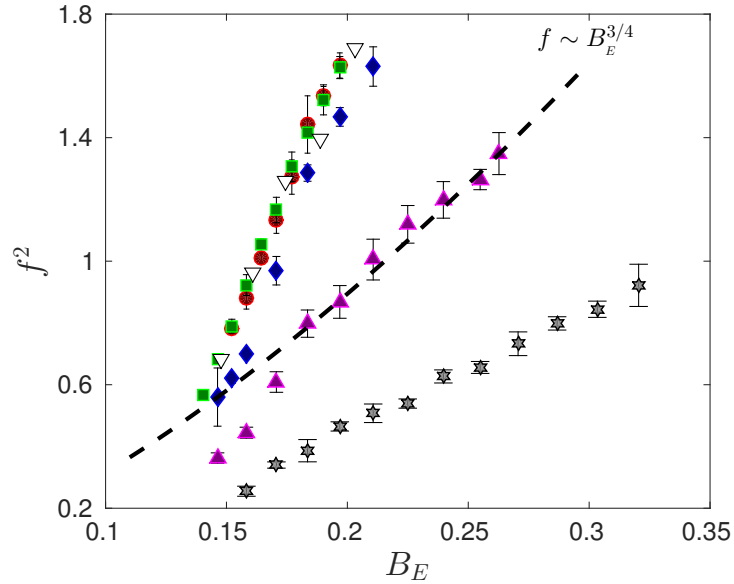


Figure 2.9: Square of the dimensionless oscillation frequency as a function of the Electric Bond number for $q = 8 \times 10^{-4}$, 2×10^{-3} , 4×10^{-3} , 1.47×10^{-2} and 3.4×10^{-2} , increasing from top to bottom (filled symbols). Empty inverted triangles show data from Fig. 6 of Juraschek et al. 1998 for $q = 1.42 \times 10^{-3}$. The dashed line stands for the expression $f \sim B_E^{3/4}$ proposed by Choi et al. 2008.

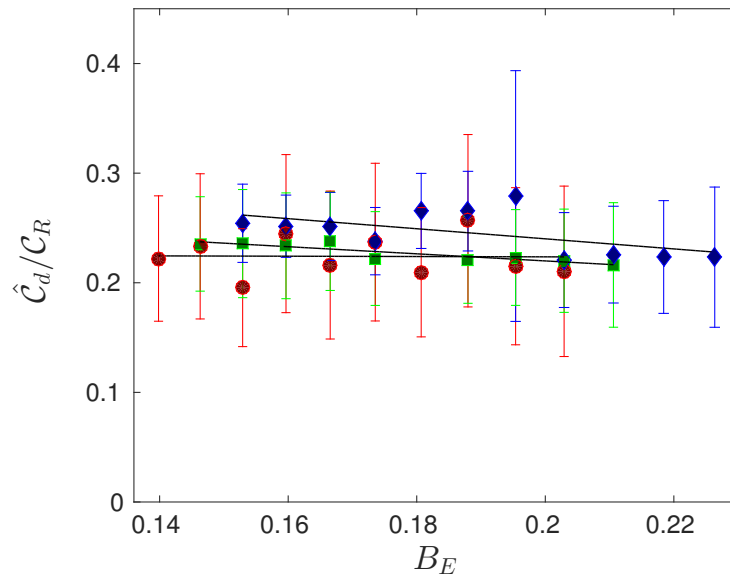


Figure 2.10: Dimensionless electric charge of the droplets, \hat{C}_d/C_R , as a function of B_E for $q = 1.6 \times 10^{-3}$ (circles), 4.1×10^{-3} (squares) and 1.2×10^{-2} (diamonds).

2.3 Results

2.3.1 Dimensionless frequency and mean volume

The microdripping regime analyzed here occurs only for values of the Electric Bond number of order unity, in a range that increases somewhat when the flow rate increases; see Fig. 2.9. Surface tension stresses, of $O(\gamma/D)$, and electric stresses, of $O(\epsilon_0 E_C^2)$, are thus of the same order and equally important in the evolution of the meniscus. The electric stress tends to elongate the meniscus axially, and the maximum elongation increases with the dimensionless flow rate. Inspection of sequences of images similar to those of Fig. 2.5 shows that (i) the diameter of the meniscus cross-section is not larger than the diameter of the needle D during most of the evolution, while its length, say H , may be of the order of D (at small flow rates) or somewhat larger than D (when the flow rate increases); and (ii) the amplitude of the oscillation of the tip is of the order of H . An order-of-magnitude balance of the liquid acceleration and the pressure force due to the electrically induced depression reads therefore $\rho H \dot{f}^2 \sim \epsilon_0 E_C^2 / H$, whence, in dimensionless variables, $f \sim B_E^{1/2} / v_M$.

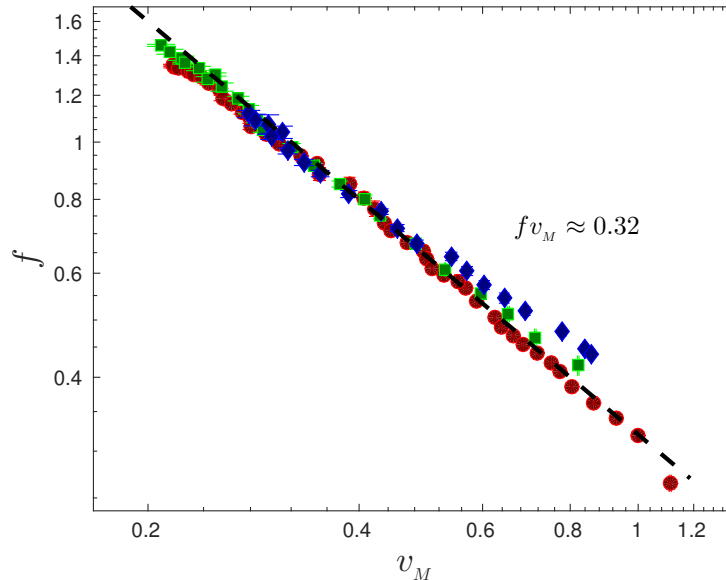


Figure 2.11: Dimensionless frequency, f , as a function of the mean dimensionless volume of the meniscus in each oscillation, v_M , for $B_E = 0.20$ (circles), 0.27 (triangles) and 0.37 (squares). The dashed line stands for the relation $f v_M \approx 0.32$.

In agreement with this estimation, the product $f v_M$ computed using data from Figs. 2.7(a) and 2.7(b) is nearly constant, independent of the flow rate in the whole range of this parameter spanned by our experiments. This product is also nearly independent of $B_E^{1/2}$, which may be due to the narrow range of $B_E^{1/2}$ where the microdripping regime is realized. With good approximation our results give $f v_M \approx 0.32$ (see Fig. 2.11).

2.3.2 Scale disparity. Small q and domain of existence

The volume of liquid emitted per period of the oscillation is equal to the volume supplied by the imposed flow rate during a period. At small flow rates, this volume is small compared to the volume of the meniscus. The ratio of droplet-to-meniscus volume is then of order q because the period of the oscillation is of the order of the capillary time ($f = O(1)$ at the left-hand side of Fig. 2.7(b)) and the volume of the meniscus is of the order of D^3 ($v_M = O(1)$ in

Fig. 2.7(a)). The periodic microdripping at small q entails thus a delicate balance to keep the mean meniscus volume close to the boundary between oscillations without volume loss and more violent oscillations in which electric stresses would tear the meniscus and cause the loss of a significant fraction of its volume.

This critical volume must coincide with the one indicated by the plateau value at the left in Fig. 2.7(a), a value that depends on the electrical Bond number. Similarly, the oscillation frequency of a meniscus with this critical volume must coincide with the plateau value in Fig. 2.7(b). This frequency is affected by the presence of the electric field and is different from the capillary frequency of a meniscus of the same volume. The electric field and the electric stress around the tip of the meniscus intensify when the meniscus elongates, which in turn reinforces the elongation until a conical tip develops. When the meniscus begins to recede, the conical tip lags behind the rest of the meniscus, and at the same time shortens and sharpens under the squeezing effect of the surface tension; see Fig. 2.5(a).

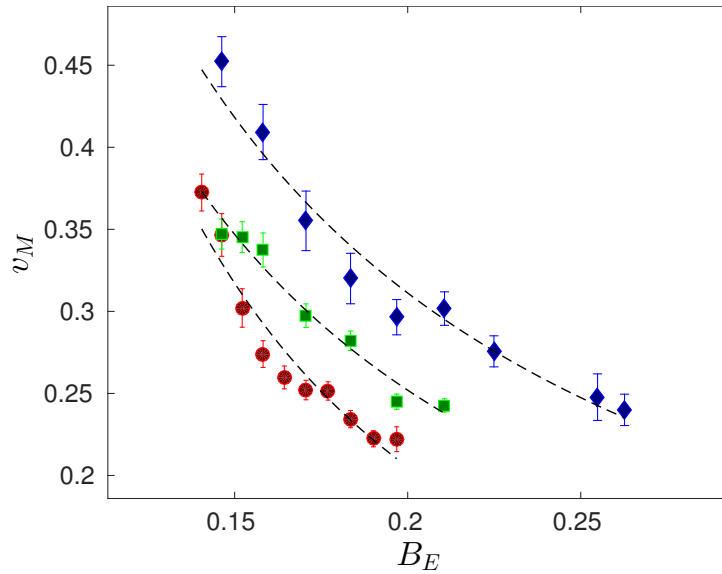


Figure 2.12: Contours of constant q in the (v_M, B_E) plane. Contours shown are for $q = 1.93 \times 10^{-3}$ (circles), $q = 3.86 \times 10^{-3}$ (squares) and $q = 1.43 \times 10^{-2}$ (diamonds), increasing from bottom to top.

Since the volume of the meniscus is nearly constant when q is small, the problem of finding v_M , f and d_d as functions of q and B_E can be approximately recast as that of finding $f(v_M, B_E)$ and $d_d(v_M, B_E)$ for a meniscus of strictly constant dimensionless volume v_M , and then making $q = (\pi/6)d_d^3 f$. Since $(v_M, B_E) = O(1)$, this problem should have a solution with $d_d \ll 1$ only in a narrow band around the curve of the (v_M, B_E) plane where $d_d = 0$. On one side of this curve the meniscus would oscillate without ejecting any droplet. On the other side of the curve the volume of the droplets, hence q , would increase with distance to the curve. To get an idea of the shape of the band and the limiting curve where $d_d = 0$, Fig. 2.12 shows some contours of constant, small q in the (v_M, B_E) plane. The lowest contour should be close to the limiting curve. As can be seen, the range of B_E where microdripping occurs extends to larger values of this parameter when q increases.

2.3.3 Comments on the tip emission of electrospay

One of the characteristics of the microdripping regime studied here is the existence of a sharp conical tip that persists during a non-negligible part of the meniscus oscillation cycle, as shown in Fig. 2.5. This conical tip leads to the formation of an electrospay. Even though we have not

attempted to measure or quantify such emission, its existence is confirmed by adding colorant to some of the liquids: a fine deposition, covering a wide area, was collected onto the counter electrode. There was impossible to completely eliminate this electro spray emission. However, its contribution to the total mass emitted per oscillation was negligible. The reason supporting that claim is twofold. First, for an electro spray of a very conductive liquid in the cone-jet mode, the characteristic flow rate is given by (Fernández de la Mora et al. 1994) $Q_e \sim (\gamma\epsilon_0\epsilon)/(\rho K)$, so one would expect that the flow rate carried by the electro spray was of that order. Comparing the former with the total flow rate, one obtains

$$\frac{Q_e}{\hat{q}} \sim \frac{\gamma\epsilon_0\epsilon}{\rho K \hat{q}} = \frac{t_e/t_c}{q} \ll 1. \quad (2.5)$$

Some preliminary experiments varying the liquid conductivity seem to support Eq. (2.5) in the sense that the ratio Q_e/\hat{q} decreases as K increases, although an investigation of its precise dependence on the conductivity is beyond the scope of the present work. In principle Eq. (2.5) also provides a minimum flow rate criterion; namely that $\hat{q} > Q_e$, since no main droplet will be emitted if the entire flow rate is emitted as electro spray. However, experiments performed with very small flow rates show that the periodic microdripping regime gives way to a pulsed non-periodic emission akin to axial spray mode I of Juraschek et al. 1998 well before values of the order of Q_e are reached.

Second, in all the experiments we compared the value of the diameter of the emitted droplet measured from the images with the one obtained from the mass conservation balance (including the measured oscillation frequency). The differences between them were within the measurement errors. In conclusion, the mass emitted in the form of an ultrafine electro spray is negligible, so we shall consider that the total mass is emitted in the form of a single drop.

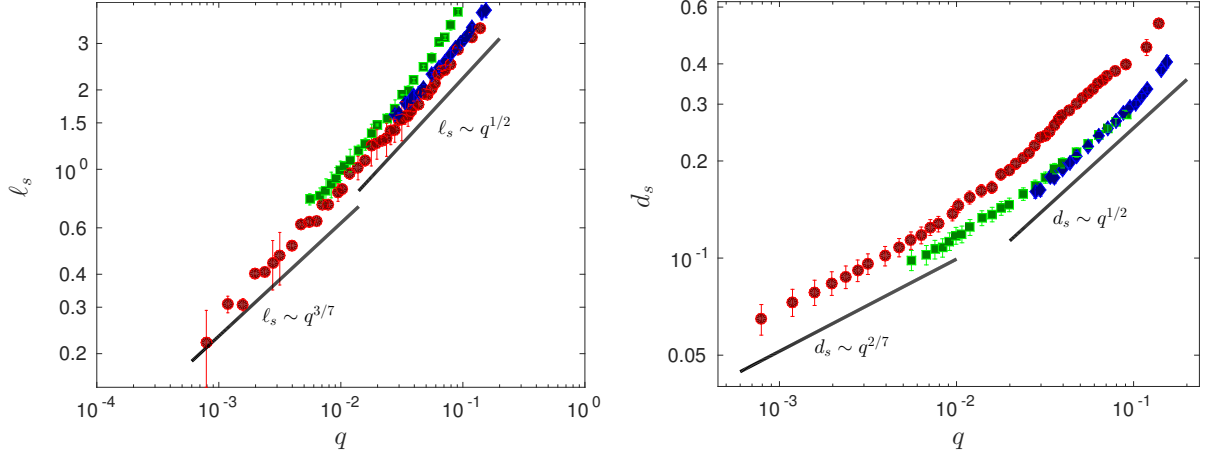
From the practical point of view, even though electro spray emission might be an undesirable effect of this microdripping regime, the fact that these ultrafine droplets are highly charged (high electrical mobility) allows sweeping them out very easily by using nearby electrodes, while the main droplet may fly away carried by its own inertia.

2.3.4 Ligament characterization

Figure 2.13 shows the dimensionless length and width of the ligament at the tip of the meniscus immediately before a droplet is ejected ($\ell_s = \hat{\ell}_s/D$ and $d_s = \hat{d}_s/D$) as functions of the dimensionless flow rate for three values of B_E . These results suggest that ℓ_s and d_s increase as powers of q , although these powers may be different for the very small values of q corresponding to the plateaus of Figs. 2.7(a) and 2.7(b) and for larger values of this parameter.

The conditions around the tip of the meniscus when the ligament develops are too complex to allow a simple analysis of the process, which seems to depend on the competition of electric stresses trying to elongate the ligament and the retraction of the rest of the tip, that probably pushes the liquid toward the bulk of the meniscus. At least for very small values of q , the process appears to be local, in the sense that it does not affect the evolution of the rest of the meniscus, and short compared to the period of the oscillation. Tentative estimates for the latest stages of the ligament evolution are worked out in this section.

The results for the smallest values of q in Figs. 2.13 can be partially rationalized as follows. As mentioned in Section 2.3.2, inspection of a number of video records suggests that a ligament appears in these cases because, after reaching its maximum elongation, most of the meniscus begins receding under the effect of surface tension stresses while locally intense electric stresses still keep its tip pinned. Assuming that recession occurs at the capillary velocity v_c (from the balance of inertia and surface tension in the bulk of the meniscus), and that the time available for the ligament to form is of the order of the pinchoff time $t_s = (\rho \hat{d}_s^3/\gamma)^{1/2}$ determined from the balance of inertia and surface tension in the ligament ($\rho \hat{d}_s^2/t_s^2 \sim \gamma/\hat{d}_s$), the length of the ligament would be $\hat{\ell}_s \sim v_c t_s = \hat{d}_s^{3/2}/D^{1/2}$. In addition, the volume of the detaching ligament must coincide



(a) Dimensionless length of the ligament $l_s = \hat{l}_s/D$ respect to the dimensionless flow rate q . The dashed straight lines at the left-hand sides have slopes $3/7$. The dashed lines at the right-hand side have slope $1/2$.

(b) Dimensionless width of the ligament $d_s = \hat{d}_s/D$ respect to the dimensionless flow rate q . The dashed straight lines at the left-hand sides have slopes $2/7$. The dashed lines at the right-hand side have slope $1/2$.

Figure 2.13: Dimensionless length and width of the ligament immediately before detachment as functions of the dimensionless flow rate for $B_E = 0.20$ (circles), 0.27 (squares) and 0.37 (diamonds).

with the volume of liquid supplied to the meniscus during a period of the oscillation, which is of the order of the capillary time; i.e., $\hat{d}_s^2 \hat{l}_s \sim \hat{q} t_c$. These two conditions taken together give $l_s \sim q^{3/7}$ and $d_s \sim q^{2/7}$, which are represented by the dashed lines at the left-hand side of Figs. 2.13. However, the consistency of these estimations is not immediately clear. At first sight, since the only dimensionless control parameters of the problem are q and B_E , the proportionality factors implicit in the proposed power laws can be at most functions of B_E and should be expected to be of order unity because $B_E = O(1)$. This would imply that $l_s \ll d_s$ for any $q \ll 1$, which is meaningless. The measured aspect ratio of the detaching ligament is $l_s/d_s = 4-8$ in our experiments, indicating that the proportionality factor for \hat{d}_s/D is small compared with that for \hat{l}_s/D in the small region of the parameter space where this type of microdripping occurs.

The evolution of the meniscus undergoes some changes when the flow rate q increases. First, the period of the oscillation increases with q past the plateau at the left of Fig. 2.7(b). Redoing the estimations above with a period proportional to $q^{1/2}$, the modified results $l_s \sim q^{9/14}$ and $d_s \sim q^{3/7}$ are obtained, whose larger exponents are in qualitative agreement with the increasing slopes at the right-hand side of Figs. 2.13. Second, the elongation of the meniscus increases with q , which modifies the process of formation of a ligament. The process changes from the axial growth due to differential receding velocities discussed above to a radial squeezing of a region of the elongated meniscus around its tip; compare Figs. 2.5(a) and 2.5(b). The length of this region eventually becomes of the order of the total length of the meniscus, though the volume emitted per cycle is still small compared to the volume of the meniscus because the ligament undergoes substantial radial squeezing before detachment. The elongation time of the meniscus is $T \sim \hat{l}_s/v_E \sim \rho^{1/2} \hat{l}_s/\epsilon_0^{1/2} E$ in these conditions, where the velocity induced in the liquid by electric stresses (from the balance $\rho v_E^2 \sim \epsilon_0 E^2$) has been used. This estimation is equivalent to that of section 2.3.1 with \hat{l}_s playing the role of the length of the meniscus. Assuming that the period of the oscillation is of the order of the elongation time, the volume conservation condition $\hat{d}_s^2 \hat{l}_s \sim \hat{q} T$ gives $d_s \sim q^{1/2}/B_E^{1/4}$, while the value of l_s is not determined by these estimations. The square root increase of the width of the ligament with dimensionless flow rate agrees with the results of Fig. 2.13(b) (dashed line at the right-hand side of this figure).

Figure 2.13(a) shows that the length of the ligament also increases nearly as the square root of q . This result can be understood noticing that: (i) Electric stresses are needed to partially offset surface tension stresses in the prominent, elongated ligament that develops for large values

of q ; see, e.g., Fig. 2.5(b). This requires $\epsilon_0 \hat{E}_n^2 \sim \gamma / \hat{d}_s$, where \hat{E}_n is the electric field at the surface of the ligament. And (ii) the measured electric charge of the detached droplets is of the order of the limit Rayleigh's charge $\mathcal{C}_R = (8\pi^2 \epsilon_0 \gamma \hat{d}_d^3)^{1/2}$. The ratio of the measured charge to the limit charge is about 1/4 and depends little on q and B_E ; see Fig. 2.10. The conditions that the charge and volume of a droplet should coincide with the charge and volume of the ligament immediately before detachment read $\sigma \hat{d}_s \hat{\ell}_s \sim \mathcal{C}_R$ and $\hat{d}_s^2 \hat{\ell}_s \sim \hat{d}_d^3$, where $\sigma = \epsilon_0 \hat{E}_n$ is the surface density of charge in the ligament (Landau et al. 1984). Upon eliminating \hat{d}_d and \hat{E}_n , these conditions give $\ell_s \sim d_s$ up to a numerical factor that turns out to be in the order of 6–7.

2.3.5 High q trends and droplet diameter

The estimation $\ell_s \sim q^{1/2} / B_E^{1/4}$ (up to a numerical factor) accounts for the increase of the dimensionless volume of the meniscus at the right-hand side of Fig. 2.7(a). Also, together with the estimation of the elongation time worked out in Section 2.3.4, which can be recast as $f \sim B_E^{1/2} / (\ell_s)$ in dimensionless variables, it accounts for the decrease of the dimensionless frequency at the right-hand side of Fig. 2.7(b).

The dimensionless equivalent droplet diameter in Fig. 2.8 increases as $q^{1/3}$ for very small flow rates and as $q^{1/2}$ for larger flow rates. Both results follow from the volume conservation condition $d_d = (6/\pi)^{1/3} (q/f)^{1/3}$ noticing that $f = O(1)$ for small q and $f = O(q^{-1/2})$ for larger q . It is noteworthy that the type of microdripping analyzed here can be operated to yield monodisperse droplets whose diameter is one tenth of the diameter of the capillary tube to which the oscillating meniscus is attached.

2.3.6 Comparisons with other results in the literature

For comparison, some experimental data of Juraschek et al. 1998 for the meniscus pulsation frequency as a function of q and B_E have been included in Figs. 2.7(b) and 2.9 (empty inverted triangles). Since these results have been used for reference in much of the later work (see, e.g., Chen et al. 2006; Choi et al. 2008), the good agreement displayed by this comparison shows that our results fit into the body of known data. Some of the pictures of Juraschek et al. 1998 suggest that the contact line of their menisci with the capillary tube may in some cases spread slightly along the outer surface of the tube. While the liquid wetting this surface is not expected to play an important part in the oscillation of the meniscus, because its motion is hindered by the proximity of the wall, it still enlarges the radius of the liquid surface and thus decreases the electric field acting on it. To try to account for this effect, an arbitrary reduction factor has been included in the expression of the electric field E_c in (2.4), whose value has been chosen for the plateaus in Fig. 13 of Juraschek and Röllgen and in our Fig. 2.7(b) to coincide. The good agreement achieved when this same factor is used for the data in Fig. 2.9 partially justifies its use.

A number of scaling laws for the meniscus oscillation frequency in pulsating spray modes have been proposed by different authors. Marginean et al. 2006a note that the oscillation frequency of low conductivity liquids in large emitters is remarkably close to the lowest capillary frequency of an isolated spherical droplet of radius equal to the radius of the contact line, which is given by $f = 4/\pi$ in our dimensionless variables and is marked by the solid line in Fig. 2.7(b). Following Juraschek et al. 1998, these authors attribute the increase of the oscillation frequency with the voltage applied to the meniscus to a decrease of the amount of liquid pulsating at the end of the capillary. Similarly, they explain the decline of the frequency with increasing flow rate as an effect of the increase of liquid volume. Using Marginean et al. 2006a estimate as a starting point, Choi et al. 2008 work out the modified scaling $f \sim B_E^{3/4}$ by replacing the radius of the contact line by the radius of the ejected ligament, which they estimate independently.

Their result is included in Fig. 2.9 (dashed line). It qualitatively accounts for the trend of the data, although it does not include the effect of the flow rate on the frequency.

Some numerical results for axial spray mode II have been reported in Higuera et al. 2013a for an inviscid liquid of infinite electrical conductivity that is injected at a constant flow rate through an orifice in a metallic plate into a region of uniform electric field. The numerical results reproduce the main features of the periodic dynamics, including the stretching of the meniscus, the formation of a ligament whose tip emits a spray of tiny droplets and eventually detaches, and the subsequent recoil of the meniscus. However, the simplified configuration used in the numerical simulations precludes quantitative comparison with our experimental data. Thus, for a value of the dimensionless flow rate in the range of our experiments, the numerical values of the Electric Bond number required for periodic microdripping (based on the uniform electric field far from the meniscus) are somewhat larger than the experimental values. The computed oscillation frequency and the maximum length of the ligament are somewhat larger than in the experiments and the mean volume of the meniscus is significantly smaller. These differences can be traced to the morphology of the electric field. Contrary to the case of a meniscus at the end of a capillary, the electric field does not tend to zero far from a meniscus on a metallic plate. This leads to enhanced electric stresses that accelerate the formation of a ligament, increase its elongation, and cause its detachment before the volume of the meniscus can increase much. In addition, since the flow rate is given, the faster dynamics also implies a larger dripping frequency.

2.4 Conclusions

We have studied the electric microdripping regime of highly conducting, low viscosity liquids, as a mean to generate monodisperse droplets with diameter considerably smaller than the capillary tube holding the dripping meniscus. We have focused on the conditions in which the microdripping is periodic.

During each oscillation, the meniscus elongates axially, growing an axisymmetric disturbance that eventually leads to the formation of a ligament and a droplet. Simultaneously, the meniscus develops a pointed tip which emits an ultrafine aerosol for a non-negligible fraction of the cycle. However, in the conditions investigated, almost all the mass emitted per oscillation is contained in the main droplet. The ultrafine emission seems to evolve on its own, independently of the main breakup process.

The dimensionless parameters controlling this periodic microdripping regime are the Electric Bond number, B_E , and the dimensionless liquid flow rate, q . The microdripping regime occurs in a fairly narrow range of values of B_E of order unity. The mean volume of the meniscus in an oscillation cycle is of the order of the cube of the diameter of the capillary tube for very small values of the flow rate, and increases nearly as the square root of the flow rate when this parameter increases. The oscillation frequency nondimensionalized with the capillary time is of order unity for very small q and decreases as $1/q^{1/2}$ when q increases.

Approximate scaling laws valid in different ranges of q have been worked out for the length and width of the ligament, and for the diameter of the main droplets.

By reducing the liquid flow rate, this mode of periodic microdripping can easily yield monodisperse droplets with diameters one tenth of that of the capillary tube at rates of the order of the capillary frequency. In the data shown, monodisperse droplets of $50 \mu\text{m}$ from a nozzle of $500 \mu\text{m}$ are produced at rates of several kHz, thus demonstrating that this microdripping regime constitutes a real alternative to the hydrodynamic atomization techniques currently used for printing or for material processing. The scaling laws obtained should allow designing the geometry of the nozzle device together with the properties of the liquid to set a given droplet size range, potentially including sub-micronic, within which monodisperse droplets may be produced at will.

References

- Acero, A. et al. 2013. Experimental analysis of the evolution of an electrified drop following high voltage switching. *Eur. J. Mech. B* 38, 58–64.
- Canny, J. 1986. A computational approach to edge detection. *IEEE Trans. Pattern Anal. Machine Intell.* (6), 679–698.
- Chen, C. H., Seville, D. a., & Aksay, I. a. 2006. Scaling laws for pulsed electrohydrodynamic drop formation. *Appl. Phys. Lett.* 89(12), 2005–2007.
- Choi, H. K. et al. 2008. Scaling laws for jet pulsations associated with high-resolution electrohydrodynamic printing. *Appl. Phys. Lett.* 92(12), 2006–2009.
- Clift, R., Grace, J. R., & Weber, M. E. 2005. *Bubbles, drops, and particles*. Courier Corporation.
- Fernández de la Mora, J. & Loscertales, I. G. 1994. Current emitted by highly conducting Taylor cones. *J. Fluid Mech.* 260, 155–184.
- Higuera, F. J. et al. 2013a. Pulsating emission of droplets from an electrified meniscus. *J. Aerosol Sci.* 66, 193–208.
- Juraschek, R. & Röllgen, F. 1998. Pulsation phenomena during electrospray ionization. *Int. J. Mass Spectrom.* 177, 1–15.
- Landau, L. D. et al. 1984. *Electrodynamics of continuous media*. Vol. 8. elsevier.
- Li, L., Breedveld, V., & Hess, D. W. 2012. Creation of superhydrophobic stainless steel surfaces by acid treatments and hydrophobic film deposition. *ACS Appl. Mater. Interfaces* 4(9), 4549–4556.
- Marginean, I. et al. 2006a. How much charge is there on a pulsating Taylor cone? *Appl. Phys. Lett.* 89(6), 064104.
- Rayleigh, L. 1882. XX. On the equilibrium of liquid conducting masses charged with electricity. *Philos. Mag.* 14(87), 184–186.
- Song, B & Springer, J. 1996. Determination of Interfacial Tension from the Profile of a Pendant Drop Using Computer-Aided Image Processing2. Experimental. *J. Colloid Interface Sci.* 184, 77–91.
- Taylor, G. 1969. Electrically Driven Jets. *Proc. R. Soc. London A* 313(1515), 453–475.

Chapter 3

Perfect conductor liquid model simulations

Contents

3.1	Introduction	29
3.2	Mathematical model	31
3.2.1	Equations	31
3.2.2	Non-dimensionalization	32
3.2.3	Perfect conductor assumption	32
3.2.4	Inviscid liquid assumption	33
3.3	Numerical procedure	33
3.3.1	Global mass conservation, pinch-off condition and tip treatment	34
3.3.2	Electrical and capillary stresses on the meniscus surface	36
3.4	Comparison with experiments	38
3.5	Conclusions and future works	43
	References	45

3.1 Introduction

The dynamics of a meniscus of a conducting liquid hanging at the tip of a capillary tube, when subjected to an electric field, present a broad variety of functioning modes. For intense enough electric fields, those modes eventually lead to the atomization of the liquid, thus constituting the so-called electro-hydrodynamic (EHD) atomization technique. Cloupeau et al. 1994, and Krupa et al. 1999 classified for the first time those modes. Juraschek et al. 1998 investigated the EHD atomization when a capillary tube continuously fed with liquid was placed in front of a metallic plate, such that the electric field was set by applying a constant voltage difference between the needle and the plate (i.e. needle-plate configuration). For low voltage differences, droplets detach continuously from the capillary tip due to the electric pulling: this is called electrodrizzling. These droplets have diameters similar to that of the capillary tube. As the voltage difference increases, they found three axial atomization modes in which the droplets are substantially smaller than the capillary tube, which they labeled as axial mode I, II and III. The first two modes are pulsating modes, where the meniscus is oscillating axially. In the axial mode I, sequences of emissions, in which ligaments are stretched from the meniscus tip and finally detached, are interspersed with intervals of no emission, where the meniscus oscillates at the frequency of an electrified pinned droplet without forming a ligament. Axial mode II is a periodic pulsating mode, also known as the microdrizzling emission mode, which is the one considered in this work. In each pulsation, a ligament is stretched and detached from the meniscus. This ligament may yield one or several droplets. Marginean et al. 2006b suggested that the axial mode I is a transition mode from electrodrizzling to microdrizzling regimes. Finally, axial mode III is a steady mode,



also known as steady cone-jet electrospray, where a fine jet is issued from the tip of a static meniscus.

We focus in the axial mode II in situations in which a single droplet is produced in each oscillation, since this is a simple way to produce monodisperse droplets, considerably smaller than the capillary tube, at relatively high frequencies. In Chapter 2 we studied experimentally the axial mode II for the production of monodisperse droplets. We found that the main controlling parameters are the liquid flow rate, q in dimensionless form, and the voltage difference, B_E in dimensionless form. While $B_E = O(1)$, q may span several orders of magnitude, thus becoming the most important controlling parameter. We also proposed some asymptotic power-law for the dependence of the dimensionless oscillation frequency f , the dimensionless droplet diameter d_d and the ligament length and diameter, ℓ_s and d_s respectively, versus q . Briefly, we noticed two different trends, one for the moderate and large values of q and other for the smaller values of q . For low values of q , the dynamic of the meniscus is independent of that of the tiny ligament, so that f becomes independent of q , being of the order of the capillary frequency; the droplet diameter d_d decreases with q , so they could form droplets ten time smaller than the capillary tube. For larger values of q the ligament length becomes comparable to the meniscus size, and it exist for a rather important part of the oscillation period, so it strongly affects the dynamics of the whole process. We also noticed the emission of an ultrafine spray from the tip of the ligament during part of its elongation stage, particularly while its tip locally adopts a conical shape. This happens during a non-negligible part of the microdripping period, resembling a cone-jet electrospray emission. In Chapter 2 we argued that the flow rate emitted from the tip in the form of an ultrafine aerosol has a negligible contribution to the total volume emitted in each meniscus oscillation because of the high conductivity of the dissolution used. Nevertheless, the presence of such ultrafine highly charged aerosol is expected to affect the electric field, at least in a region close to the ligament tip.

In this chapter we model and simulate the dynamic of a meniscus of an inviscid liquid, $\mu = 0$, infinitely conducting, $K \rightarrow \infty$, (i.e. the liquid remains equipotential) subjected to an intense electric field in the needle-plate configuration and compare the results with experiments done with highly conducting water dissolutions in microdripping (axial mode II). This is similar to the work developed by Higuera et al. 2013b, except that now the electrode configuration is that of the real experiments, so the results may be contrasted. The model, which does not consider the droplets airborne, presents a limited range of applicability for two reasons. First, it does not apply at the cone-jet that may form locally at the tip of the ligament because the electric field enters the liquid in the cone-to-jet transition region (Higuera 2003), so the liquid does not remain equipotential there. Second, the ultrafine, highly charged aerosol emitted from the tip strongly distorts the electric field around the tip of the ligament in a region whose extend is unknown. A more appropriate treatment of the liquid tip would require the balance of charges on the surface of the liquid forming the meniscus (Higuera 2003), which requires solving the electric field inside the liquid. Unfortunately, the time scale of the dynamics of the charges are of the order of the electric relaxation time, $t_e = \epsilon\epsilon_0/K$, where ϵ and K are the liquid dielectric constant and conductivity, respectively, and ϵ_0 is the permittivity of vacuum. For the high conductivity liquids used here, $t_e \sim 1 \times 10^{-9}$ s, so very short time steps are required to describe the fast dynamics of this tip, if possible at all. However, the size of the region around the tip where the liquid might not be equipotential is of the order of the distance in which the residence time of the liquid is of the order of the electric relaxation time (Fernández de la Mora et al. 1994), $\hat{r} \sim (\gamma/\rho)^{1/3} (\epsilon\epsilon_0/K)^{2/3}$, which in our experiments result $\hat{r} \sim 1 \times 10^{-7}$ m, that is, much smaller than any other length of interest. On the other hand, the meniscus oscillation time is of the order of the capillary time, $t_c = (\rho D^3/\gamma)^{1/2}$, where ρ and γ are the liquid density and surface tension, and D is the diameter of the capillary tube; in our experiments $t_c \sim 1 \times 10^{-3}$ s. Therefore, to avoid extremely long simulations, requiring very short time steps and very small size resolution, the perfect conductor liquid assumption is considered to be valid in the whole meniscus, although it cannot catch the details of what happens at the tip. Therefore, the model

is expected to capture the dynamic of the meniscus in situations in which the ligament conical tip forms relatively far from the meniscus, that is, for moderate or large flow rates.

3.2 Mathematical model

A flow rate \hat{q} of a liquid of density ρ , surface tension γ , zero viscosity ($\mu = 0$), and an infinite electrical conductivity $K \rightarrow \infty$, flows through an infinitely thin tube of length L_N and diameter D into the space between the tube and a flat counter-electrode of infinite radius, following the axisymmetric model sketched in Figure 3.1(a). The distance L between the tube's tip and the counter-electrode is much larger than the diameter of the tube, $D/L \ll 1$. An electric field, $\hat{\mathbf{E}}$, is created between the tube and the counter-electrode when a voltage difference ϕ_0 is applied between the tube and counter-electrode.

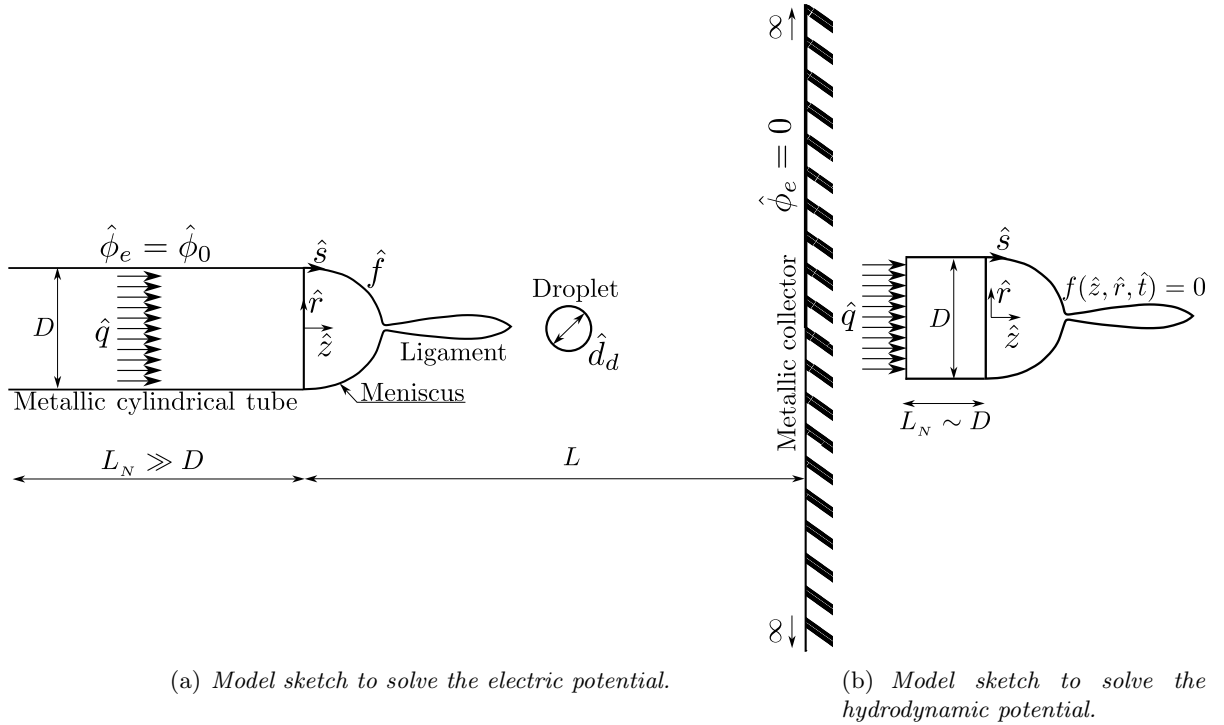


Figure 3.1: Definition Sketch.

3.2.1 Equations

The surface of the liquid is considered electrically equipotential and the movement of the meniscus perturbs the electric field in the vicinity of the tube's tip. The electric potential outside the liquid, $\hat{\phi}_e$, must satisfy the Laplace's equation, $\nabla^2 \hat{\phi}_e = 0$, which is solved outside the liquid in the region sketched in figure 3.1(a), with $\hat{\phi}_e = 0$ on the counter-electrode and infinitely far from the tube and the liquid, and $\hat{\phi}_e = \phi_0$ on the tube and the liquid as boundary conditions.

The flow is considered irrotational, and the velocity potential, $\hat{\mathbf{v}} = \nabla \hat{\phi}$, is calculated by solving the Laplace's equation in the liquid region, as sketched in Figure 3.1(b), which includes a length of the injection tube of the order of the tube diameter, $L_N \sim D$. We use homogeneous Neumann conditions at the walls of the tube, and $\nabla \hat{\phi} \cdot \mathbf{e}_z = 4\hat{q}/(\pi D^2)$ in the injection zone ($\hat{z} = -L_N$, $\hat{r} < D/2$), where \hat{q} is the liquid flow rate and \mathbf{e}_z is the unit vector in \hat{z} direction. On the surface of the liquid, defined by the function $f(\hat{z}, \hat{r}, \hat{t}) = 0$, with $f < 0$ inside the liquid, the kinematic condition, $Df/D\hat{t} = 0$, and the dynamic condition, $\partial_{\hat{t}} \hat{\phi} + \hat{p}/\rho + 1/2 \nabla \hat{\phi} \cdot \nabla \hat{\phi} - g\hat{z} = c(t)$, must be satisfied, where \hat{p} is the pressure in the liquid relative to the outer medium, g acceleration

of the gravity, $c(t)$ a constant that depends on the time, \hat{t} , and $D/D\hat{t} = \partial_{\hat{t}} + \hat{\mathbf{v}} \cdot \nabla$ (see Fernández Feria 2001 or Landau et al. 1987).

The relative pressure, \hat{p} , can be written from a balance of normal stresses at the meniscus surface as $\hat{p} = \gamma \hat{k}_u - \mathbf{n} \cdot \mathbf{T}_e \cdot \mathbf{n}$, where \hat{k}_u is the curvature of the surface, $\gamma \hat{k}_u$ is the capillary pressure and \mathbf{T}_e the electric stresses tensor. The curvature of the meniscus is calculated in terms of the arc length, $\hat{s} = \int_0^{\hat{s}} \sqrt{1 + (d\hat{r}/d\hat{z})^2} d\hat{z}$, and the slope angle, θ , with $\tan \theta = d\hat{r}/d\hat{z}$: $\hat{k}_u = -d\theta/d\hat{s} + \cos(\theta)/\hat{r}$. The electric stresses are obtained from the Maxwell stress tensor, which for a continuum isotropic medium, with constant permittivity and a magnetic field negligible with respect to the electric field, is $\mathbf{T}_e = \epsilon_0(\hat{\mathbf{E}}\hat{\mathbf{E}} - 1/2(\hat{\mathbf{E}} \cdot \hat{\mathbf{E}})\mathbf{I})$ (Dulikravich et al. 1997). For a perfect conductor the electric charges are only present at the liquid surface, so the electric field is normal to its surface, $\hat{\mathbf{E}} = \hat{E}_n \mathbf{n}$, and the Maxwell tensor reduces to $\mathbf{T}_e = 1/2\epsilon_0 \hat{E}_n^2 \mathbf{n}\mathbf{n}$, where $\mathbf{n} = \nabla f/|\nabla f|$ is the unit normal to the meniscus surface pointing away from the liquid.

3.2.2 Non-dimensionalization

The problem is made non-dimensional using as characteristic dimensions the tube's diameter, D , the capillary time, $t_c = (\rho D^3/\gamma)^{1/2}$, the capillary velocity, $v_c = (\gamma/(\rho D))^{1/2}$, the capillary flow rate, $q_c = (\gamma D^3/\rho)^{1/2}$, and taking $\phi_c = Dv_c$ as the characteristic velocity potential. The characteristic voltage is selected as $\phi_0/\ln(4L/D)$ to obtain a similar non-dimensionalization for the electric field than in Chapter 2; hence, the characteristic electric field is $E_c = \phi_0/(D \ln(4L/D))$.

The problem depends then on three dimensionless parameters that are the electric Bond number, B_E , the Bond number, B , and the dimensionless flow rate, q , or injection velocity, $v_n(z = -L_N/D, r < 1/2)$, which take the form:

$$B_E = \frac{\epsilon_0 E_c^2 D}{\gamma}, \quad (3.1)$$

$$B = \frac{\rho g D^2}{\gamma}, \quad (3.2)$$

$$v_n(z = -L_N/D, r < 1/2) = \frac{4}{\pi} q. \quad (3.3)$$

3.2.3 Perfect conductor assumption

Considering a liquid and a geometry similar to that used on the experiments of Chapter 2, the time scales of the different charge transport mechanisms are the capillary time, $t_c = (\rho D^3/\gamma)^{1/2}$, which is the time scale of the liquid motion and so of charge convection, $t_e = \epsilon\epsilon_0/K$ the time scale of the charge conduction or charge relaxation, and $t_d = D^2/D_{f0}$ the time scale of charge diffusion. They can be estimated using $\epsilon = 63$, $K = 0.4$ S/m, $\rho = 1 \times 10^3$ Kg/m³, $\gamma = 40 \times 10^{-3}$ N/m, $D = 500 \times 10^{-6}$ m, and the characteristic diffusion coefficient can be estimated making use of the Einstein relation $D_{f0} = k_B Z_e T/(ze)$ for the diffusion of charged particles. k_B is the Boltzmann constant, Z_e is the electrical mobility of the ions, with $K = \hat{\rho}_e Z_e$, and ze the charge of the ions. Additionally, the temperature is $T = 298K$, and the charge density can be estimated considering that, in the experiments, all the additive (1.5 mg of hydrochloric acid per liter of solution) is completely dissociated. The characteristic charge density can be estimated then as $\hat{\rho}_e \sim 1 \times 10^5$ C/m³, and the characteristic diffusion coefficient is finally $D_{f0} \sim 1 \times 10^{-8}$ m²/s¹. With these estimates, the following time relations are obtained: $t_e/t_c \sim 1 \times 10^{-7} \ll 1$ and $t_e/t_d \sim 1 \times 10^{-10} \ll 1$. So diffusion and convection of electric charges are not important in the bulk of the liquid compared to conduction.

Nevertheless, the assumption of perfect conductor liquid is not valid in length scales $\delta \ll D$ in the following cases: (i) when $t_e \sim t_d$, but now using δ as characteristic length, which yields

¹The value reported for HCl in water in Freitas Jr. 1999 is $D_{f0} = 3.6 \times 10^{-9}$ m²/s at $T = 310$ K.

a length scale $\delta/D \sim (t_e/t_d)^{1/2} \sim 1 \times 10^{-5}$ known as the Debye length. And (ii) when $t_e \sim t_c$, again with δ as characteristic length, which yields a length scale $\delta/D \sim (t_e/t_c)^{2/3} \sim 1 \times 10^{-5}$, where charge convection is important.

Summarizing, the assumption of a perfect conducting liquid is reasonably valid for the case of highly conductive liquids used in the experiments, except for very thin layers where the liquid is in contact with the electrode, at the liquid surface or at the very tip of the conical meniscus produced by the effect of the electric stresses.

3.2.4 Inviscid liquid assumption

The assumption of inviscid liquid is reasonable for water solutions like the ones used in the experiments (Chapter 2), where the Ohnesorge number, $\text{Oh} = \mu/\sqrt{\rho\gamma D}$ is of the order of 1×10^{-2} , so viscous effects are considerably less important than the effects of inertia or capillary forces. Gravitational forces are also small, $B \sim 1 \times 10^{-2}$, and could be dropped out from the dynamic condition, although they have been maintained in the formulation.

3.3 Numerical procedure

The solution of the problem requires solving the Laplace equation for the velocity potential in the liquid, $\hat{\phi}$, and for the electric potential outside the liquid, $\hat{\phi}_e$, subjected to their corresponding boundary conditions. In what follows, we shall consider the dimensionless variables.

The Laplace's equation can be transformed into a boundary integral equation by the Boundary Element Methods, BEM, such as that in Equation 3.4 for the dimensionless liquid velocity potential ϕ . The equation needs to be solved exclusively on the boundary/contour that encloses the liquid, termed C_1 , which includes the liquid surface that is represented by the function $f(z, r) = 0$. The integral equation is numerically solved over a set of points along C_1 , including the liquid meniscus, the tube walls, and the injection zone of the tube. A number of points equal to $N = 101 + 8\text{round}(z_{tip})$ are uniformly distributed on the arc length along the meniscus, whose known positions are given by their dimensionless radial and axial coordinates, r and z respectively, and whose dimensionless velocity potentials ϕ are known. With round a function that rounds towards the nearest integer, and z_{tip} the axial position of the meniscus tip. The normal velocity, v_n is known in the tube walls, $v_n = 0$, and injection zone, $v_n = (4/\pi)q$. Thus, Equation 3.4 yields the dimensionless velocity normal to the interface on the N points, $v_n = \mathbf{v} \cdot \mathbf{n}$ (see Appendix C for more detail).

$$\begin{aligned} \phi(z_0, r_0) = & -2 \int_{C_1} G(z, r, z_0, r_0) v_n(z, r) r \, dl \\ & + 2 \int_{C_1}^{PV} \phi(z, r) G_n(z, r, z_0, r_0) r \, dl, \end{aligned} \quad (3.4)$$

where G is the appropriate Green function, see Pozrikidis 2002, $G_n = \partial_n G$, dl a differential element of length arc on C_1 , with the unit normal vector, \mathbf{n} , pointing inwards, and PV stands for the Cauchy principal value of the integral.

A similar approach is done for the dimensionless electric potential, whose corresponding boundary integral equation is shown in (3.5). The boundary C_2 encloses the outer medium, including also the liquid interface.

$$\begin{aligned} \phi_e(z_0, r_0) = & 2 \int_{C_2} G(z, r, z_0, r_0) E_n(z, r) r \, dl \\ & + 2 \int_{C_2}^{PV} \phi_e(z, r) G_n(z, r, z_0, r_0) r \, dl, \end{aligned} \quad (3.5)$$

where $E_n = -\nabla\phi_e \cdot \mathbf{n}$ is the normal dimensionless electric field on the boundary C_2 , and the unit normal vector, \mathbf{n} , points inwards. In this case Equation 3.5 provides the normal dimensionless electric field on the surface of the meniscus, known the electric potential applied to the meniscus and the tip $\phi_e = \ln(4L/D)$ (as follows from the non-dimensionalization).

Once the E_n and v_n at the meniscus surface are known, Equations 3.6 and 3.7 yield the time evolution of the meniscus surface, whereas Equation 3.8 (the dynamic condition on the interface) provides the update of the dimensionless velocity potential. These differential equations are solved using the adaptive Runge-Kutta-Fehlberg method of fourth order (see Mathews et al. 1999 and Appendix D).

$$\frac{dz}{dt} = v_z, \quad (3.6)$$

$$\frac{dr}{dt} = v_r, \quad (3.7)$$

$$\frac{d\phi}{dt} = \frac{1}{2}\nabla\phi \cdot \nabla\phi + \frac{1}{2}B_E E_n^2 - k_u + Bz + c(t), \quad (3.8)$$

with $v_r = v_s \sin\theta + v_n \cos\theta$, $v_z = v_s \cos\theta - v_n \sin\theta$, and the constant $c(t)$ is arbitrarily taken in each time step to impose a velocity potential $\phi = 0$ at the point $(r = 1/2, z = 0)$. The tangential velocity on the meniscus, v_s , is calculated by differentiating the velocity potential with respect to the arc length, $v_s = d\phi/ds$, using a central difference scheme. At the droplet's tip the condition $\lim_{r \rightarrow 0} k_2 = k_1$ is imposed, that is, the meniscus tip must end with a spherical cap ($\theta = -\pi/2$).

The simulation starts with a static hemispherical meniscus, which serves as initial condition for equations 3.6 and 3.7. Initially, the flow rate, $q(t = 0)$, is zero and $v_n(t = 0, z, r) = 0$ for all the points of the interface. This last condition is then used in equation 3.4 to obtain the velocity potential, ϕ , that is used as initial condition in equation 3.8. Once started the simulation, the flow rate is increased linearly with time until the desired flow rate is obtained at $t = 0.01$, and maintained constant afterwards. For given values of the flow rate, q , Electric Bond number, B_E , and Bond number, B , the simulations are let to evolve in time until a periodic oscillation of the meniscus is reached.

3.3.1 Global mass conservation, pinch-off condition and tip treatment

Different numerical considerations must be undertaken, additionally, for the particular simulations performed in the present chapter. It is expected that, at some times, a fraction of the meniscus is going to detach from it to form a droplet, so an algorithm needs to be implemented to allow removing the part of the simulated meniscus downstream of the axial point where a certain pinch-off condition is reached. Also, global mass conservation must be imposed on the meniscus to compensate for the round-off errors that inevitably lead to a mass imbalance after a large number of time steps.

Global mass conservation in the meniscus is imposed in each time step as follows: the volume of the meniscus is calculated at the current time step, i , as $v_i = \pi \int r^2 dz$, with z and r the position of the points forming the meniscus at the current time step. Considering the volume in the prior time step, v_{i-1} , the geometric factor C_v is calculated as,

$$C_v = \frac{v_{i-1} + q\Delta t}{v_i}, \quad (3.9)$$

with q the flow rate and Δt the current time step. C_v is now used to readjust the position of the points of the interface, being (z^*, r^*) the adjusted position, in a way that mass conservation is

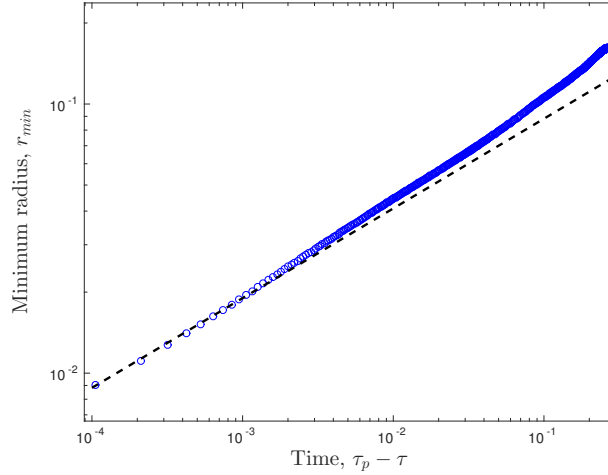


Figure 3.2: Minimum radius of the neck, r_{min} , prior pinch-off versus the time to pinch-off, $(t_p - t)$ for $q = 4.56 \times 10^{-2}$ and $B_E = 0.2$. The dashed line stands for $r_{min} \sim (t_p - t)^{1/3}$

automatically satisfied:

$$z^* = C_v^{1/3} z, \quad (3.10)$$

$$r^* = C_v^{1/3} r. \quad (3.11)$$

$$(3.12)$$

The boundary condition for $r^*(s=0) = 1$ is also imposed. It has to be pointed out that this is a very small correction since the factor $|1 - C_v|$ is in general lower than 1×10^{-6} . Nevertheless, it must be included to avoid mass imbalance after the very large number of time steps required by the simulations.

Regarding the pinch-off condition needed to remove all the fluid downstream of a given point, we select the pinch off location as that where (i) the radial position of a point of the interface is smaller than a critical radius r_c ($r < r_c$) and (ii) this point must be a local minima of $r(s)$, with s being the arc length. To find this point, in each time step we (i) adjust two splines to the radial and the axial position of the interface, $r(s)$ and $z(s)$ respectively, with respect to the arc length s . (ii) All the local minima, r_m , of $r(s)$ are identified. (iii) If the condition $r_m < r_c$ is satisfied for any minima (z_m, r_m) , all the points that satisfies that $z > z_m$ are removed from the meniscus interface. (iv) An hemispherical cusp is added to close the tip, discretized in five points, from the point (z_m, r_m) to the point $(z_m + r_m, 0)$, and assigning to those new points the values of the velocity potential, ϕ , and the normal velocity, v_n , of the pinch-off point (z_m, r_m) . After this procedure, the interface is re-gridded to maintain the number of points it had before the pinch-off, and maintaining an approximately equal arc length spacing on the meniscus by interpolating with cubic splines $r(s)$ and $z(s)$. It has to be noted that after the pinch-off the time step is automatically reduced by the adaptive Runge-Kutta method, as described in Appendix D. This time step reduction is crucial to prevent the simulations from failing after the pinch-off.

The radius r_c for the pinch-off criteria is chosen as $r_c = 5 \times 10^{-3}$ in the simulations. This value is small enough to ensure that the time and location at which the pinch-off between the ligament and the meniscus occurs, are practically the same even if smaller values of r_c are chosen. Figure 3.2 shows the evolution of the minimum radius of the neck, which forms on the meniscus before the pinch-off, as a function of the time to pinch-off in a simulated case. For a sufficiently small neck radius, the computations suggest that it goes as $r \sim (t_p - t)^{1/3}$, which implies that when $r \sim r_c = 5 \times 10^{-3}$, the time for the pinch-off to occur is of the order of $(t_p - t) \sim 1 \times 10^{-7}$, which is much smaller than any other characteristic time of interest in the problem. Interestingly, this pinch-off time scaling does not agree with the scaling provided in literature for the pinch-off of uncharged inviscid liquid ligaments, $r \sim (t_p - t)^{2/3}$ (Nitsche et al. 2004). However, this later

scaling is recovered with our model if the dripping of an uncharged droplet is computed (not shown). Nevertheless, the results plotted in Figure 3.2 are not intended to specifically analyze the pinch-off problem in detail, but just to provide some estimate of the pinch off time to support the appropriateness of using $r_c = 5 \times 10^{-3}$ as the radius at which pinch-off occurs.

Finally, during its evolution the meniscus might tends to develop conical or sharp pointed tips, as those seen in the experiments, making the electric and capillary stresses on the meniscus surface to increase dramatically as the tip is approached. Even though the meniscus tip is always forced to be a spherical cap in the model, the radius of such cap may be made as small as desired by increasing the number of nodes in which the interface is discretized, which in principle would allow simulating such conical (although artificially rounded) tips. However, increasing the number of nodes a factor of two or three dramatically rises the time required by the simulation to attain periodic conditions. From the argument given in section 3.2.3, the radius of the electro spray jet would be $r_j \sim 1 \times 10^{-5}$, so an extremely large number of nodes would be needed around the tip to describe such cone-jet transition. But even in that case, the equations would fail because the surface would cease being equipotential, so for the present model it is useless to try to describe such small geometrical features. On the other hand, the condition that both radii of curvature must be equal at the liquid tip, $\lim_{r \rightarrow 0} k_2 = k_1$, (i.e. spherical cap) becomes a source of error in the model as soon as the "real shape" requires tips sharper than that allowed by the differential arc length ds chosen for the calculations, even long before the field penetrates the liquid, or when the tip is artificially rounded after the pinch-off. This artificial geometrical imperfection of the tip leads to spurious imbalances between the capillary and electric pressures that strongly influences the dynamic of the liquid tip, resulting in the formation of spurious liquid jets when the electric stresses overcome the capillary ones, or in the formation of spurious wells at the tip otherwise. In either case, spurious capillary waves are generated that travel and propagate upstream since there is no viscosity to damp them, so the influence of this source of error in the dynamic of the oscillating meniscus is difficult to asses.

3.3.2 Electrical and capillary stresses on the meniscus surface

Figure 3.3 shows five computed dimensionless meniscus profiles, from its most retracted position to the more elongated one (prior to pinch off), for $q = 5.79 \times 10^{-2}$ (a), and for $q = 6.82 \times 10^{-3}$ (b), for $B_E = 0.2$ and $B = \times 10^{-2}$. In both cases, the evolution has reached a periodic regime. The radial and axial coordinates are made dimensionless with the nozzle diameter, D . The meniscus begins to elongate from its retracted position until it adopts a quasi-conical shape (second panel from the top in (a) and in (b)) after which tiny droplets begin to be ejected from the meniscus tip. As time advances, the meniscus develops a ligament whose tip keeps on randomly emitting bursts of tiny droplets (panels 3 and 4 in both cases). The ligaments are stretched and finally detached from the meniscus (fifth panel in both cases, just before detachment), forming a larger droplet. After the detachment the meniscus recedes violently (not shown) and the same process starts again periodically. Figure 3.3 also show the strong influence of the flow rate q on the meniscus mean volume, the length and width of the ligament and the volume of the droplets emitted from the meniscus during each oscillation. The main features are similar to those observed in the experiments, although in the later there were no ejection of small droplets prior to the detachment of the ligament (except for those invisible ones emitted by the electro spray at the conical tip, see section 3.4). This qualitative difference might be possibly due to the spurious effect caused by the way the model reshapes the ligament tip, as discussed in the previous section.

The simulations allow checking the importance of the capillary and electric stresses on each point of the meniscus surface at any stage of its oscillation, and so checking if some of the assumptions made in Chapter 2 are appropriate. Figures 3.4 to 3.6 represent the dimensionless capillary and electric stresses on the meniscus, k_u and $1/2 B_E E_n^2$ respectively, versus the dimensionless axial position, z , for some key stages of the meniscus oscillation.

Figure 3.4(a) shows a meniscus with an elongated ligament right before its detachment. The ligament is fully stretched and the neck where the capillary stresses are going to produce the

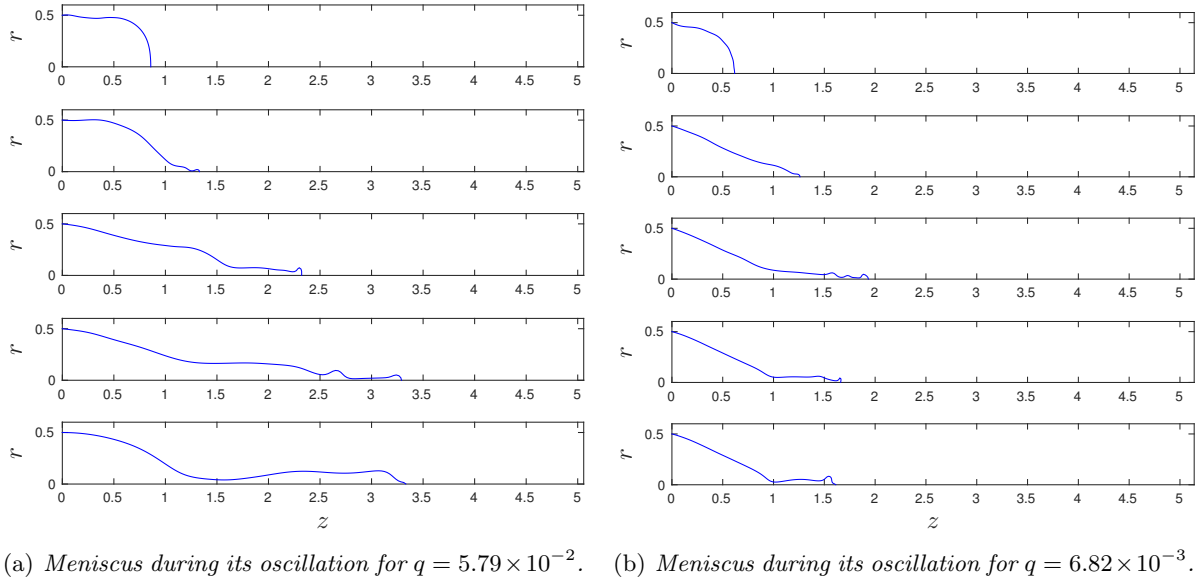


Figure 3.3: Dimensionless meniscus profile at different stages during its oscillation for two different flow rates. $B_E = 0.2$ and $B = 6 \times 10^{-2}$.

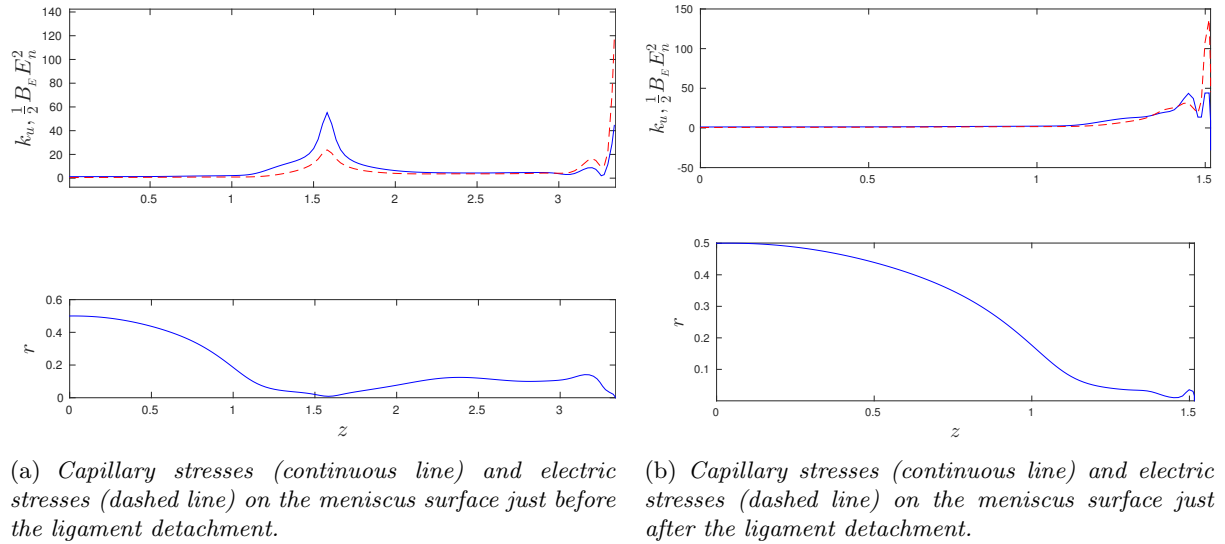
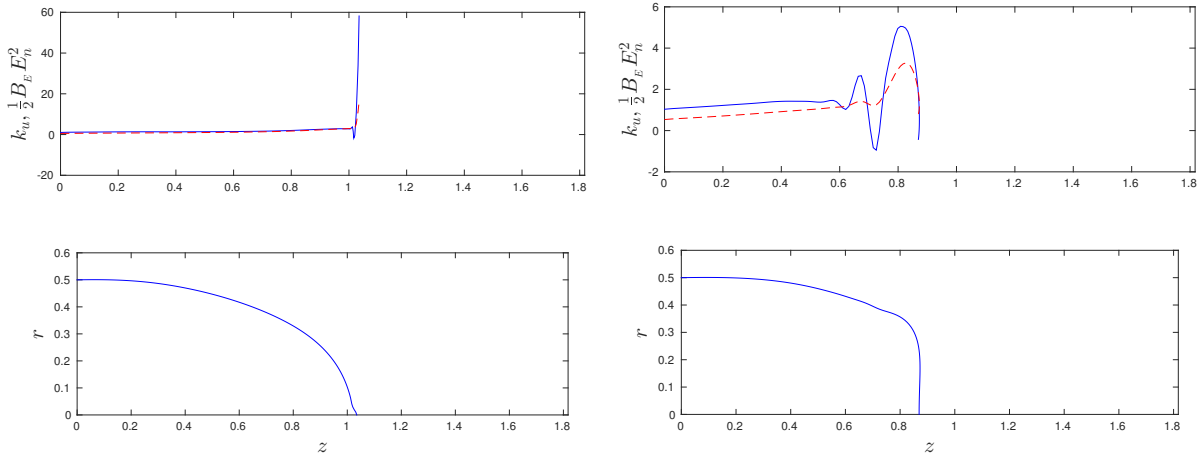


Figure 3.4: Dimensionless capillary and electric stresses on the meniscus surface just before and after the ligament detachment. $q = 5.79 \times 10^{-2}$, $B_E = 0.2$ and $B = 6 \times 10^{-2}$.

pinch off can be clearly observed. As assumed in Chapter 2, the capillary and electric stresses balance each other along the ligament, where they remain constant, whereas the capillary stresses dominates on the neck and the electric ones dominate on the tip. Right after the detachment, see Figure 3.4(b), the electric stresses at the tip become stronger than the capillary ones, leading to the ejection of tiny droplets from the meniscus tip until the capillary stresses take over and the meniscus begins to recede violently with a velocity of the order of the capillary velocity. This feature is not observed in the experiments, where there is no emissions from the meniscus tip after the detachment of the ligament, and it is probably due to the numerical errors linked to the artificially rounded tip, as commented before. The beginning of the recession period is shown in Figure 3.5(a). As mentioned before, the capillary stresses become dominant at the tip leading to a retraction of the meniscus. Figure 3.5(b) shows an instant where the retraction velocity is of the order of the capillary velocity. Some capillary waves may be identified. After the retraction, the meniscus elongates again, Figure 3.6(a), and a rounded tip is formed later on, Figure 3.6(b), when the electric stresses begin to take over at the tip. Capillary waves can be observed. In



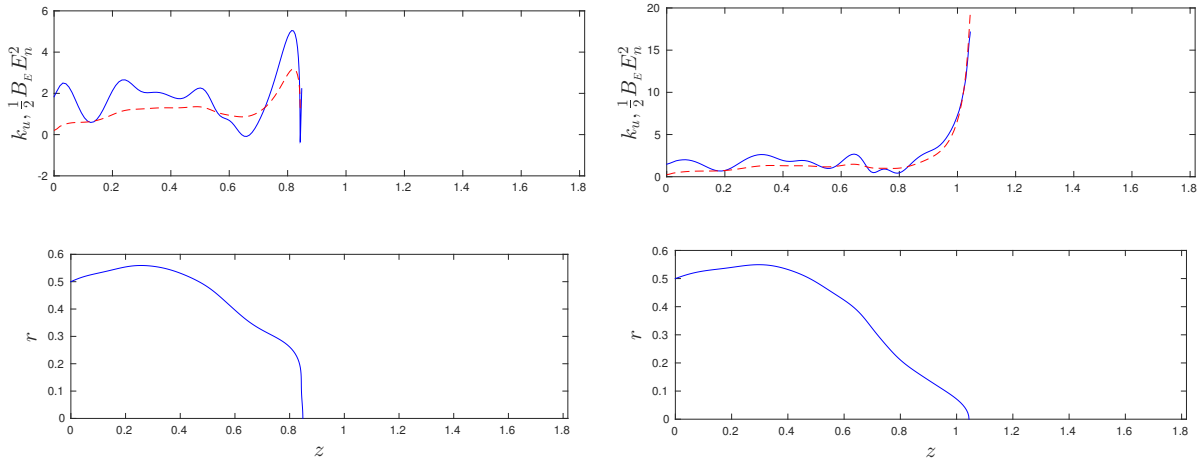


(a) Capillary stresses (continuous line) and electric stresses (dashed line) on the meniscus surface during the first stages of the retraction.

(b) Capillary stresses (continuous line) and electric stresses (dashed line) on the meniscus surface during its violent retraction.

Figure 3.5: Dimensionless capillary and electric stresses on the meniscus surface in different stages during its retraction. $q = 5.79 \times 10^{-2}$, $B_E = 0.2$ and $B = 6 \times 10^{-2}$.

subsequent times, small droplets will start being ejected from the tip and the ligament begins to form.



(a) Capillary stresses (continuous line) and electric stresses (dashed line) on the meniscus surface when it starts to elongate after the retraction stage.

(b) Capillary stresses (continuous line) and electric stresses (dashed line) on the meniscus surface when a pointed tip starts to form at its tip.

Figure 3.6: Dimensionless capillary and electric stresses on the meniscus surface in different stages during its elongation. $q = 5.79 \times 10^{-2}$, $B_E = 0.2$ and $B = 6 \times 10^{-2}$.

3.4 Comparison with experiments

The simulations have been performed for $B_E = 0.2$, $B = 6 \times 10^{-2}$ and a range of dimensionless flow rates, q , from 6.3×10^{-4} up to 1.5×10^{-1} to compare them with the experiments of Chapter 2. The simulations start with an initial hemispherical meniscus that inflates while being fed at constant flow rate. The electric stresses pull the meniscus, giving it an ellipsoidal-like shape as it continuously grows in volume. After some time, the electric stresses start tearing off a small mass of liquid from the meniscus tip while it keeps on growing and elongating. At some point, a periodic state is reached, where the volume that enters the meniscus during a period of the

oscillation equals the volume emitted from it in the form of droplets during that period. These processes can be observed in Figure 3.7(a) for a case in which $q = 7.35 \times 10^{-2}$, $B_E = 0.2$ and $B = 6 \times 10^{-2}$. It represents the dimensionless meniscus volume, v_{ol} , versus the dimensionless time, t . The dotted line corresponds to the computed results whereas the solid line collects experimental results for the same conditions when the periodic microdripping is obtained. It is interesting to note that the values of v_{ol} and the oscillation period is well captured by the simulations. However, it is also clear that the detail of the emissions is not.

Figure 3.7(b) shows the dimensionless axial position of the meniscus tip, z_{tip} , versus the dimensionless time t . The dotted line represents the computed values and the solid line represents the experiment. Whereas in the experiments there is apparently just one droplet emitted at the end of each oscillation, indicated by the steep fall of z_{tip} , the simulations yield two or three burst of emissions of tiny droplets at a very high frequency while the meniscus elongates, as indicated by the highly oscillating parts of z_{tip} , before a much larger droplet is eventually emitted at the end of the period. The inset in Figure 3.7(b) shows the blown up of one of these high frequency bursts.

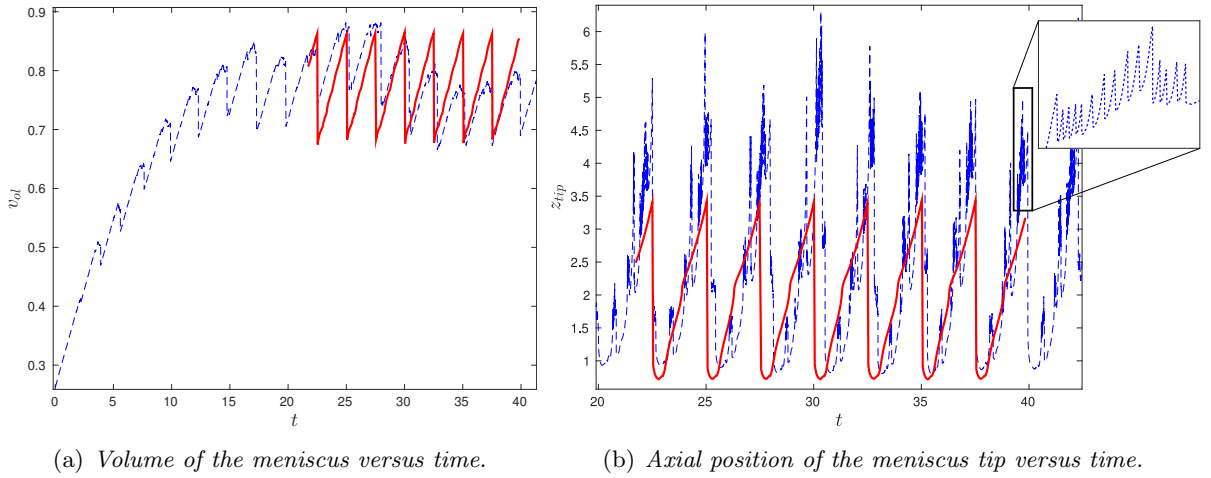


Figure 3.7: Temporal evolution of the meniscus volume and the axial position of the tip for $q = 7.35 \times 10^{-2}$, $B_E = 0.2$ and $B = 6 \times 10^{-2}$. Solid line for experiments and dashed line for simulations.

A more detailed comparison between the experimental and numerical values of z_{tip} with time t is shown in Figure 3.8 for $q = 5.79 \times 10^{-2}$, $B_E = 0.2$ and $B = 6 \times 10^{-2}$. The time offset between the experimental curve (dotted line) and the numerical one (continuous line) has been manually adjusted to kind of overlapping both curves. This figure includes pictures of the experimental meniscus shape corresponding to the time location where the arrows point at. As mentioned before, the experimental result yields a single drop, indicated by the sudden drop of z_{tip} . When analyzed in more detail, one observes how the experimental curve z_{tip} versus t increases smoothly from the beginning (left most point in the curve) when, suddenly, its slope presents an abrupt drop around $t \sim 111.35$ in this case. This jump in the slope of $z_{tip}(t)$ occurs when the meniscus develops the conical tip, as indicated by the corresponding picture. In this case, the conical tip persists even after the ligament detaches from the meniscus (right most picture). It seems reasonable to expect that the intense space charge in front of the meniscus, caused by the electro spray of invisible droplets emitted from its conical tip, deforms, decreases or limits the electric field acting on a region close to the tip of the ligament, thus explaining why the velocity of the tip suddenly slows down. Therefore, it seems that the main difference between the simulations and the experiments lays on the dynamic of the tip that the present model is unable to describe, as mentioned before, and also on the existence of a strong space charge due to the electro spray emitted from the conical tip, which is not taken into account in the model.

Figure 3.9 shows the experimental evolution of the tip velocity, v_{tip} , made dimensionless with

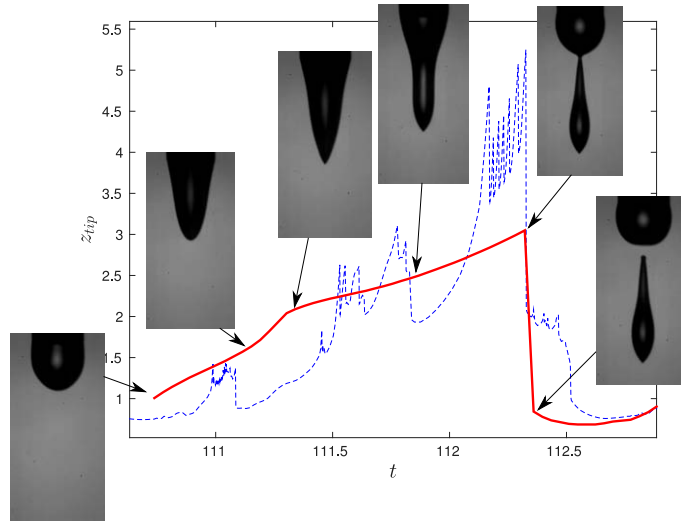


Figure 3.8: Temporal evolution of the axial position of the tip for $q = 5.79 \times 10^{-2}$, $B_E = 0.2$ and $B = 6 \times 10^{-2}$. Solid line for experiments and dashed line for simulations.

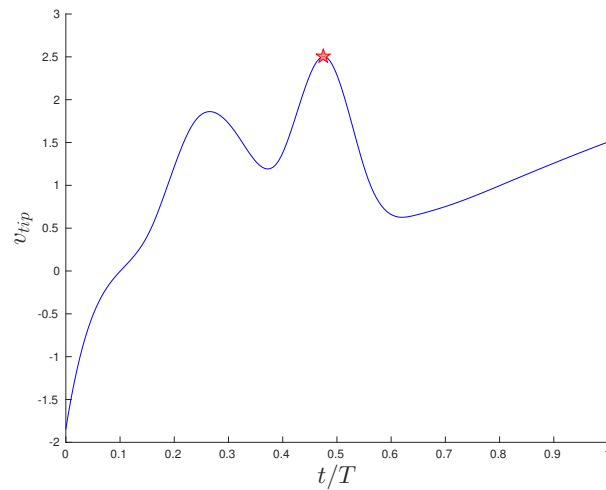
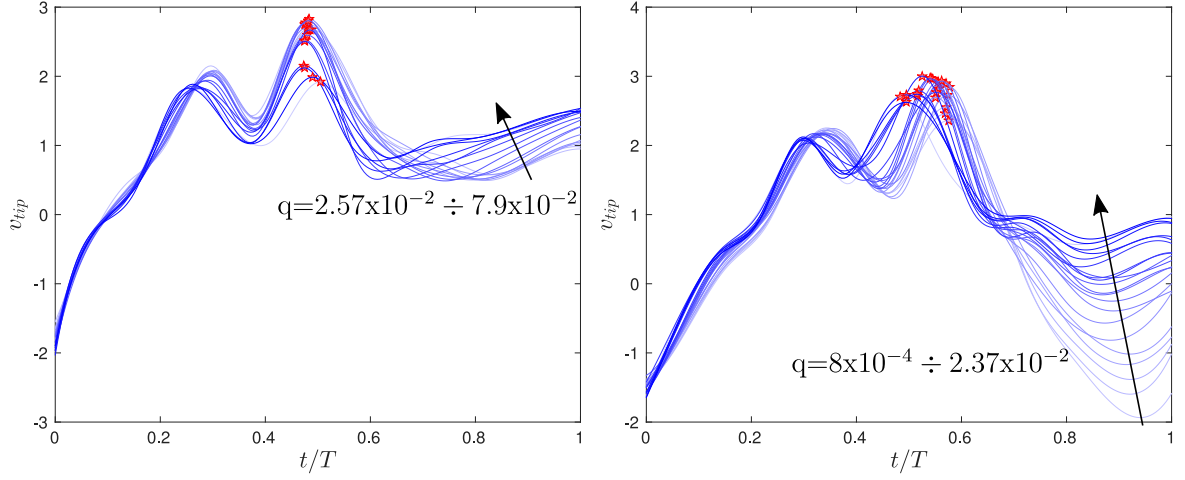


Figure 3.9: Temporal evolution of the dimensionless velocity of the tip, v_{tip} , in a cycle of the meniscus oscillation for $q = 5.79 \times 10^{-2}$, $B_E = 0.2$ and $B = 6 \times 10^{-2}$. A pentagon symbol indicates the moment at which an electro spray starts to be emitted from the meniscus tip. T is the dimensionless period of the oscillation.



(a) Temporal evolution of the dimensionless velocity of the tip, v_{tip} , in a cycle of the meniscus oscillation for dimensionless flow rate varying from $q = 2.57 \times 10^{-2}$ up to $q = 7.9 \times 10^{-2}$. (b) Temporal evolution of the dimensionless velocity of the tip, v_{tip} , in a cycle of the meniscus oscillation for dimensionless flow rate varying from $q = 8 \times 10^{-4}$ up to $q = 2.37 \times 10^{-2}$.

Figure 3.10: Temporal evolution of the dimensionless velocity of the tip, v_{tip} , in a cycle of the meniscus oscillation for different dimensionless flow rate. Darker solid lines are for higher flow rates, and pentagon symbols indicate the moment at which an electrospay starts to be emitted from the meniscus tip. $B_E = 0.2$ and $B = 6 \times 10^{-2}$. T is the dimensionless period of the oscillation.

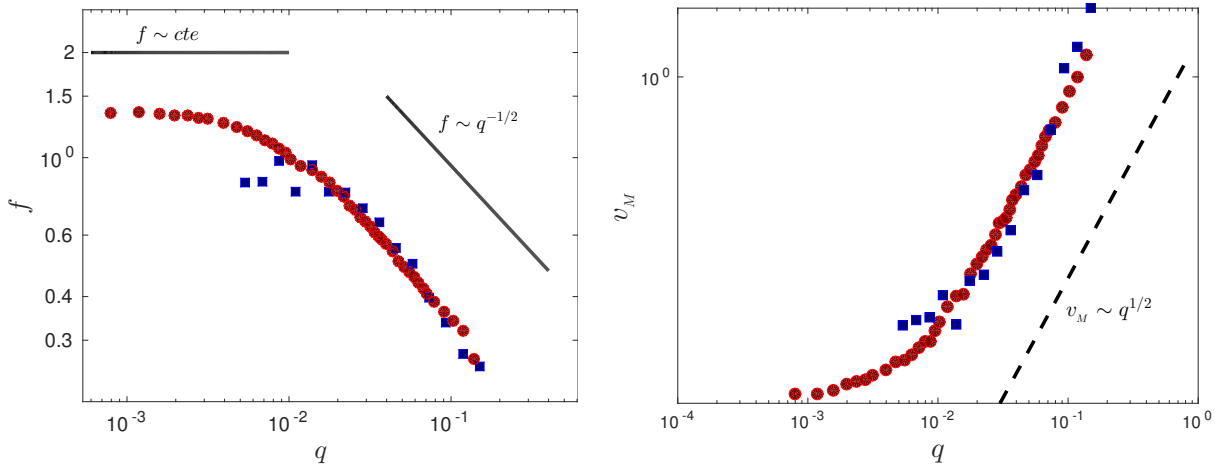
the capillary velocity, v_c , versus the time made dimensionless with the oscillation period, T , for the same case of Figure 3.8 ($q = 5.79 \times 10^{-2}$, $B_E = 0.2$ and $B = 6 \times 10^{-2}$). The starting time is set at the instant when the ligament detaches from the meniscus. The symbol (star) indicates the time location when the conical tip develops. At the beginning, the tip velocity is negative, indicating the recession of the meniscus after the detachment of the ligament. At $t/T \sim 0.1$ the tip velocity is zero, indicating the time at which the recession part of the oscillation ends. Between $t/T \sim 0.1$ and $t/T \sim 0.5$ the meniscus grows and its tip remains rounded, although its tip velocity does not grow monotonically: a noticeable hump near $t/T \sim 0.3$ may be easily identified, although there are one more hump, much more subtle, around $t/T \sim 0.15$. These humps are caused by capillary waves reflecting back and forth from the meniscus base at the needle rim, which may be clearly seen in the videos. At $t/T \sim 0.5$, when the conical tip develops, the tip velocity suffers a sudden drop, jumping from $v_{tip} \sim 2.5$ to $v_{tip} \sim 1$, to grow again with time, but much smoothly than before, until the end of the oscillation. As shown in Figure 3.10 (a), very similar results are obtained from the experiments for moderate and large values of q while keeping constant $B_E = 0.2$ and $B = 6 \times 10^{-2}$: the conical tip develops somewhere close to $t/T \sim 0.5$ and the dimensionless tip velocity drops from $v_{tip} \sim 2.2 - 2.8$ down to $v_{tip} \sim 1$ to remain relatively constant until the end of the oscillation.

Figure 3.10(b) shows experimental values of $v_{tip}(t)$ for the smaller flow rates keeping $B_E = 0.2$ and $B = 6 \times 10^{-2}$. The first half of the cycle is very similar to the case of moderate and large flow rates, Figure 3.10(a). The conical tip also appears around $t/T \sim 0.5$, but as q decreases v_{tip} also decreases for dimensionless time larger than 0.5, in contrast with the case of larger flow rates. The main reason is the length of the ligament. Whereas for moderate and large flow rates the dimensionless length of the ligament, ℓ_s , is of order one or larger, for sufficiently small flow rates one obtains that $\ell_s < 1$. When $\ell_s \geq 1$ the dynamic of the tip of the ligament becomes almost independent of the oscillation of the meniscus, whereas for $\ell_s < 1$ the motion of the tiny ligament is linked to the oscillation of the meniscus, so the tip tends to move as the meniscus does.

For our inviscid liquid, one may assume that the velocity of the tip as the elongation of the meniscus proceeds is caused by the electric suction, so that $\rho \hat{v}_{tip}^2 \sim \epsilon_0 \hat{E}_{tip}^2$, from which one

obtains $\hat{E}_{tip} \sim (\rho/\epsilon_0)^{1/2} \hat{v}_{tip}$ or, in dimensionless form, $E_{tip} \sim v_{tip}/B_E^{1/2}$. With this hypothesis, Figures 3.9 and 3.10 are just a re-scaled measurement of E_{tip} versus time. In this case, E_{tip} drops down as soon as the conical tip forms, and remains relatively constant until the detachment of the ligament. The electric field given by Taylor is expressed as $\hat{E}_T = (2\gamma/(r\epsilon_0 \tan \alpha_T))^{1/2}$, where $\alpha_T = 49.23^\circ$ is Taylor's angle. For the liquid used, and taking a characteristic value of $r = D/4$ as the radius of the ligament at the instant in which the conical tip develops, one obtains a dimensionless Taylor field $E_T \approx 6$ that would induce a tip velocity $v_{Ttip} \approx 2.6$. This estimate is consistent with the idea that the formation of an electrospay at the conical tip limits the ligament tip velocity. The fact that the field at which the conical tip forms is relatively constant might be understood since for highly conducting liquids, like the ones used here, the details of the cone-jet-electrospray are relatively independent of the surroundings, and so is the electric field on the Taylor cone.

In the computed case, however, the tip accelerates to dimensionless velocities much larger than 2.8 and much faster than in the experimental cases. This is clearly seen from Figure 3.8, where before each burst the slope of the discontinuous line (computed one) representing $z_{tip}(t)$ becomes much steeper than the maximum slope of the continuous line (i.e., when the conical tip forms). The bursts are preceded by the formation of a (spurious) jet, possibly caused by the artificial rounded tip forced by the model. Accordingly, this results in spurious values of E_{tip} , much larger than the real ones, due to the shape of the tip imposed in the model and, perhaps, also overestimated due to the absence in the model of the electrospay-space charge. Therefore, the details of the dynamics of the ligament tip cannot be correctly reproduced.

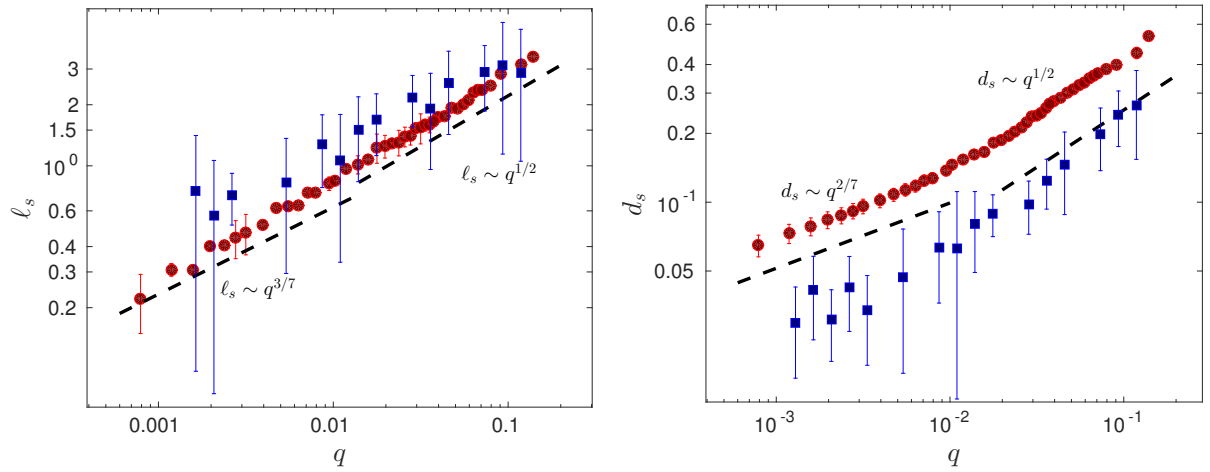


(a) Dimensionless frequency of the oscillation, f , versus the dimensionless flow rate, q . Circles for the experiments and squares for the simulations.

(b) Dimensionless meniscus mean volume per oscillation, v_M , versus the dimensionless flow rate, q . Circles for the experiments and squares for the simulations.

Figure 3.11: Evolution of the dimensionless frequency of the oscillation and the dimensionless mean volume of the meniscus versus the dimensionless flow rate. $B_E = 0.2$ and $B = 6 \times 10^{-2}$.

Nevertheless, more global quantities, such as meniscus dimensionless volume, v_{ol} , and oscillation dimensionless frequency, f , are reproduced rather well for most cases, suggesting that the errors associated to the tip does not affect much the dynamic of the meniscus. Figure 3.11 shows the dimensionless oscillation frequency, f , and the dimensionless meniscus mean volume, v_M , versus the liquid flow rate q . The circles represent the experimental results whereas the squares represent the numerical results. For moderate and large flow rates, $q \geq 10^{-2}$, the simulations reproduce the experimental results. However, for the smaller flow rates the simulations underestimate f and overestimate v_M . The simulations also appear to yield a plateau of both f and v_M for flow rates smaller than $q = 1 \times 10^{-2}$ whereas in the experiments the plateau is attained at around $q = 1 \times 10^{-3}$. The simulations cease to yield periodic microdripping (axial mode II) for flow rates smaller than $q \approx 5 \times 10^{-3}$. For smaller flow rates, the simulations yield axial mode I instead: meniscus oscillation with interspersed emissions of droplets and stages



(a) Dimensionless ligament length ℓ_s versus the dimensionless flow rate q .

(b) Dimensionless ligament mean diameter d_s versus the dimensionless flow rate q .

Figure 3.12: Dimensionless ligament length ℓ_s and ligament mean diameter d_s versus the dimensionless flow rate q . Circles for the experiments and squares for the simulations. $B_E = 0.2$ and $B = 6 \times 10^{-2}$.

with no emission. This result is not surprising since the simulated meniscus in axial mode II always exhibit spurious bursts of emissions of droplets as the ligament forms, thus emptying the ligament itself. As $q \rightarrow 1 \times 10^{-3}$, the drainage due to the bursts reduces in excess the volume of the ligament and eventually prevents the pinch off, whereas in the experiments the volume of liquid emitted in the form of ultra fine aerosol is almost negligible, so the ligament does not have any appreciable drainage.

The effect of this drainage due to the emission of droplets as the ligament forms may be clearly seen in Figures 3.12. Figures 3.12(a) and 3.12(b) show, respectively the dimensionless length and diameter of the ligament, ℓ_s and d_s , before pinch off versus the dimensionless flow rate q . The circles represents experiments whereas the squares represents simulations. In this case $B_E = 0.2$ and $B = 6 \times 10^{-2}$. The computed values of ℓ_s are larger than the experimental ones, as expected from the discussion about the velocity of the ligament tip. On the other hand, the computed values of d_s are considerably smaller than the experimental ones. This is due to the continuous drainage brought about by the bursts suffered by the simulated ligament during the oscillation. The same may be concluded from Figure 3.13. It plots the equivalent dimensionless diameter of the droplet, d_d , formed after the ligament detaches from the meniscus, versus the flow rate q . Circles represent experiments whereas the squares represent simulations. As expected, the simulations notably under estimate the experimental results because of the spurious drainage effect. In the same figure 3.13, the crosses stand for the dimensionless droplet volume obtained by resorting to mass conservation through the flow rate q and the oscillation frequency f obtained from the simulation. The crosses match very well the experimental results. It is not surprising since the computed f reproduces very well the experimental ones, so application of mass conservation leads to the correct droplet size.

3.5 Conclusions and future works

An inviscid, perfectly conducting liquid has been used to model the axial mode II (periodic microdripping) regime, in the needle-plate electric configuration, neglecting the effect of the droplets emitted during the oscillations. Under these hypotheses, the equations governing the liquid dynamics and the electric field are the Laplace equation for the velocity and electric potentials. Those are solved by the Boundary Element Method (BEM).

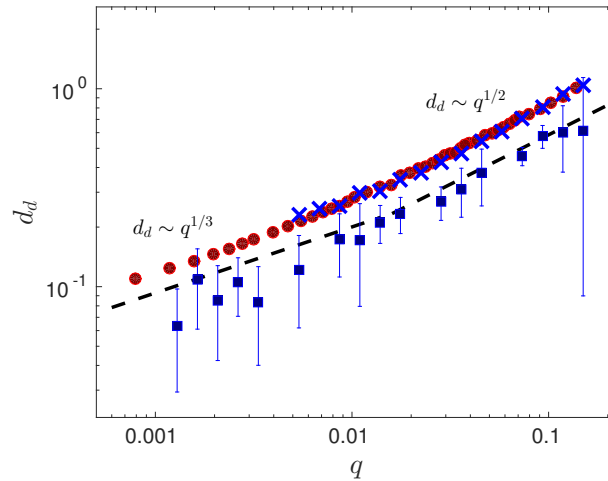


Figure 3.13: Equivalent diameter of liquid emission per meniscus oscillation. Circles for the experiments and crosses for the simulations. Squares represent the equivalent diameter of the volume emitted in the main ligament developed in each period. $B_E = 0.2$ and $B = 6 \times 10^{-2}$.

The results of the simulations agree qualitatively well with the experiments. As time advances, the meniscus elongates and forms a relative narrow tip that eventually forms a ligament. As the ligament stretches, bursts of droplets are randomly emitted from the tip of the ligament. At some further time the ligament detaches from the meniscus. The meniscus then recedes and the process repeats itself periodically.

Some of the assumptions made in Chapter 2 have been checked. As expected, the electric stresses are of the order of the capillary stresses in the ligament, except at the tip and the neck. The electric stresses are dominant in a zone around the ligament tip whereas the capillary stresses dominate on the neck, eventually leading to the ligament pinch off. After the ligament detaches from the meniscus, the capillary stresses become dominant in all the meniscus and the meniscus retracts violently at a velocity of the order of the capillary velocity. Capillary waves are formed on the meniscus while it starts to elongate again and the electric stresses take the control of the tip producing a pointed quasi conical tip from which small droplets begin to be emitted again.

The simulations have been compared with the experimental results of Chapter 2. The computed values of the oscillation frequency f and the meniscus mean volume v_M for moderate and large flow rates agree very well with the experimental results. However, the details of the evolution of the ligament are not captured. The bursts of droplets that randomly occur on the simulations do not happen in the experiments. The reason lays mainly on the limitations of computing the details of the ligament tip, which is artificially rounded leading to spurious imbalances between the electric and capillary stresses at the tip. This effect is combined with the existence, in the experiments, of a strong space charge that is not included in the present model. This space charge is generated by the electrospray emitted from the Taylor cone that forms at the tip of the ligament in the experiments. This particular structure seems to limit the maximum electric field pulling the ligament. As a consequence, the computed ligaments are exposed to stronger electric fields on their tip, so they become longer, thinner and have a smaller volume than the experimental ones due to the spurious bursts of emissions, so the droplets formed after the ligament pinch off are smaller than the experimental ones. The disagreement increases as the flow rate decreases. Nevertheless, the droplet size may be obtained with good precision by combining the computed frequency f with mass conservation.

The minimum flow rate for axial mode II obtained from the simulations is overestimated. This is due to the continuous mass drainage that experiences the computed ligament as bursts of droplets are randomly emitted from its tip, whereas in the experiments an almost negligible mass is emitted from the conical tip, which forms at the tip of the ligament, in the form of an

ultra fine aerosol.

Future works are, then, necessary to correctly compute the variables near the tip and to include the effect of the structure space charge emitted from the Taylor cone that forms at the ligament tip for a non-negligible part of the oscillation period. Perhaps the large scale disparity between the dimensions of the ligament and those of the cone-jet-electrospray for highly conducting liquids, such as the ones used in this work, might allow treating at least to a first order this effect.

References

- Cloupeau, M. & Prunet-Foch, B. 1994. Electrohydrodynamic spraying functioning modes: a critical review. *J. Aerosol Sci.* 25(6), 1021–1036.
- Dulikravich, G. S. & Lynn, S. R. 1997. Unified Electro-Magneto-Fluid (EMFD): A Survey of Mathematical Models. *Int. J. Nonlinear Mech.* 32(5), 923–932.
- Fernández Fera, R. 2001. *Mecánica de fluidos*. Universidad de Málaga / Manuales.
- Fernández de la Mora, J. & Loscertales, I. G. 1994. Current emitted by highly conducting Taylor cones. *J. Fluid Mech.* 260, 155–184.
- Freitas Jr., R. A. 1999. *Nanomedicine, Volume I: Basic capabilities*. Landes Bioscience, Georgetown, TX.
- Higuera, F. J. 2003. Flow rate and electric current emitted by a Taylor cone. *J. Fluid Mech.* 484, 303–327.
- Higuera, F. J. et al. 2013b. Pulsating emission of droplets from an electrified meniscus. *J. Aerosol Sci.* 66, 193–208.
- Juraschek, R. & Röllgen, F. 1998. Pulsation phenomena during electrospray ionization. *Int. J. Mass Spectrom.* 177, 1–15.
- Krupa, A & Jaworek, A. 1999. Spherical Probe for Measuring Aerosol Mass Flow Rate. *J. Aerosol Sci.* 30(1), 377–378.
- Landau, L. D. & Lifshitz, E. 1987. *Fluid Mechanics; 2nd Edition*. Vol. 6. Butterworth-Heinemann.
- Marginean, I., Nemes, P., & Vertes, A. 2006b. Order-chaos-order transitions in electrosprays: The electrified dripping faucet. *Phys. Rev. Lett.* 97(6), 064502.
- Mathews, J. H. & Fink, K. D. 1999. *Numerical methods using MATLAB*. Vol. 31. Prentice hall Upper Saddle River, NJ.
- Nitsche, M. & Steen, P. H. 2004. Numerical simulations of inviscid capillary pinchoff. *Journal of Computational Physics* 200(1), 299–324.
- Pozrikidis, C. 2002. *A practical guide to boundary element methods with the software library BEMLIB*. CRC Press, Inc. Boca Raton, FL, USA.

Chapter 4

Electro-coflowing emissions

Contents

4.1	Introduction	47
4.2	Problem description and experiments	48
4.3	Results	49
4.3.1	Phase diagram in electro-coflow	49
4.3.2	Effect of the viscosity of the outer liquid.	52
4.3.3	Oscillatory regime in electro-coflow and comparison with microdripping regime in air	53
4.4	Conclusions and future works	59
	References	60

4.1 Introduction

The generation of emulsions is a regular procedure to synthesize particles in the micron size regime. One inexpensive way of doing so resorts to glass microfluidic devices operated in the so-called coflow configuration. It consists of a capillary tube in which a thinner capillary tube is coaxially located. This thinner tube is usually a borosilicate tube whose end has been pulled to form a tip that may have a diameter between a few and hundreds of microns. A liquid flows through the annular gap between the concentric tubes, whereas a second liquid, immiscible with the first one, is forced through the inner tube. For given tube sizes and fluid properties (density, viscosity, and surface tension) the controlling parameters are the liquid flow rates. Thus, for given density and viscosity ratios, the outcome is controlled by the flow rates, or in dimensionless form, by the Weber and Capillary numbers. In its most typical configuration, the viscous drag the outer liquid exerts on the meniscus of the inner liquid sticking out of the tip may overcome the capillary stress, thus pulling a liquid ligament whose diameter decreases as it develops downstream. This is the so-called jetting mode in the thinning regime, and it is a simple way to generate droplets that may be smaller in diameter than the tip. There are many other modes (Guerrero et al. 2014; Castro-Hernández et al. 2009; Utada et al. 2007) but they are not in the scope of this work. In brief, the scaling laws for this jetting in thinning regime indicate the possibility of generating tiny droplets from large tips, but it also states the difficulty of reaching the sub-micron size regime.

On the other hand, it is well known that the electrospray in the cone-jet mode is an easy mean to generate droplets or fibers (liquid ligaments) that may easily reach the sub-micron size regime. It is, therefore, promising to combine both techniques, coflow and electrospray, to try to generate droplets from a single device, but whose diameters may now span from hundred of microns down to the sub-micron regime.



The novelty is, therefore, including the electric forces within the microfluidic device. To that end Gundabala et al. 2010 (Gundabala et al. 2013) developed a novel microfluidic device, in which a third liquid, immiscible with the first one, is injected counterflow through a third capillary tube, also axially located inside the first capillary tube, see Fig. 4.1(a). This third liquid, the liquid collector, forms an interface with the first liquid, the outer one. This interface is steady, but flows downstream dragged by the outer liquid. Then, if the outer fluid is a dielectric and the collector one is a conductor, one can apply a voltage difference between the collector fluid and the inner fluid (the one that will form the droplets), as sketched in Figs. 4.1. The thus formed highly charged droplets will swim towards the liquid interface (the liquid collector), where they will loose their charge. The velocity of the interface will drag the uncharged droplets away downstream.

This Chapter is dedicated to the experimental characterization of this novel glass microfluidic device when the atomization is mostly due to the action of the electric stresses. Different emission regimes are observed when different ranges of the controlling parameters are swept, and among them appears a pulsating regime similar to the microdripping regime studied in Chapter 2. Under this regime, droplets are generated whose diameter is smaller than the diameter of the tip of the inner tube.

4.2 Problem description and experiments

To search the microdripping regime in electro-coflow and to characterize the generation of emulsions in this regime, a microfluidic device such as the one used by Gundabala et al. 2010 and Utada et al. 2005 has been fabricated. The device, sketched in figure 4.1, has been fabricated using borosilicate glass capillaries. The tip of a glass tube of 2 mm of outer diameter has been pulled and cut by means of the equipment described in appendix A to a tip diameter of around 50 μm . This tube, labeled as *inner glass tube* in figure 4.1(a), has been introduced inside another glass tube of square section of 2 mm of inner side labeled as *outer glass tube*. A third glass tube of 2 mm of outer diameter, the *collector glass tube*, has been also introduced inside the *outer glass tube* through the opposite side as the *inner glass tube*, and located at a distance of 1.5 mm from the pulled tip.

A flow rate, \hat{q}_i , of ethylene glycol has been forced through the *inner glass tube* by means of a pressurized tank. Another pressure driven flow rate, \hat{q}_o , of silicone oil, acting as coflowing liquid, flows through the gap between the outer diameter of the *inner glass tube* and the inner square section of the *outer glass tube*. Another flow rate of ethylene glycol, \hat{q}_{col} , is pressure driven, in counterflow configuration, through the *collector glass tube*. The flow rate of the collector is set to form a rounded and steady liquid interface between the outer and collector liquids, located at a distance of 1 mm from the inner tube tip.

It is important to notice that this three-fluid system is very sensitive to variations of pressure in the feeding systems, so special care must be taken to ensure the steadiness of the liquid collector interface. It would be preferable to fix the flow rates with syringe pumps to overcome these stability problems.

The conductivity of the ethylene glycol, 1.07×10^{-4} S/m in this case, and the practically dielectric silicone oil allows setting up an electric field between the meniscus of the inner liquid at the *inner glass tube* tip, connected at a voltage $\hat{\phi}_0$, and the liquid collector connected at ground voltage. Thus, by varying the outer flow rate and the electric field one may observe different emission regimes produced in electro-coflow. The properties of the liquids used have been obtained from the literature, and are listed in the table 4.1. The interfacial tension, $\gamma = 17.5 \pm 0.4$ mN/m has been measured by the pendant drop method at 20°C.

Once the geometry and the liquids are established, the governing parameters are the inner and outer flow rates, \hat{q}_i and \hat{q}_o respectively, along with the voltage applied to the inner liquid, $\hat{\phi}_0$. These parameters have been swept to make a phase diagram of the emissions in electro-coflow. The emissions from the meniscus tip have been recorded with a high speed camera and,

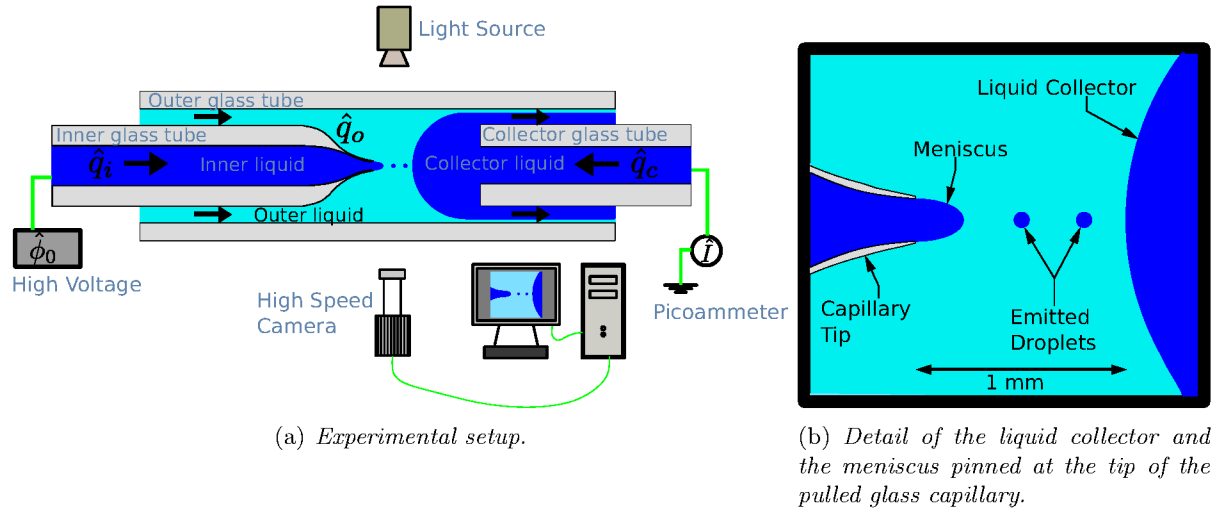


Figure 4.1: Experimental setup in electro-coflow.

Liquid	μ [mPa s]	ρ [Kg m ⁻³]	K [S m ⁻¹]
Ethylene glycol	16.9 ⁽²⁾	1113 ⁽¹⁾	1.07×10^{-4} ⁽¹⁾
Silicone oil (PDMS) 10 cSt	9.3 ⁽²⁾	930 ⁽²⁾	-

Table 4.1: Properties of ethylene glycol, Scharlau 99.5 %, and silicone oil 10 cSt, Sigma-Aldrich, at ⁽¹⁾20°C, ⁽²⁾25°C. Viscosity, μ , density, ρ , and conductivity, K . The interfacial tension between the ethylene glycol and silicone oil is $\gamma = 17.5 \pm 0.4$ mN/m, measured at 20°C.

particularly, a region of the governing parameters has been found where a regime similar to that of microdripping in air appears.

4.3 Results

4.3.1 Phase diagram in electro-coflow

Different kinds of emissions have been observed when the inner, \hat{q}_i , and outer, \hat{q}_o , flow rates, and the voltage, $\hat{\phi}_0$, are swept. In a first approach, these emission regimes can be classified as dripping and jetting emissions. The viscosity of the outer liquid plays an important role in the jet formation and the development of whipping instabilities (Riboux et al. 2011; Guerrero et al. 2014), allowing to observe these instabilities smoothly. In the whipping instabilities the electrified jet emitted from the meniscus of the inner liquid tend to bend in an off-axis direction due to the self repulsion of the charges along the jet. The movement of the jet, which is quite violent and chaotic in air, is smoothed by the viscosity of the outer liquid taking a helicoidal structure.

The emission regimes observed in electro-coflow are represented in figure 4.2 for different outer flow rates when the inner flow rate and the voltage are swept. These emission can be classified as electro-dripping, zone I, oscillating meniscus, zone II, and jetting emissions, zones III and IV. There is an upper limit in the phase diagrams where the voltage applied to the inner liquid is so high that the interface of the collector becomes unstable and charged jets are emitted from it. In the electro-dripping regime (zone I), figure 4.3(a), droplets are emitted from the tube tip. The droplet size is considerably bigger than the tube tip diameter and the frequency of droplet emission is lower than that of other emission regimes. As the voltage applied to the inner liquid increases, the frequency of the droplet emission increases and the droplet size decreases until, for a given voltage difference, a transition to an oscillating meniscus regime is established, termed zone II. In this zone II three sub-zones have been identified, zones a, b and c, as a

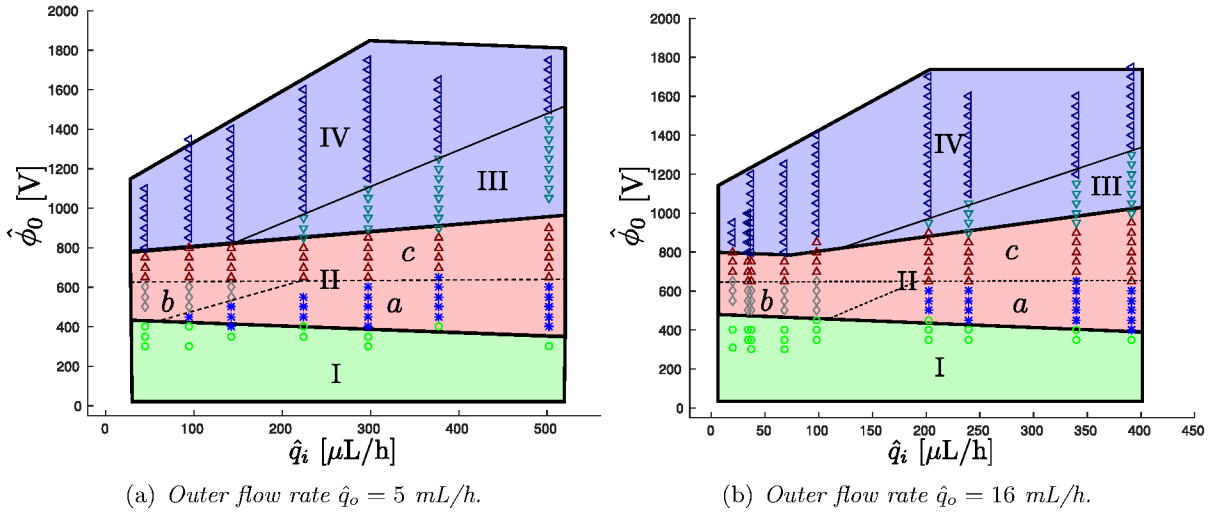


Figure 4.2: Phase diagram of the emissions in electro-coflow for different inner flow rates, \hat{q}_i and voltage applied to the inner liquid, $\hat{\phi}_0$. The outer medium is silicone oil, with a viscosity of $9.3 \times 10^{-3} \text{ Pa s}$. Zone I for electrodrinking, zone II for oscillating meniscus, and zones III and IV for jet emissions.

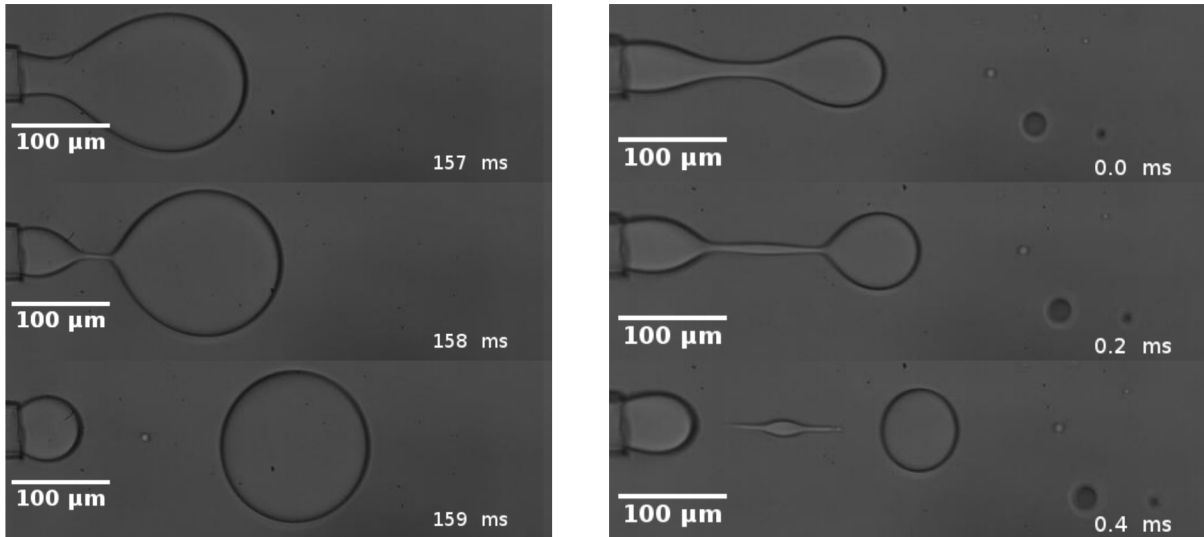


Figure 4.3: Emissions in electro-coflow: electrodrinking and transition to a oscillating meniscus.

matter of different details during the emission. In sub-zone *a*, Figure 4.3(b), a meniscus of the inner liquid is pinned to the tip of the inner tube. This meniscus, when fed with the flow rate \hat{q}_i and connected to high voltage $\hat{\phi}_0$, elongates; from its tip, a droplet of diameter of the order of the tube tip diameter detaches. After the detachment, the meniscus recedes and then starts to elongate again and the cycle repeats itself in a periodic way. This periodic emission regime labeled as zone II resembles the microdripping regime observed in air, but with the difference that, in sub-zone *a*, no charged jet is issued from the meniscus tip during the whole process. In sub-zone *b*, the emission of charged jets from the tip of the elongated meniscus occurs in all the oscillations, Figure 4.4(a). Finally, when the voltage difference is sufficiently high, sub-zone *c* is reached, where the ligaments formed due to the elongation of the meniscus become considerable longer than before, and its detachment and break up results in several droplets of different diameters, although smaller than that of the inner tube's tip, Figure 4.4(b). For higher voltages the ligaments become even longer and doesn't completely detach from the meniscus, in

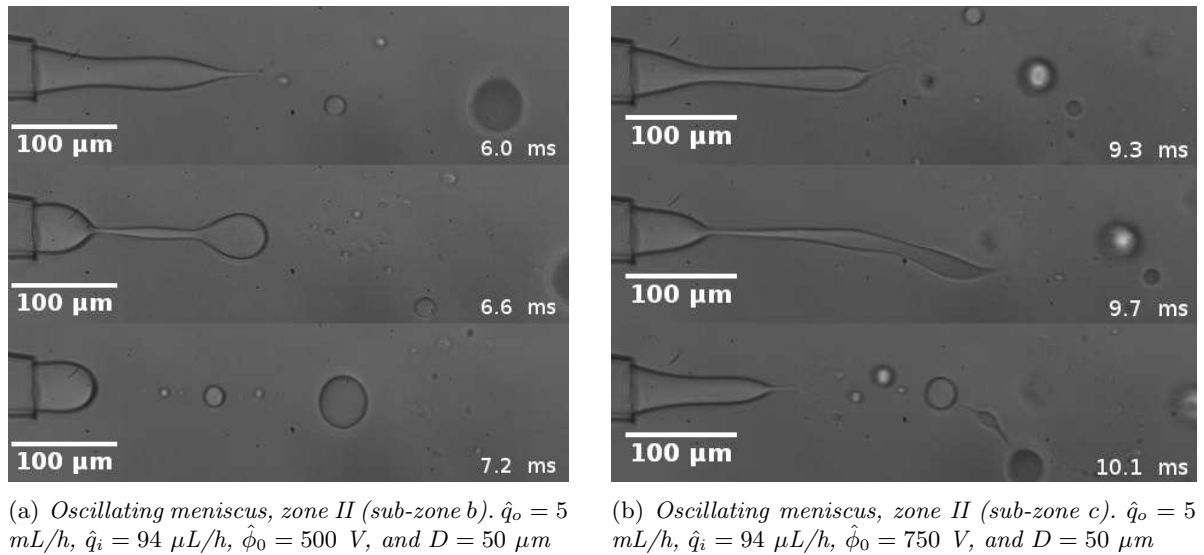


Figure 4.4: Emissions in electro-coflow: oscillating meniscus and transition to jetting.

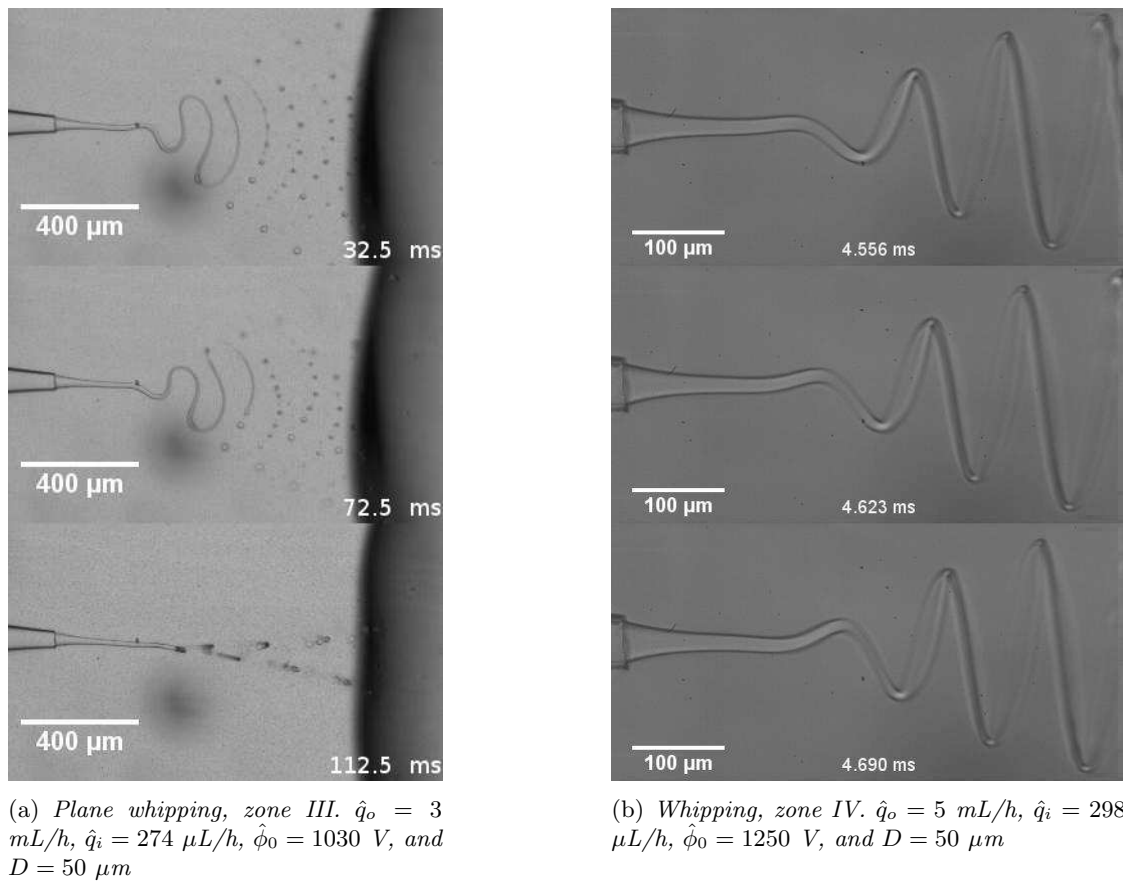


Figure 4.5: Emissions in electro-coflow: Emission of jets.

a clear transition to a jetting regime.

Jetting emissions occur for high enough voltages. In these emissions, from the tip of a static meniscus an electrified jet is issued. In zone IV three-dimensional whipping instabilities are dominant in the charged jets, which develop a helicoidal structure whose characteristic frequency is much slower than those observed in air thanks to the viscosity of the outer fluid, figure 4.5(b). It's to be noted the almost in-plane whipping observed in zone III, figure 4.5(a), in contrast with the three-dimensional structure of the jet in the whipping instability in zone IV. In zone

Liquid	μ [mPa s]	ρ [Kg m ⁻³]	K [S m ⁻¹]
Hexamethyldisiloxane 0.65 cSt	0.5 ⁽²⁾	764 ⁽¹⁾	-

Table 4.2: Properties of Sigma-Aldrich hexamethyldisiloxane 0.65 cSt at ⁽¹⁾20 °C, ⁽²⁾25 °C. Viscosity, μ , density, ρ , and conductivity, K .

III the jet tends to bend, but it remains confined on a plane that might rotate along the jet axis at very low frequencies. This in-plane whipping is, to our knowledge, the first time that has been observed. Cone-jet emissions, where the capillary/varicose instabilities are dominant and the jet breaks into droplets before it bends, have not been observed for the flow rates swept in the experiments and the liquids used.

4.3.2 Effect of the viscosity of the outer liquid.

The outer liquid has been changed to hexamethyldisiloxane from Sigma-aldrich (with a kinematic viscosity of 0.65 cSt, see table 4.2) to analyze the effect of the viscosity of the outer liquid on the emissions observed in electro-coflow. Attending to the phase diagram of the emissions for this outer liquid, Figure 4.6, the main observable change is that the zone III of plane whipping instabilities have changed to the zone labeled as V, where the charged jet emitted from the meniscus does not bend by the effect of the electric charges, not even breaks in droplets by Rayleigh-Plateau instabilities but it continues as a continuous straight jet until it impacts against the collector interface, figure 4.7.

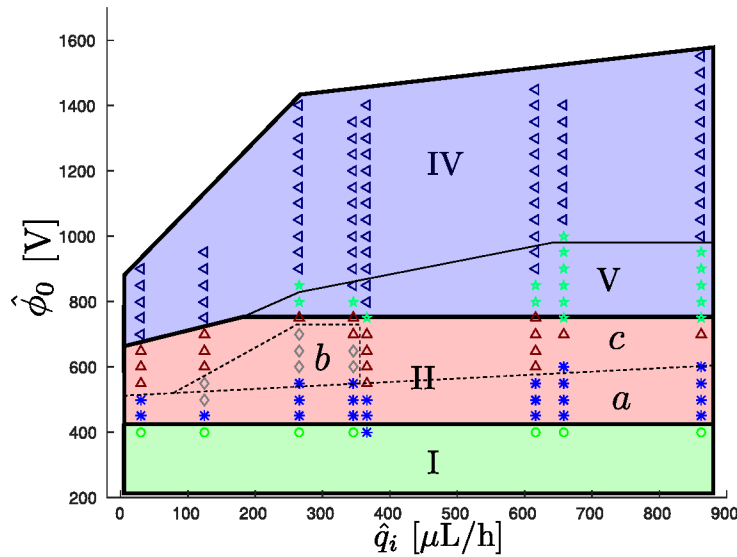


Figure 4.6: Phase diagram of the emissions in electro-coflow for different inner flow rates, \hat{q}_i and voltages applied to the inner liquid, $\hat{\phi}_0$. The outer liquid is hexamethyldisiloxane with a viscosity of 0.5×10^{-3} Pa s and the outer flow rate, \hat{q}_o , is 16 mL/h. Zone I for electrodropping, zone II for oscillating meniscus, and zones IV and V for jet emissions.

Another observation is that the maximum voltage applied to the inner liquid for which the collector remains stable is reduced as the viscosity of the outer liquid decreases. The whipping regime, zone IV, presents also changes when attention is paid to the structure of the jet. For a less viscous outer medium the whipping instabilities are not as regular as they were before, Figure 4.8. Now the structure of the jet is more irregular resembling the chaotic structure exhibited by electrified jets whipping in air.

These observations indicate that the viscosity of the outer medium is affecting the dynamics of the oscillating meniscus; and hence, viscous forces must be considered in the delicate balance

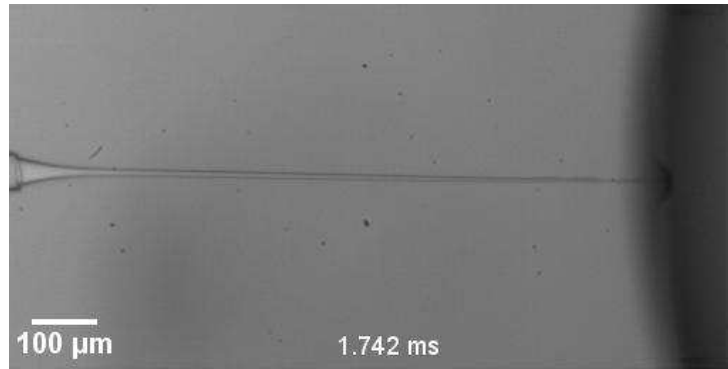


Figure 4.7: Jetting, zone V. $\hat{q}_o = 16$ mL/h, $\hat{q}_i = 346$ μ L/h, $\hat{\phi}_0 = 800$ V, and $D = 50$ μ m.

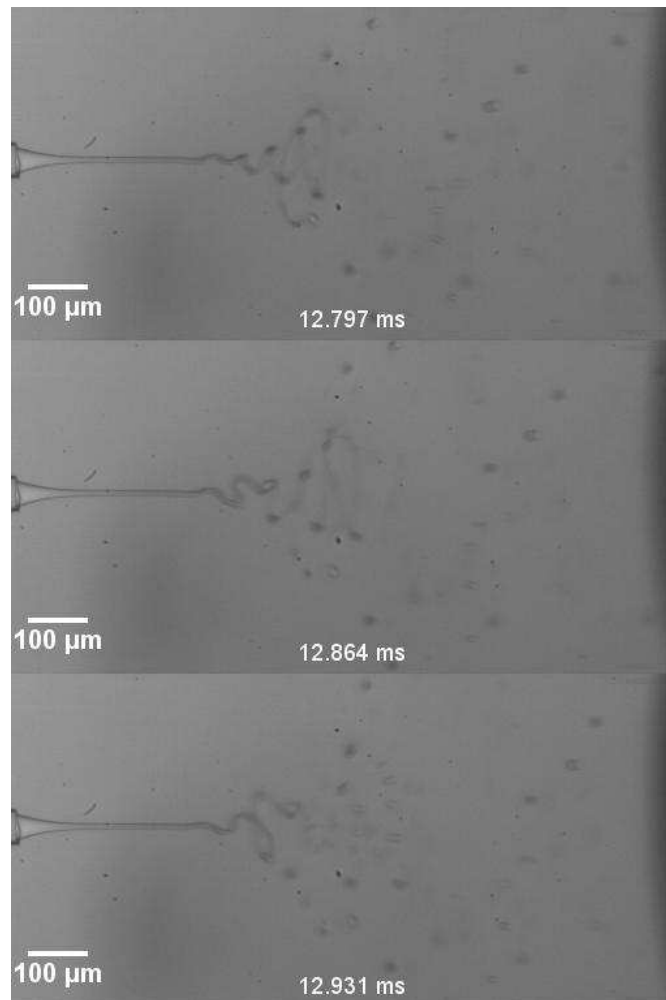


Figure 4.8: Whipping, zone IV. Viscosity of the outer liquid, 0.5×10^{-3} Pa s. $\hat{q}_o = 16$ mL/h, $\hat{q}_i = 346$ μ L/h, $\hat{\phi}_0 = 1000$ V, and $D = 50$ μ m.

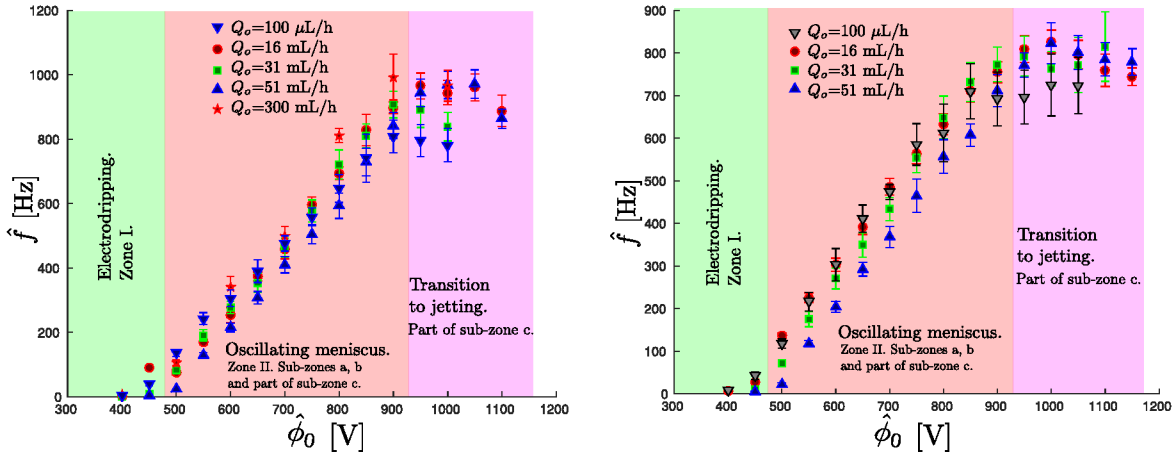
of forces that are acting on the meniscus.

4.3.3 Oscillatory regime in electro-coflow and comparison with microdripping regime in air

Once checked the viability of the liquid collector for discharging the emitted droplets and the outer flow for taking these droplets away, and once identified the parametrical range in \hat{q}_o , \hat{q}_i

and $\hat{\phi}_0$ where the regime with oscillating meniscus can be observed, zone II, the objective is to compare this regime in electro-coflow with the microdripping regime in air analyzed in Chapter 2.

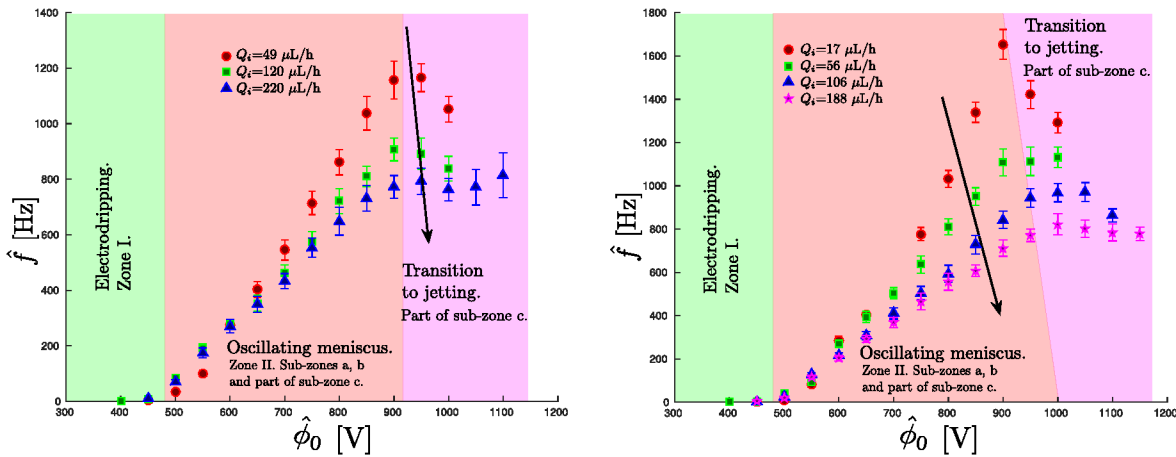
To do this, the frequency of the oscillation of the meniscus has been measured from the recorded videos. The gray level of the region occupied by the meniscus in the frames of the videos has been tracked over time. More precisely, the position of the centroid of the gray level of the pixels in this region changes with the motion of the meniscus at the same frequency that the meniscus oscillates. This makes possible to easily measure the oscillation frequency of the meniscus, \hat{f} , by means of a Fourier analysis of the centroid of gray level in the frames of each video.



(a) $\hat{q}_i = 111 \pm 28 \mu\text{L}/\text{h}$, and $\hat{q}_o = 100 \mu\text{L}/\text{h}$ (inverted triangles), $\hat{q}_o = 16 \text{ mL}/\text{h}$ (circles), $\hat{q}_o = 31 \text{ mL}/\text{h}$ (squares), $\hat{q}_o = 51 \text{ mL}/\text{h}$ (triangles) and $\hat{q}_o = 300 \text{ mL}/\text{h}$ (stars)

(b) $\hat{q}_i = 213 \pm 44 \mu\text{L}/\text{h}$, and $\hat{q}_o = 100 \mu\text{L}/\text{h}$ (inverted triangles), $\hat{q}_o = 16 \text{ mL}/\text{h}$ (circles), $\hat{q}_o = 31 \text{ mL}/\text{h}$ (squares) and $\hat{q}_o = 51 \text{ mL}/\text{h}$ (triangles)

Figure 4.9: Frequency of the meniscus oscillation, \hat{f} , in zone II, versus voltage, $\hat{\phi}_0$, for constant inner flow rate, \hat{q}_i . Different symbols are for different outer flow rates, \hat{q}_o , from $50 \mu\text{L}/\text{h}$ up to $300 \text{ mL}/\text{h}$. The viscosity of the outer liquid is $\mu_o = 9.3 \times 10^{-3} \text{ Pa s}$.



(a) $\hat{q}_o = 31 \text{ mL}/\text{h}$, and $\hat{q}_i = 49 \mu\text{L}/\text{h}$ (circles), $\hat{q}_i = 120 \mu\text{L}/\text{h}$ (squares) and $\hat{q}_i = 220 \mu\text{L}/\text{h}$ (triangles)

(b) $\hat{q}_o = 51 \pm 7 \text{ mL}/\text{h}$, and $\hat{q}_i = 17 \mu\text{L}/\text{h}$ (circles), $\hat{q}_i = 56 \mu\text{L}/\text{h}$ (squares), $\hat{q}_i = 106 \mu\text{L}/\text{h}$ (triangles) and $\hat{q}_i = 188 \mu\text{L}/\text{h}$ (stars)

Figure 4.10: Frequency of the meniscus oscillation, \hat{f} , in zone II, versus voltage, $\hat{\phi}_0$, for constant outer flow rate, \hat{q}_o . Different symbols are for different inner flow rates, \hat{q}_i , from $16 \mu\text{L}/\text{h}$ up to $220 \mu\text{L}/\text{h}$. The viscosity of the outer liquid is $\mu_o = 9.3 \times 10^{-3} \text{ Pa s}$.

Figures 4.9 and 4.10 are obtained when silicone oil of 10 cSt is used as outer liquid . In

Figures 4.9(a) and 4.9(b) the inner flow rate is maintained almost constant, and the outer flow rate is changed by three orders of magnitude, but the frequency of the oscillating meniscus is barely affected by the changes in the outer flow rate. The different curves remain approximately within the error bars of the measurements. The shape of the frequency versus voltage curves is quite indicative of the regime of each measurement. In zone II the frequency grows linearly with the voltage; for larger voltages (end of sub-zone *c*) the frequency remains almost constant or grows at a very lower rate with the voltage. Is in this part where the dripping regime is transitioning to a jetting regime. In the linear region, between 500 V and 900 V, there is a trend similar to that of the microdripping regime in air, where the frequency also increases linearly with the voltage.

In Figures 4.10(a) and 4.10(b) the outer flow rate is maintained constant and the inner flow rate is varied. When the inner flow rate is increased the oscillation frequency decreases, while the relation $\hat{f} - \hat{\phi}_0$ continues being relatively linear. Attending to changes in inner flow rate an voltage, the oscillation regimes in electro-coflow behave similarly than the microdripping regime in air, while changes in the outer flow rate do not produces appreciable changes in both frequency of the oscillation or emitted volume per oscillation.

4.3.3.1 Time scale of the meniscus oscillations

The main difference between the oscillating meniscus regimes observed in electro-coflow and the microdripping regime in air of Chapter 2 is the time scale of the meniscus oscillations. In the periodic microdripping regime in air the dynamics of the meniscus and the ligament formation process is determined by the action of capillary and electric forces. The electric forces are dominant in the meniscus tip, pulling the meniscus axially or at least maintaining the tip pinned, whilst the capillary forces are dominant in the meniscus zone close to the tube provoking the recession of this part of the meniscus. This distribution of stresses makes possible the formation and elongation of a ligament which ultimately detaches from the meniscus and develops a droplet. As stated in Chapter 2 the time needed to form and develop this ligament has an important effect on the period of the meniscus oscillations when high flow rates are being considered and hence large ligaments are formed. But despite this effect, as a first approximation, the period of the oscillations in microdripping in air is of the order of the capillary time. In electro-coflow, however, the period of the meniscus oscillations is of the order of 1×10^{-3} s, as shown in Figures 4.9 and 4.10, while the capillary time is of the order of $t_c = (\rho_i D^3 / \gamma)^{1/2} \sim 1 \times 10^{-5}$ s. In this case the tube's tip diameter is $D = 50 \mu m$, ρ_i is the density of the inner liquid, the ethylene-glycol, and γ is the interfacial tension between the inner and outer liquids, being the outer liquid silicone oil of 10 cSt. This difference with respect to the microdripping in air suggests that in the oscillation/emission process in liquid phase other stresses must play a role. When the viscosity of the outer medium is reduced from 9.3×10^{-3} Pa s to 5×10^{-4} Pa s, there is a significant increment of the oscillation frequency of the meniscus, which seems to imply that the new stresses that are important in the meniscus dynamics in electro-coflow are the viscous stresses of the outer and inner liquid.

Figure 4.11 shows a collage of images of different stages of the meniscus during the formation of the ligament for a representative case of the pulsating regimes in electro-coflow. In the image at the top the meniscus has a quasi-conical shape and a fine jet begins to be emitted from its tip. The ligament evolves very similarly to the way it does in the microdripping regime in air, developing a neck. And finally, in the image at the bottom, the pinch off occurs and the ligament detaches from the meniscus. The period of the meniscus oscillation is of the order of the ligament formation time, \hat{t}_s , which has a value of 1×10^{-3} s in the experiments of Figure 4.11. Estimates of the ligament formation time, and the effect that the viscosity of the inner and the outer liquid have on this time, are worked out in this section.

The ligament developed in the meniscus tip is a slender geometry that is characterized by a length, $\hat{\ell}_s$, and a width, \hat{d}_s , in the same way than in Chapter 2. During the ligament formation time, \hat{t}_s , the liquid flows in radial direction from the meniscus to the ligament a distance which

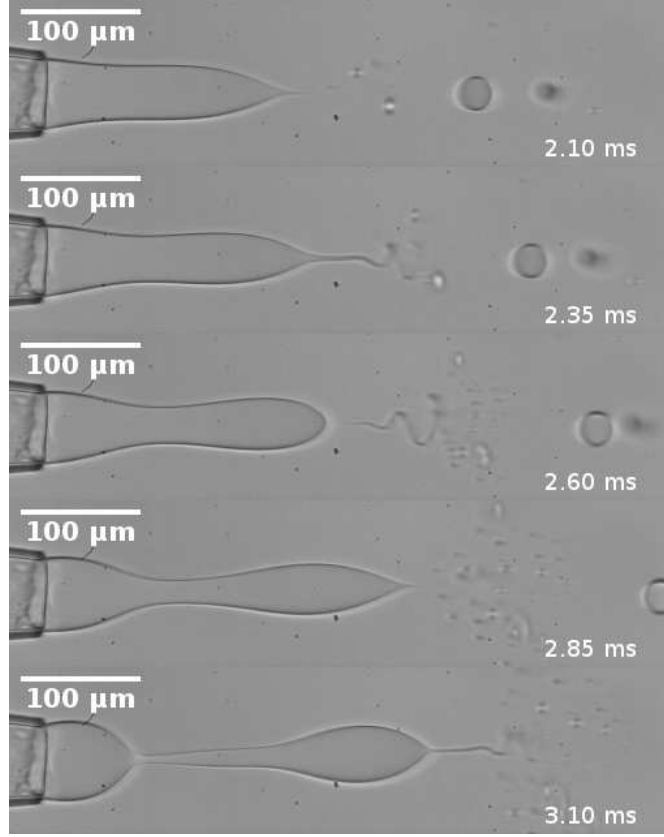


Figure 4.11: Ligament formation in oscillating meniscus regime, zone II, in electro-coflow. Viscosity of the outer liquid, 9.3×10^{-3} Pa s. $\hat{q}_o = 48$ mL/h, $\hat{q}_i = 188$ μ L/h, $\hat{\phi}_0 = 700$ V, and $D = 50$ μ m.

is of the order of \hat{d}_s at a radial velocity $\hat{v}_{rs} \sim \hat{d}_s/\hat{t}_s$, where the subindex s stands for ligament related magnitudes. This radial flow must fill up the rest of the ligament, so by the continuity equation, the axial velocity of the liquid in the ligament is $\hat{v}_{zs} \sim \hat{v}_{rs}\hat{\ell}_s/\hat{d}_s$, and hence $\hat{v}_{zs} \sim \hat{\ell}_s/\hat{t}_s$. Note that the ligament is a slender geometry and then $\hat{\ell}_s \gg \hat{d}_s$, which imply that $\hat{v}_{zs} \gg \hat{v}_{rs}$.

For the representative case of Figure 4.11, the Reynolds number of the inner and outer liquids are of the order of $\text{Re}_i = \rho_i \hat{\ell}_s \hat{d}_s / (\mu_i \hat{t}_s) \sim 1 \times 10^{-1}$ and $\text{Re}_o = \rho_o \hat{\ell}_s \hat{d}_s / (\mu_o \hat{t}_s) \sim 1 \times 10^{-1}$, respectively, where the subindexes i and o stand for properties of the inner and outer liquid; and the representative values of \hat{d}_s , $\hat{\ell}_s$, and \hat{t}_s measured in the recorded videos of the experiments are, respectively, 15 μ m, 200 μ m, and 1×10^{-3} s. These relatively low value of the Reynolds numbers indicate that the characteristic time of the oscillation of the meniscus is going to be some viscous time, instead of the capillary time as it occurs in air.

At the same time, the capillary stresses acting on the meniscus produce an overpressure $\Delta\hat{p}_\gamma \sim \gamma/\hat{d}_s$ in the region around the neck, which is the one that pushes the liquid in axial direction to form the ligament. This force per unit of ligament length is of the order of $\hat{F}_p \sim \hat{d}_s^2 \Delta\hat{p}_\gamma / \hat{\ell}_s$, and must be balanced by a viscous force since the Reynolds numbers are smaller than one.

The two candidates to balance \hat{F}_p are the viscous force per unit of ligament length due to the elongation of the liquid inside the ligament, which is of the order of $\hat{F}_{vi} \sim \hat{d}_s^2 \mu_i \hat{v}_{zs} / \hat{\ell}_s^2$, and the viscous force per unit of ligament length from the viscous shear stress due to the outer medium, which is of the order of $\hat{F}_{vo} \sim \mu_o \hat{v}_{zs}$. If we compare both viscous forces, we have that $\hat{F}_{vo}/\hat{F}_{vi} \sim \mu_o \hat{\ell}_s^2 / (\mu_i \hat{d}_s^2)$, where μ_i and μ_o are the viscosities of the inner and outer liquid, respectively. In the experiments performed both viscosities are of the same order, so $\hat{F}_{vo}/\hat{F}_{vi} \sim (\hat{\ell}_s/\hat{d}_s)^2 \gg 1$. So \hat{F}_{vo} must be the one that balances \hat{F}_p . From this balance the following expression for \hat{t}_s is obtained,

$$\hat{t}_s \sim \frac{\mu_o \hat{\ell}_s^2}{\gamma \hat{d}_s}. \quad (4.1)$$

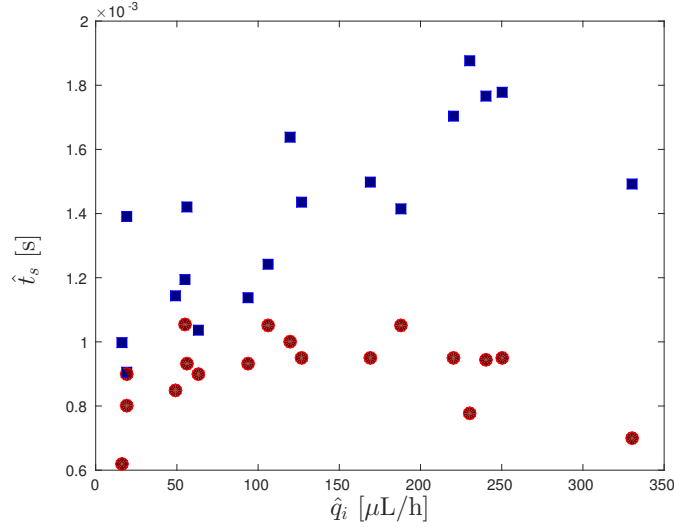


Figure 4.12: Ligament formation time, \hat{t}_s , versus inner flow rate, \hat{q}_i . Viscosity of the outer liquid, 9.3×10^{-3} Pa s. $\hat{\phi}_0 = 700$ V, and $D = 50$ μm . Circles for the values measured in the videos, squares for the values from Equation 4.1. The results corresponding to different outer flow rates are represented in this figure, due to the little effect that this flow has in oscillating regimes.

In Figure 4.12, the circles represent experimental values of \hat{t}_s versus the inner flow rate, whereas the squares represent the values of \hat{t}_s yield by Equation 4.1, calculated with the measured values of $\hat{\ell}_s$ and \hat{d}_s , versus \hat{t}_s . Although the values plotted in the figure have a high dispersion due to the uncertainties in the measurements of \hat{t}_s , $\hat{\ell}_s$, and \hat{d}_s , the order of magnitude of the values of \hat{t}_s are consistent with the experimentally measured period of the oscillations in electro-coflow oscillating regime.

4.3.3.2 Ligament characterization

As shown in Figure 4.4, in the parametric range for which periodic oscillating regimes are established, each of these oscillations have different stages, similar to those observed in the case of the microdripping regime in air: a first stage of elongation of the meniscus until fine jets are emitted from its tip, a second stage in which a ligament is developed, a third stage where the pinch off of the ligament occurs, and a final stage where a subtle recession of the meniscus take place.

Knowing that the ligament formation process is controlled by the viscous shear of the outer liquid, scalings of the ligament length, $\hat{\ell}_s$, and diameter, \hat{d}_s , can be obtained in electro-coflow with respect to the inner flow rate. In the experiments made on oscillating regime, zone II, the period of the oscillation, T , is of the order of the ligament formation time, t_s , approximately given by equation 4.1. Assuming that the mass flow issued in the form of spray from the tip of the ligament is small compared with the injected flow rate, mass conservation in the ligament provides $\hat{q}_i T \sim \hat{\ell}_s \hat{d}_s^2$, which combined with equation 4.1 yield

$$\hat{\ell}_s \sim \hat{q}_i^{1/5} T^{3/5}, \quad (4.2)$$

$$\hat{d}_s \sim \hat{q}_i^{2/5} T^{1/5}. \quad (4.3)$$

Figure 4.13 shows \hat{f} versus \hat{q}_i at constant voltage $\hat{\phi}_0$ for four different voltages. It seems that the frequency of the meniscus oscillation scales with a power close to $-1/3$ of \hat{q}_i for the range

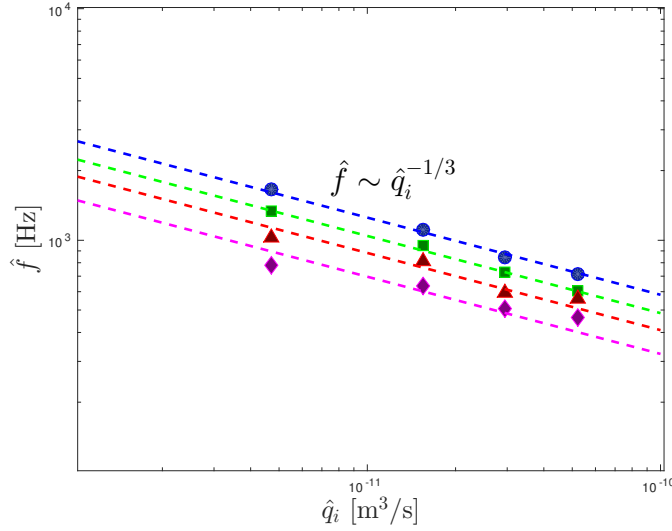
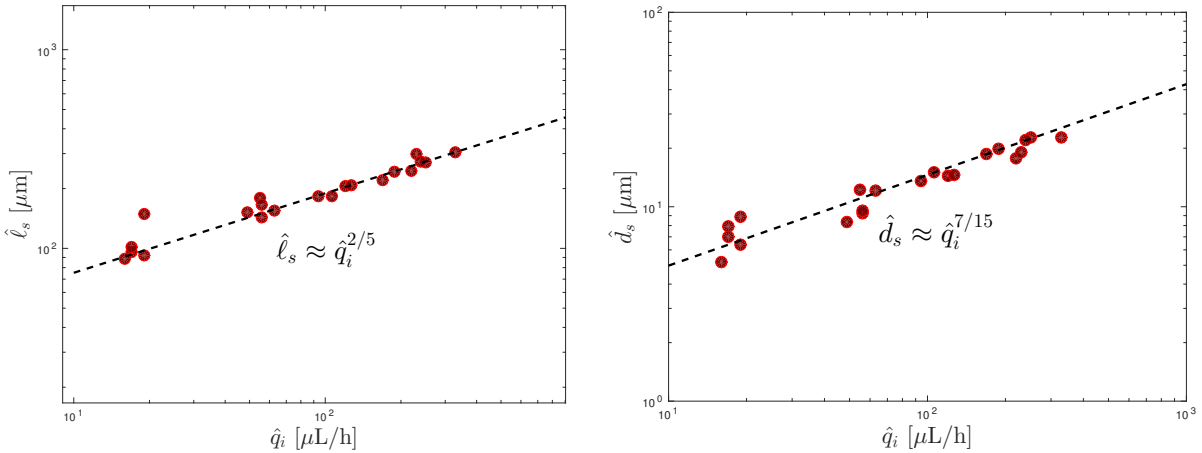


Figure 4.13: Frequency of the meniscus oscillation, \hat{f} , in zone II, versus inner flow rate, \hat{q}_i for an outer flow rate $\hat{q}_o = 51 \pm 7$ mL/h and outer viscosity $\mu_o = 9.3 \times 10^{-3}$ Pa s. Circles for $\hat{\phi}_0 = 900$ V, squares for $\hat{\phi}_0 = 850$ V, triangles for $\hat{\phi}_0 = 800$ V, and diamonds for $\hat{\phi}_0 = 750$ V. The dashed lines have slope $-1/3$.

of flow rates in the experiments. By introducing $T = 1/\hat{f} \sim \hat{q}_i^{1/3}$ in equations 4.2 and 4.3, the scalings $\hat{\ell}_s \sim \hat{q}_i^{2/5}$ and $\hat{d}_s \sim \hat{q}_i^{7/15}$ are obtained.

Figure 4.14 shows the measured values of \hat{d}_s and $\hat{\ell}_s$ versus the inner liquid flow rate, \hat{q}_i , in electro-coflow oscillating regimes for a voltage $\hat{\phi}_0 = 700$ V. Interestingly, despite of the dispersion of the measurements, which include those taken for different outer flow rates, the proposed scalings, represented by dashed lines, agree relatively well with the experiments. It is noteworthy that trends not too different from those obtained for microdripping in air are found for \hat{d}_s and $\hat{\ell}_s$, even though the dynamics in the zone II of electro-coflow are controlled by the viscosity of the outer fluid terms in our experiments.



(a) Length of the ligament $\hat{\ell}_s$ respect to the flow rate of the inner liquid \hat{q}_i . The dashed straight line has slope $2/5$.

(b) Width of the ligament \hat{d}_s respect to the flow rate of the inner liquid \hat{q}_i . The dashed straight line has slope $7/15$.

Figure 4.14: Length and width of the ligament immediately before detachment as a function of the inner flow rate. $\hat{\phi}_0 = 700$ V, and $D = 50$ μm . The results corresponding to different outer flow rates are represented in this figure, due to the little effect that this flow has in oscillating regimes.

4.4 Conclusions and future works

Following Gundabala et al. (2010), glass capillary microfluidic device has been manufactured with the purpose of generating emulsions of ethylene glycol in silicone oil using electro-coflowing techniques. A liquid collector has been used satisfactorily to discharge the droplets of the dispersed phase of the emulsion and the outer flow rate has been useful to drive the neutralized droplets away from the electrified meniscus of the inner liquid. Nevertheless, small pressure fluctuations in the systems controlling the outer and collector liquids flow rates make it difficult to maintain stable the liquid collector interface at a constant distance of 1 mm from the tip of the inner tube, so extreme care has to be taken to get steady state conditions. There is also a maximum voltage difference between the inner liquid and the liquid collector beyond which fine electrified jets are emitted from the collector severely affecting the dynamics of the meniscus of the inner liquid.

For a fixed couple of liquids (the inner and collector liquids are the same in our experiments), a phase diagram of the emissions in electro-coflow has been obtained by sweeping the governing parameters, the inner liquid flow rate, \hat{q}_i , the outer liquid flow rate, \hat{q}_o , and the voltage difference set between the inner and collector liquids, $\hat{\phi}_0$. The outer liquid flow rate does not have a pronounced effect on the phase diagrams, so those are given in the \hat{q}_i - $\hat{\phi}_0$ plane. Five different zones have been identified. Zone I stands for dripping. Zone II stands for oscillating meniscus, where in general a thin jet is issued from the tip of the ligament as it forms; although in some regions of zone II (sub-zone *a*) no jet is issued from the tip of the ligament. In another region of zone II, sub-zone *c*, the jet is continuously emitted from the ligament tip, and the ligament break up is multimodal, yielding droplets smaller than the tip diameter. This zone also covers the transition from dripping regimes to jetting regimes. In zone III, the first jetting zone, the highly charged jet experiences an in plane whipping: the wavy jet is always contained in an axial plane that may rotate at a slow frequency. This type of whipping, till our knowledge, has not been reported in the literature. In zone IV the electrified jet develops a three-dimensional whipping, forming an spiral whose diameter increases as the jet approaches the liquid collector. Finally, in zone V the jet becomes stable and remains straight until it reaches the liquid collector. For the liquid used, we have not seen a cone-jet structure that breaks up into droplets before the whipping sets in.

In the oscillation regime, zone II, the meniscus pinned to the tip of the inner tube drips periodically in a manner that resembles the microdripping regime in air characterized in Chapter 2. We find that in this oscillatory regime, before the transition to jetting occurs, the frequency of the oscillation \hat{f} increases lineally with the voltage $\hat{\phi}_0$, and decreases when the inner flow rate \hat{q}_i increases, similar to what we observed in the microdripping regime in air. This linear behavior is observed in all the sub-zones *a* and *b*, and nearly the entire sub-zone *c*, indicating that despite the differences observed in the emission, the whole zone II is the same oscillatory regime. The outer flow rate, \hat{q}_o , does not seem to have any effect on the frequency of the oscillation.

While the oscillation frequency for microdripping in air is of the order of the capillary frequency in the case of electro-coflow, however, the corresponding oscillation frequencies are two orders smaller than the capillary frequency. This suggests that other stresses must be involved in the process. Estimates of the importance of the viscous stresses due to the outer and the inner liquid are worked out, indicating that the viscous effect of the outer liquid on the dynamics of the ligament is responsible for slowing down the oscillation frequency. This leads to an estimate of the frequency in terms of the viscosity of the outer liquid, the interfacial tension and the length and diameter of the ligament that provides the correct order of magnitude of the oscillation frequency.

Approximate scaling laws have been worked out for the ligament length and width when the inner flow rate increases, assuming that the period of the meniscus oscillation is of the order of the formation time of the ligament, and observing that the frequency of the oscillation scales as

$$\hat{q}_i^{-1/3}.$$

As future works, new geometries need to be studied for the microfluidic device to generate the liquid collector interface, to make it more robust to fluctuations in the pressure or in the flow rate of the outer and collector liquids. The experimental work needs also to be extended to a wider range of flow rates and liquid properties (i.e. increase the viscosity ratio) to explore new emission regimes and production rates of droplets.

References

- Castro-Hernández, E. et al. 2009. Scaling the drop size in coflow experiments. *New J. Phys.* 11(7), 075021.
- Guerrero, J. et al. 2014. Whipping of electrified liquid jets. *Proc. Natl. Acad. Sci. U.S.A.* 111(38), 13763–13767.
- Gundabala, V. R., Vilanova, N., & Fernández-Nieves, A. 2010. Current-Voltage characteristic of electrospray processes in microfluidics. *Phys. Rev. Lett.* 105(October), 1–4.
- Gundabala, V. et al. 2013. “Method and Electro-Fluidic Device to produce emulsions and particle suspensions”. Patent US 2013/0277461 A1 (US).
- Riboux, G. et al. 2011. Whipping instability characterization of an electrified visco-capillary jet. *J. Fluid Mech.* 671, 226–253.
- Utada, A. S. et al. 2007. Dripping, Jetting, Drops, and Wetting: The Magic of Microfluidics. *MRS Bulletin* 32(09), 702–708.
- Utada, A. et al. 2005. Monodisperse double emulsions generated from a microcapillary device. *Science* 308(5721), 537–541.

Chapter 5

Resonance of electrified and non electrified pinned droplets

Contents

5.1	Introduction	61
5.2	Equations	62
5.3	Numerical approach	63
5.4	Experimental setup	65
5.5	Results	66
5.5.1	Vibrations of non-electrified pinned droplets	66
5.5.2	Vibrations of electrified pinned droplets	69
5.6	Conclusions	72
	References	72

5.1 Introduction

The stability and vibration of electrified and non-electrified pinned droplets has been thoroughly studied, both numerically and experimentally. In the related literature, it is customary the use of flat surfaces to support the droplet and then vibrate it to study its resonance. Nevertheless, in many practical cases droplets or meniscus are supported by, or are hanging from, more complex surfaces, like tube tips with different wall thickness, as in the case of electrosprays or the electric microdripping regime. The numerical scheme used to simulate the microdripping regime, see Appendices C and D, can also be used to perform nonlinear time-marching simulations of vibrating pinned droplets, that is, pendant or sessile drops anchored to the outer rim of a cylindrical rod, or tube, or to any other axisymmetric surface, to find their resonance frequencies, thus extending the works in the literature.

In the case of the resonance of electrified pinned droplets, a cylinder-plate configuration instead of a parallel plates configuration may be also more appropriate to generate the electric field around the droplet. This cylinder-plate configuration is broadly used in electrohydrodynamic atomization because the cylinder allows intensifying the electric field around the droplet for a given voltage difference.

The present chapter collects the results, obtained from numerical simulations and from experiments, of the first natural frequency of inviscid pinned droplets (higher natural frequencies are also obtained from the simulations, but the work is centered on the first natural frequency of the droplets). In this work, the droplets are anchored to the outer diameter of a rod or tube. For the case of electrified droplets, the electric field is created between the tube holding the droplet and a flat counter electrode.



For the computations, the liquid is considered a perfect conductor and inviscid, so that electrical relaxation effects are neglected and the flow is irrotational. Once the droplet is deformed, it is left to vibrate freely. Equilibrium static shapes are never reached due to the consideration of inviscid fluid, so the droplets remains oscillating indefinitely. The first natural frequencies of the vibrating droplet are obtained by performing the Fourier's Transform of the position of a point of the interface in time.

For the experiments, a solution of water and ethylene glycol is used to avoid evaporation/condensation of solvents. The droplets are hold in tubes with different wall thickness. The Ohnesorge number is of the order of 1×10^{-2} and its electrical relaxation time is $t_e \sim 1 \times 10^{-6} s$, so that viscous and electric effects in the liquid can be neglected.

5.2 Equations

Consider a droplet of radius R pinned to the tip of a tube of outer radius a and thickness e , as sketched in Figure 5.1 in dimensionless form. The liquid has a density ρ , a surface tension γ , is considered inviscid and its flow irrotational, so the Laplace's equation is solved inside the droplet for the velocity potential, $\hat{\phi}$, as in Chapter 3, with the difference that in the present case the injection velocity through the tube is zero, so the boundary condition for $\hat{\phi}$ at the tube walls and base, is $\nabla \hat{\phi} \cdot \mathbf{n} = 0$, with \mathbf{n} the normal to the boundary (see Figure 5.1(b)). The velocity potential at the droplet's interface is known in each time step, the interface being given by $f(\hat{z}, \hat{r}, \hat{t}) = 0$, with $f < 0$ inside the droplet. The kinematic and dynamic conditions must be satisfied at the interface (see Higuera et al. 2013b),

$$\partial_t \hat{f} + \hat{\mathbf{v}} \cdot \nabla \hat{f} = 0, \quad (5.1)$$

$$\partial_t \hat{\phi} + \frac{\hat{p}}{\rho} + \frac{1}{2} \nabla \hat{\phi} \cdot \nabla \hat{\phi} - g \hat{z} = \hat{c}(t), \quad (5.2)$$

where $\hat{\mathbf{v}} = \nabla \hat{\phi}$ is the liquid velocity and $\hat{p} = \gamma \hat{k}_u - 1/2 \epsilon_0 \hat{E}_n^2$ is the liquid pressure referred to the outer medium. \hat{k}_u is the local curvature, $1/2 \epsilon_0 \hat{E}_n^2$ the electric stresses and \hat{E}_n the normal electric field at the droplet's interface. The time dependent constant $\hat{c}(t)$ is selected at each time step to impose that $\hat{\phi}(\hat{r} = a, \hat{z} = 0) = 0$ as a reference, without limiting the generality of the foregoing. The local curvature is calculated as,

$$\hat{k}_u = \hat{k}_1 + \hat{k}_2, \quad \text{with} \quad \hat{k}_1 = -\frac{d\theta}{d\hat{s}}, \quad \text{and} \quad \hat{k}_2 = \frac{\cos(\theta)}{\hat{r}}, \quad (5.3)$$

where \hat{k}_1 is the in-plane curvature (i.e. in the $\hat{z} - \hat{r}$ plane), \hat{k}_2 is the azimuthal curvature, $\theta = \text{atan}(d\hat{r}/d\hat{z})$ is the slope angle of a tangent to a given point of the interface, and \hat{s} is the arc length, $d\hat{s}^2 = d\hat{z}^2 + d\hat{r}^2$. The singularity at the droplet's tip is solved considering that $\lim_{\hat{r} \rightarrow 0} \hat{k}_2 = \hat{k}_1$.

For the simulations of electrified droplets, the liquid is considered a perfect conductor and the outer medium a perfect dielectric gas or vacuum. The electric field inside the droplet is hence null and the outer electric field at the interface is normal to it, $\hat{\mathbf{E}} = \hat{E}_n \mathbf{n}$. Outside the droplet the electric field is obtained by solving the Laplace's equation for the electric potential $\nabla^2 \hat{\phi}_e = 0$ in the tube-plate configuration sketched in Figure 5.1(a). The boundary conditions are $\hat{\phi}_e = 0$ at the plate and far from the droplet, and $\hat{\phi}_e = \hat{\phi}_0$ at the tube and the droplet's interface.

The problem, considering the most general case of electrified droplets, is made dimensionless using the tube's outer radius, a , the capillary time, $t_c = (\rho a^3 / \gamma)^{1/2}$, the capillary velocity, $v_c = (\gamma / (\rho a))^{1/2}$, the electric field $E_c = \hat{\phi}_0 / a$ and the velocity potential $\phi_c = a v_c$. The resonance of the electrified pinned droplets depends then on four dimensionless parameters: The Bond number, B , the Electric Bond number, B_E ; and two geometric parameters: *i*) the aspect ratio R/a or the dimensionless volume, v_{ol} , and *ii*) the dimensionless thickness of the tube's wall, e/a .

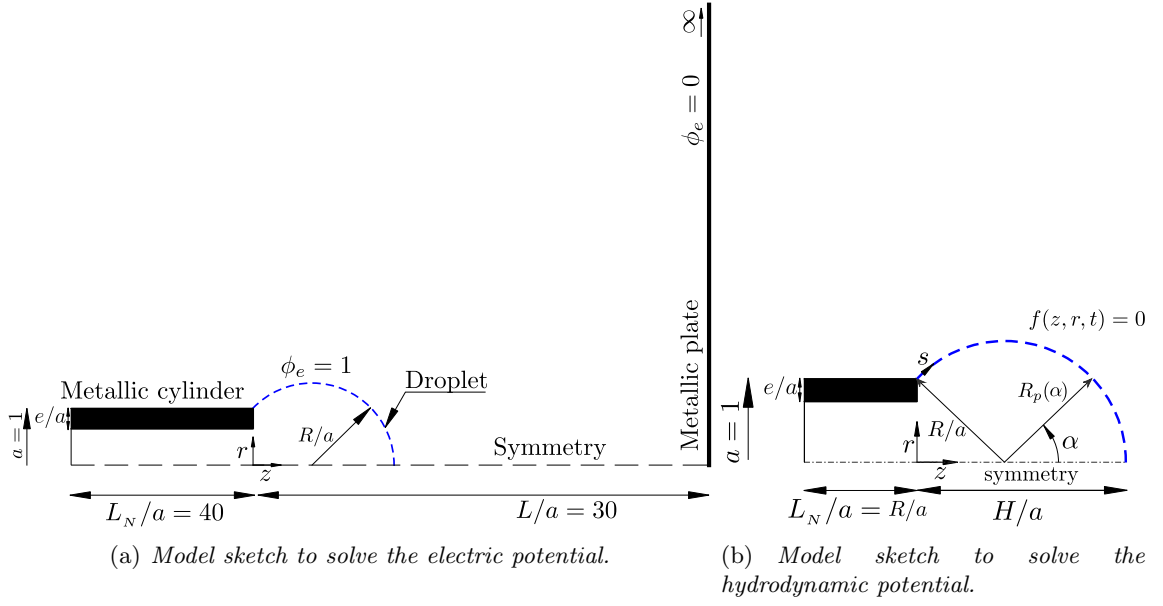


Figure 5.1: Definition Sketch.

$$B = \frac{\rho g a^2}{\gamma}, \quad B_E = \frac{\epsilon_0 E_c^2 a}{\gamma}, \quad v_{ol} = \hat{v}_{ol}/a^3, \quad e/a. \quad (5.4)$$

5.3 Numerical approach

Using Boundary Element Methods, BEM, as described in appendix C, the Laplace's equation for the velocity potential is transformed to the boundary integral equation shown in 5.5, which is solved exclusively on the boundary that encloses the liquid, which includes the droplet interface. For a known position of the interface, where r and z are respectively the dimensionless radial and axial position of a set of N points, equally distributed in arc length, on the interface, and for the known dimensionless velocity potential ϕ at those points, the dimensionless normal velocity to the interface, v_n , can be obtained from 5.5. The number of points in which is discretized the interface is selected as a function of the droplet volume, as $N = 101 + 4\text{round}(H/a)$, with $\text{round}()$ a function that rounds its argument to the nearest integer.

$$\phi(z_0, r_0) = -2 \int_{C_1} G(z, r, z_0, r_0) v_n(z, r) r dl + 2 \int_{C_1}^{PV} \phi(z, r) G_n(z, r, z_0, r_0) r dl, \quad (5.5)$$

where G is the appropriate Green function, see appendix C, $G_n = \nabla G \cdot \mathbf{n}$, C_1 is the boundary which encloses the domain where is solved the Laplace's equation, and PV stands for the Cauchy principal value of the integral.

For such interface, the tangential velocity $v_s = \partial_s \phi$ is obtained directly differentiating ϕ respect to the arc length s using central differences. And the axial and radial velocity are obtained as $v_z = v_s \cos(\theta) - v_n \sin(\theta)$ and $v_r = v_s \sin(\theta) + v_n \cos(\theta)$, respectively.

For the general case of electrified droplets simulations, the Laplace's equation for the electric field, $\nabla^2 \phi_e = 0$, is transformed, as in the case of the velocity potential, to the boundary integral equation 5.6 by means of BEM, see appendix C. Once solved, this equation provides the normal electric field $E_n = -\partial_n \phi_e$ at the interface.

$$\phi_e(z_0, r_0) = 2 \int_{C_2} G(z, r, z_0, r_0) E_n(z, r) r dl + 2 \int_{C_2}^{PV} \phi_e(z, r) G_n(z, r, z_0, r_0) r dl. \quad (5.6)$$

The boundaries C_2 and C_1 (see appendix C) depend, on the geometry used to generate the far electric field and to support the droplet, respectively. For the case of electrified pinned droplets, the droplet is connected to a dimensionless voltage $\phi_e=1$, and the reference voltage $\phi_e=0$ is in an infinite plane located at a dimensionless distance L/a from the droplet in axial direction.

Once the normal component of the electric field, E_n and velocity, v_n , are known on the interface at a given time, the time evolution of the interface is determined following the adaptive Runge-Kutta scheme of Appendix D. The points (z, r) of the interface at the next time step, together with the new velocity potential, are used to solve again the Laplace equations for v_n and E_n .

To test the model, the solutions yielded by the numerical scheme proposed above have been compared with results given in the literature. First of all, the vibration of charged and non-charged inviscid free droplets have been studied numerically under very small perturbations, and the natural frequencies obtained have been compared with the analytical expressions given by Rayleigh in both cases (Rayleigh 1879 and Rayleigh 1882). This comparison supports the validity of the numerical scheme used in this dissertation. The details have been included in Appendix C.

Then, axisymmetric numerical simulations of non-electrified pinned droplets have been performed in the geometry sketched in Figure 5.1(b) with and without the effect of gravity, $B \neq 0$, for different tube's wall thickness. These simulations have been compared with *i*) the analytical solution 5.7, which stands for the resonance of a droplet pinned to a circle (Bostwick et al. 2009, and see Appendix E), *ii*) simulations of droplets supported on a bowl (the geometry used for the solutions of Strani et al. 1984), and *iii*) experimental results of sessile droplets supported on a tube's tip. Also, non-electrified droplets pinned on a flat plate have been simulated to compare their first natural frequency for sub-hemispheric droplets.

Finally, axisymmetric numerical simulations of electrified pinned droplets have been performed in the geometry sketched in Figure 5.1, to check the effect of the Electric Bond number on their first natural frequency. For the sake of simplicity, in the case of these particular simulations, gravity has been neglected, $B = 0$, and tubes without wall thickness, $e/a = 0$, have been considered.

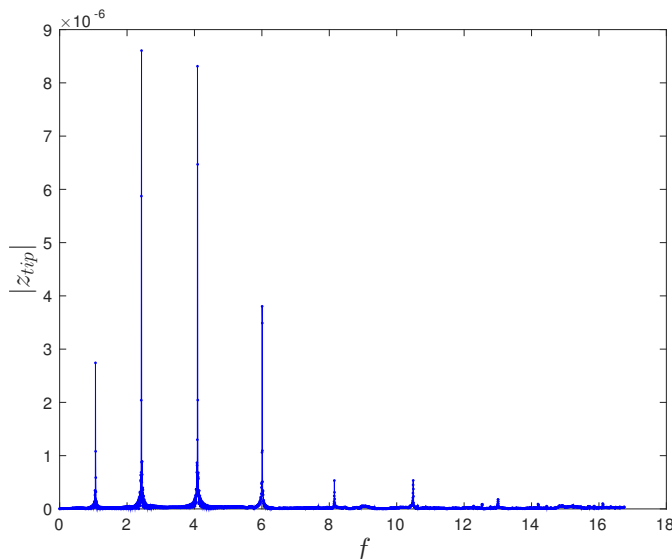


Figure 5.2: Peaks representing the natural frequencies obtained from the simulations after applying the Fourier transform to the evolution over time of the axial position of the droplet's tip, z_{tip} . This case is for a non-electrified sub-hemispheric droplet of volume $v_{ol} = 1.12$ supported on a tube of wall thickness $e/a = 0.3$

In all the cases, the simulation starts with an initial perturbed shape of the droplet (z_i, r_i) , and

an initial velocity potential ϕ_i on the droplet interface corresponding to a normal velocity $v_n = 0$. The stationary shape of a droplet of volume v_{ol} under the effect of an electric field generated in a tube-plate configuration, and pinned to the perimeter of the tube's tip of dimensionless radius $a = 1$ is used as initial position of the interface. The surface of the droplet is then perturbed in such a way that for each point (z, r) of the interface it holds that $z = C_z z_i (1 + \text{erand}(\alpha) \cos(\theta))$ and $r = C_r r_i (1 + \text{erand}(\alpha) \sin(\theta))$, compatible with the anchoring conditions to the tube, where α is an auxiliary angle used to generate the geometry and $\text{rand}(\alpha)$ is a function that gives a normally distributed random number between -1 and 1 for each α . The amplitude of the perturbation, ϵ , is generally a small number, $\epsilon = 0.001$, to study the effect of small perturbations, and when it is increased, nonlinear effects can be observed. The coefficients C_r and C_z are selected to force that the perturbed droplet have the same volume than the unperturbed one. The pinned droplet is left to evolve in time with the only restriction of the anchoring conditions to the tube, and after a dimensionless time between $t = 300$ and $t = 3000$, depending on the droplets volume, the Fourier transform of the axial position of the point $z_{tip} = (z(r = 0), r = 0)$ over time is used to obtain the different droplet natural frequencies (see the peaks in Figure 5.2 representing those frequencies).

5.4 Experimental setup

We have performed some experiments to study the resonance of non-electrified droplets. A volume of liquid is poured in a glass tube of outer diameter $D = 6.13$ mm, wall thickness $e = 1$ mm and a depth of two centimeters, as sketched in Figure 5.3(a). The liquid meniscus sticking out of the tube has a volume \hat{v}_{ol} varying from 9 nL up to 35 nL, and is anchored at the outer diameter of the tube, as shown in Figure 5.3(b). The liquid used is a 73 % w/w solution of ethylene glycol in distilled water. This concentration is in equilibrium with the moist in the air in the lab, at a temperature of 25 °C and a relative humidity of 48 %, so there is no evaporation nor condensation of water from or to the meniscus.

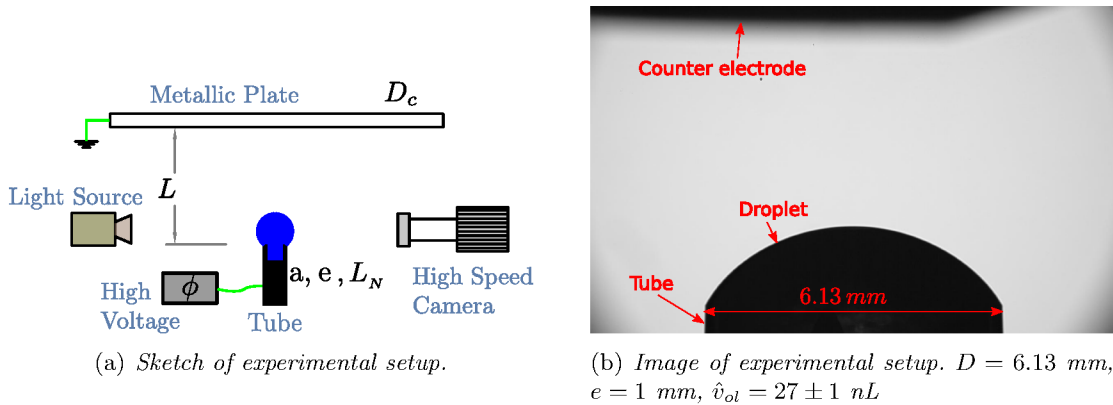
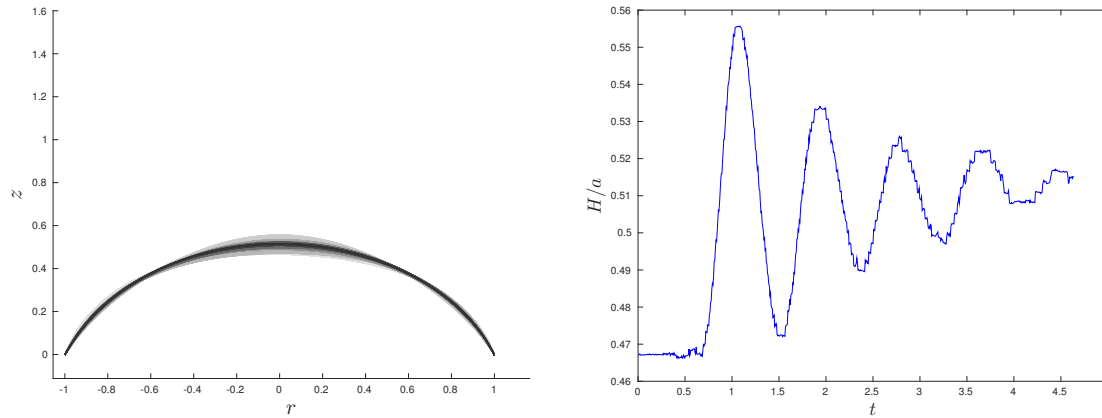


Figure 5.3: Experimental setup.

The liquid density is $\rho = 1088$ kg/m³, its surface tension of $\gamma = 49$ mN/m and its viscosity $\mu = 6.9$ mPas. All the properties have been measured at 25 °C. The density has been measured by means of a pycnometer, using distilled water as reference liquid. A du Noüy ring tensiometer has been used to measure the surface tension. A home made Ostwald viscosimeter was used to measure the viscosity.

Some sets of experiments have been done for different droplet volumes. In each experiment, the liquid inside the tube is initially connected to a high voltage with respect to the metallic plate located at 10 mm over the tube's tip, see Figure 5.3(a), so the meniscus original shape is deformed by the electric field created between the tube and the metallic plate. The voltage is then turned off suddenly, and the droplet starts to oscillate until it reaches its equilibrium



(a) superimposed contours of the droplet during its oscillation. Darker colors are used for the contours at the end of the droplet's oscillation.

(b) Variation of droplet height, H , with time.

Figure 5.4: Information obtained from high-speed recordings of vibrated droplets.

shape at rest. During its movement, a video is recorded using a high speed camera, and a set of images like that of figure 5.3(b) are obtained. These images are analyzed using different computer vision techniques to detect the contour of the droplets, as described in appendix B, so the evolution of the droplet shape and height with time can be characterized and measured. Figure 5.4(a) shows a set of droplet dimensionless contours obtained at different times since the electric field is turned off until the droplet becomes at rest. In this case the meniscus volume was $\hat{v}_{ol} = 27$ nL. Figure 5.4(b) shows the droplet dimensionless height since the electric field is turned off until the droplet becomes at rest. The analysis of this oscillation provides the first natural frequency of the droplet. Although an electric field is used to perturb the droplet surface, the resonance frequency obtained from $H/a(t)$ may be taken as that of a non-electrified droplet provided that (i) the voltage has been turned off in a time much shorter than the oscillation period, and (ii) that the electrical relaxation time of the liquid is also much smaller than the oscillation period. The charge relaxation time is $t_e = \epsilon\epsilon_0/K$, with ϵ the dielectric constant of the liquid, K its electrical conductivity, and ϵ_0 the vacuum permittivity. For the liquid considered, $t_e \sim 1 \times 10^{-6}$ s, which is effectively much shorter than the period of the oscillation of the droplets, which for the experimental cases is of the order of 1×10^{-2} s. This method of measuring the first natural frequency of droplets pinned to a tube's tip has turned out to be very effective compared to others, such as mechanically vibrating the meniscus. In particular, for the case of sub-hemispheric droplets, where its surface is barely excited by the action of a mechanical vibrator, excitation with the field has been essential to measure their natural frequencies.

5.5 Results

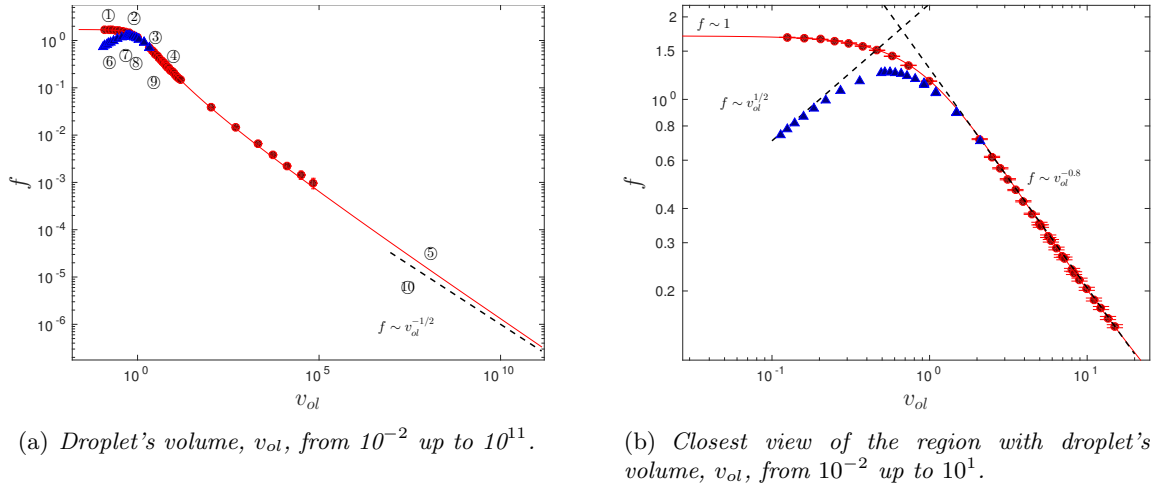
5.5.1 Vibrations of non-electrified pinned droplets

A droplet with the form of a spherical cap of dimensionless radius R/a and dimensionless volume v_{ol} is pinned to the rim of a circular flat surface, or tube's tip, of radius a , see Figure 5.1(b) in the simulations performed in this Chapter. Strani et al. 1984 found an analytical solution for the resonance of non-electrified inviscid droplets if instead of a flat surface or tube, a bowl is used to support the droplet. Bostwick et al. 2009 presented an extension of Strani's work, but in this case they studied the resonance of a droplet of radius R pinned to a circle. Strani and Bostwick do not obtain an analytical expression as a result of their work, because the pinned droplet that they are considering is vibrating immersed in an outer medium. But if no outer medium is considered instead, the analytical dimensionless natural frequencies, or eigenfrequency, $f = \hat{f}(\rho a^3/\gamma)^{1/2}$, for

inviscid droplets can be written into a compact expression as follows (see appendix E),

$$f = \frac{1}{2\pi} \left(\frac{R}{a} \right)^{-3/2} \sqrt{l(l-1)(l+2)}, \quad (5.7)$$

where l is a real number, which makes zero the Legendre's function of first kind $P_l(\cos(\alpha_0)) = 0$, with $\alpha_0 = \pi - \arcsin(a/R)$. Given α_0 , this equation has solution for an infinite number of l : $l_1 < l_2 < l_3 \dots$, which correspond with the resonance modes $n = 1, n = 2, n = 3, \dots$ of the droplet (if free droplets were considered). $l = l_2$ is the first value of l that corresponds to a vibration of the droplet where its volume remains constant, so it corresponds to the first natural frequency we are going to observe in the experiments and the simulations. This solution is shown in figure 5.5, where the dimensionless frequency versus the droplet dimensionless volume is represented by the solid red line.



(a) Droplet's volume, v_{ol} , from 10^{-2} up to 10^{11} .

(b) Closest view of the region with droplet's volume, v_{ol} , from 10^{-2} up to 10^1 .

Figure 5.5: First dimensionless eigenfrequency versus droplet dimensionless volume of pinned droplets. The solid red line represents analytical solution 5.7 (for l_2) and the dashed lines its trends in the regions where $v_{ol} \rightarrow 0$, $v_{ol} \sim 2$ (hemispherical droplets) and $v_{ol} \gg 1$. Circles indicates the simulations supporting the droplets on a bowl (Strani's geometry) whereas the triangles represents simulations of droplets supported on a flat surface. The frequency is made dimensionless with the capillary time associated to the anchoring radius a . The numbers in (a) corresponds to the cases shown in figure 7.

Several simulations have been performed using both the Strani's bowl and a flat surface to support the droplets. The results are shown in Figure 5.5. The cases for Strani's geometry are represented by the dots, whereas the triangles collect the results of droplets on flat surfaces. The analytical solution, Equation 5.7, is represented by the solid red line and, as expected, matches the simulations using the Strani's geometry. As stated by Strani et al. 1984, the frequency only seems to vary as a power of the volume if a small range of volumes is considered. For example, for a droplet radius between 1 and 3 times the radius of the solid support, $R/a = 1 - 3$, the first natural frequency goes as $f \sim v_{ol}^{-0.8}$. Nevertheless, when a wider range of volumes is swept, see figure 5.5(a), the relation frequency - volume is no longer potential. For very large droplets, $R/a \gg 1$, the first natural frequency of the pinned droplet tends to that of a free droplet, $f \sim v_{ol}^{-1/2}$. This last results was also stated by Strani et al.

Considering droplets on flat surfaces, the difference with Strani's results occurs for droplets with a volume lower than that of a hemisphere of radius $R/a = 1$, sub-hemispheric droplets, as can be seen in Figure 5.5(b). As v_{ol} increases over 1, the first natural frequency on a flat surface equals that provided by Strani's geometry. The difference between the oscillations in these two geometries can be seen in Figure 5.8 for five different values of v_{ol} , where the deformation of the interface, the red solid line, has been exaggerated to ease visualization. The cases 1 to 5

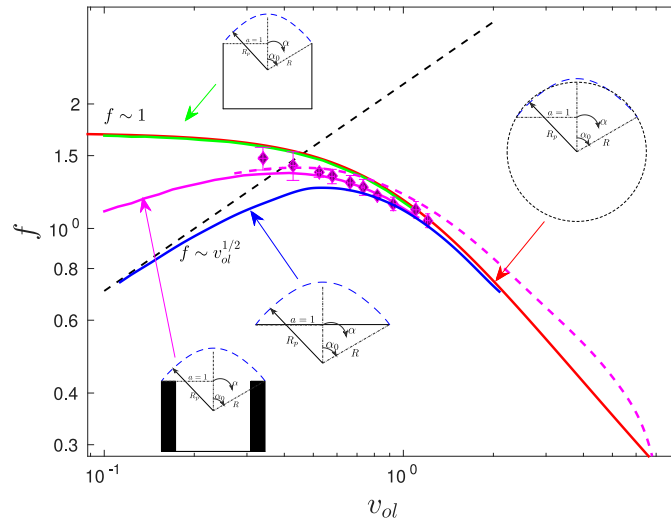


Figure 5.6: Evolution of the first dimensionless eigenfrequency versus the droplet dimensionless volume of pinned droplets. Solid red line for simulations of droplets supported on a bowl with $B = 0$, solid green line for simulations of droplets supported on the tip of a tube without thickness and with $B = 0$, solid blue line for simulations of droplets supported on a flat surface and with $B = 0$, solid magenta line for simulations of droplets supported on the tip of a tube with dimensionless thickness $e/a = 0.3$ and with $B = 0$, dashed magenta line for simulations of droplets supported on the tip of a tube with dimensionless thickness $e/a = 0.3$ and with $B = 2.04$, and diamonds for experiments of droplets supported on the tip of a tube with dimensionless thickness $e/a = 0.33$ and with $B = 2.04$.

correspond to the Strani's geometry, and cases 6 to 10 correspond to a spherical droplet supported on a flat surface. They are also represented by their corresponding numbers in Figure 5.5.

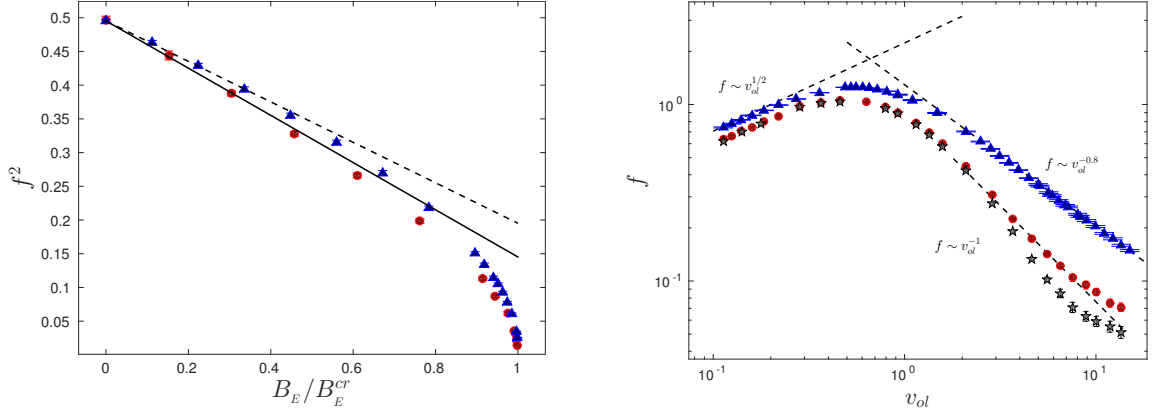
On the other hand, an analogy can be established between the vibration of pinned droplets supported on a flat surface and the stability of the free surface in a tank. Noblin et al. 2004 made use of this analogy to approximate the natural frequencies of pinned droplets. These authors considered a cylindrical tank of radius a filled up to an height h with the same inviscid liquid. The natural frequencies of the liquid's surface, made dimensionless with the capillary time and neglecting gravity, is $f = 1/(2\pi)\sqrt{k^3 \tanh(kh/a)}$, k being the zeros of the Modified Bessel Function of the first kind of order zero. In the analogy, the small volume droplets, $v_{ol} \rightarrow 0$, corresponds to a tank with a very low depth, $h \rightarrow 0$. In this limit the natural frequency for the vibration of the tank's surface scales as $f \sim v_{ol}^{1/2}$, in very good agreement with the simulations, see Figure 5.5(b).

If droplets are now supported on the tip of a tube of dimensionless radius $a = 1$ and depth R/a , that has no thickness, $e/a = 0$, the simulations, solid green line in Figure 5.6, indicates that, regardless of the droplet volume, the first eigenfrequency, f , is practically the same that in the case of droplets supported on a bowl, represented by the red solid line in Figure 5.6. In contrast, as already mentioned above, when droplets are supported on a flat surface, the natural frequency of sub-hemispheric droplets follows a completely different behavior as volume is reduced, solid blue line in Figure 5.6. This case represents the limit of a tube of radius a and thickness $e/a = 1$, so curves green and blue are the limiting cases for the behavior of the oscillation of droplets supported on a tube's tip of a given thickness. Effectively, if we perform simulations for the case of a tube with wall thickness of $e/a = 0.3$, solid magenta line in Figure 5.6, we observe that the result is between the curves green a blue, as expected. The diamonds in Figure 5.6 represent experiments of droplets supported on a glass tube of outer radius $a = 3.065$ mm and wall thickness of 1 mm, $e/a = 0.33$. We can see that the experimental data agree with the simulations, solid magenta line, even though $B = 2.04$ in the experiments. The dashed magenta line in Figure 5.6 shows the same simulations but taking $B = 2.04$. For hemispheric

and sub-hemispheric droplets, the influence of B is small, although it becomes significant as v_{ol} increases.

5.5.2 Vibrations of electrified pinned droplets

The droplets have been electrified, now, generating an electric field between a cylinder and an infinite plate. An hemispherical droplet of radius $R = a$ is supported on the flat base of the cylinder, of radius a , and the Electric Bond number has been increased from 0 to the critical value, B_E^{cr} , at which the droplet's surface becomes unstable and fine jets are emitted from it. The evolution of the first eigenfrequency of the simulated droplets in this case is compared with the case in which the electric field is created between two parallel plates and also with the analytical expression for charged free droplets of the same volume than the hemisphere placed at the cylinder's tip, Equation 1.2. The results are shown in Figure 5.7(a). The main difference between the cylinder-plate and parallel plates configurations is that the critic Electric Bond number is much higher in the case of the parallel plates, because the electric field intensifies more strongly at the cylinder's tip. Once normalized the Electric Bond number with its critic value, the evolution of f respect to B_E / B_E^{cr} are very close in both electrical configurations, circles an triangles in Figure 5.7(a).



(a) Square of the first eigenfrequency versus the ratio of the Electric Bond number to the critical Electric Bond number B_E / B_E^{cr} . Circles for the cylinder-plate configuration, triangles for the plate-plate configuration. The lines are for the expression $f^2 = f_{ne}^2 - C_g B_E / B_E^{cr}$, where the geometric factor corresponds to $C_g = 0.3$ (dashed line), and $C_g = 0.35$ (solid line). The volume of the droplet is the same in all the simulations and equal to the volume of a hemisphere of radius $R = a$.

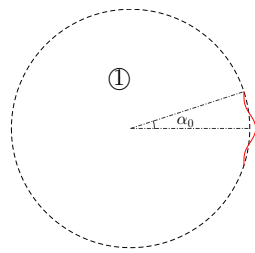
(b) First eigenfrequency versus droplet volume for $B_E = 0$ (triangles), $B_E = 5$ (circles) and $B_E = 5.3$ (stars) in cylinder-plate configuration. Dashed lines represent the tendencies for $v_{ol} \rightarrow 0$ and $v_{ol} \sim 2$

Figure 5.7: Dimensionless first eigenfrequency versus Electric Bond number and droplet's volume for the first vibration mode, $l = l_2$. For the case of droplets supported on a flat surface.

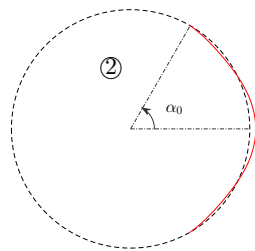
For $B_E / B_E^{cr} < 0.8$ the equilibrium shape of the droplet, before perturbing it, has a maximum radial deformation respect to a spherical shape lower than a 10%. For these quasi-spherical droplets the square of the first eigenfrequency varies linearly respect to the normalized Electric Bond number in a similar way than the charged free droplets do. That is $f^2 - f_{ne}^2 = -C_g B_E / B_E^{cr}$ (solid line in Figure 5.7(a)), where f_{ne} is the natural frequency of the same non electrified droplet and C_g a geometric factor. This expression is obtained analytically in Appendix E for a spherical droplet pinned to a circle and creating the electric field between the droplet and a concentric spherical counter electrode placed away from the droplet and perturbing the droplet's radius as $R_p(\alpha) = R/a + \epsilon^{i\omega t} P_l(\cos(\alpha))$, for small perturbations ($\epsilon \ll 1$). When $B_E / B_E^{cr} > 0.8$ the equilibrium shape of the droplets are clearly non spherical, are rather elongated in the axial

direction instead, and this produces a change on the tendency of the natural frequency, whose square is no longer linear with respect to the normalized Electric Bond number. In the limit of very elongated droplets, when $B_E \rightarrow B_E^{cr}$, the computed results seems to indicates that the square of the frequency scales as $f^2 \sim \sqrt{1 - B_E / B_E^{cr}}$, although the range of B_E swept are too small to be sure.

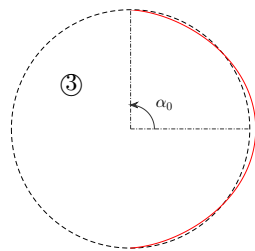
In Figure 5.7(b) the Electric Bond number is maintained constant, $B_E = 5$ and $B_E = 5.3$, in a cylinder-plate configuration and the droplet's volume has been increased. The first eigenfrequency, circles and stars, is compared with the simulations of non electrified droplet, triangles, in the same conditions. The same two tendencies than in the case of non electrified droplets have been found. For droplets with a volume lower than such of a hemisphere the frequency scales as $f \sim v_{ol}^{1/2}$ and for bigger droplets the frequency decreases initially as a power of the volume, with the difference that now there is a maximum droplet's volume beyond which no equilibrium shape exist.



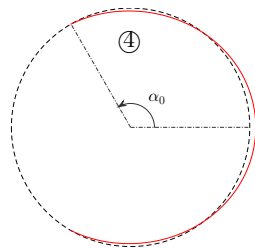
(a) $\alpha_0 = \pi/10$. Droplet supported on a bowl.



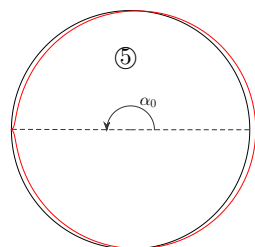
(c) $\alpha_0 = \pi/3$. Droplet supported on a bowl.



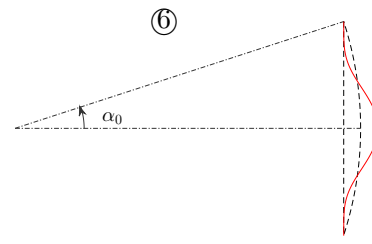
(e) $\alpha_0 = \pi/2$. Droplet supported on a bowl.



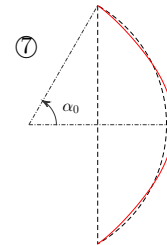
(g) $\alpha_0 = 2\pi/3$. Droplet supported on a bowl.



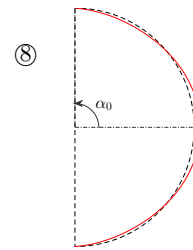
(i) $\alpha_0 = 0.999\pi$. Droplet supported on a bowl.



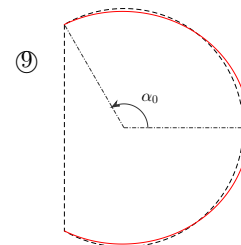
(b) $\alpha_0 = \pi/10$. Droplet supported on a flat surface.



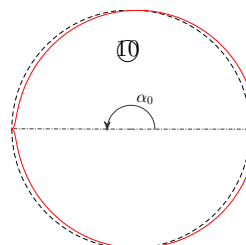
(d) $\alpha_0 = \pi/3$. Droplet supported on a flat surface.



(f) $\alpha_0 = \pi/2$. Droplet supported on a flat surface.



(h) $\alpha_0 = 2\pi/3$. Droplet supported on a flat surface.



(j) $\alpha_0 = 0.999\pi$. Droplet supported on a flat surface.

Figure 5.8: Deformed interface, solid line, for a droplet supported on a bowl (Strani's geometry), left, and a droplet supported on a flat surface, right. For the case $l = l_2$

5.6 Conclusions

In this chapter we have looked at the natural vibration of pinned droplets, with and without electrification. In particular, we have analyzed the effect of the shape of the solid supporting the droplets, as well as the effect of setting the electric field with electrodes in the plate-to-plate or in the cylinder-to-plate configuration. Spherical bowls, flat plates, and tubes with different wall thickness have been considered as solid supports. The inviscid, perfect conductor liquid model developed in Chapter 3 has been used to simulate the vibration of these droplets. Small perturbations have been considered in this work, although non-linear oscillations can also be determined. Some experiments have been carried out with non-electrified droplets.

Regarding the oscillation of uncharged droplets, it is found that, according to our model, pinned droplets with volumes larger than that of the hemisphere (super-hemispherical droplets) exhibit a first natural frequency that does not depend on the shape of the support. Our results matches with those of Strani et al. 1984, who considered droplets supported by a bowl of equal radius, and Bostwick et al. 2009, who considered droplets pinned by a circumference. However, for sub-hemispherical droplets, the geometry of the support strongly affects the natural frequency of the droplets and so its resonance. For flat supports, the first eigenfrequency tends to vary as $v_{ol}^{1/2}$ as $v_{ol} \rightarrow 0$, resembling the oscillation of a pool with a very small depth. However, if the support is a bowl the frequency remains constant. For tubes with different wall thickness the frequency evolves in between the previous two cases, letting it clear that the shape of the solid support affects the natural frequency of the droplets. Experiments with sub-hemispheric droplets seems to confirm the computed results.

To perform the oscillation experiments with sub-hemispheric droplets it has been essential to initially disturb them with an electric applied between the droplet support and a nearby electrode. After the electric field deforms the otherwise mechanical equilibrium shape, the voltage difference is turn to zero, so the droplet oscillates for several cycles. The optical analysis of the cycles allow obtaining the first natural frequency of the droplet. We where unable of mechanically excite sub-hemispheric droplets while within the small perturbation limit.

Regarding the oscillation of electrified droplets, the model developed in Chapter 3 allows to compare the effect of the electrode configuration. No experiments have been performed in this case. The analysis is restricted to hemispheric droplets. It is found that the range of B_E is much wider for the plate-to-plate than for the cylinder-to-plate configuration. In fact, the critical Electric Bond number B_E^{cr} at which no steady solution exists is much larger for the plate-to-plate than for the cylinder-plate configuration. Nevertheless, when the Electric Bond Number is normalized with the critical Electric Bond number, the first natural frequency made dimensionless with the capillary time for both configurations nearly coincide with each other. For $B_E / B_E^{cr} < 0.8$, where the droplet equilibrium shape is still close to an hemisphere, the eigenfrequency evolves approximately as that of the charged free droplet, $f^2 - f_{ne}^2 = -C_g B_E / B_E^{cr}$, where f_{ne} is the first natural frequency of the same non-electrified droplet and C_g is a geometrical factor. When $0.8 < B_E / B_E^{cr} < 1$ the equilibrium shape is rather elongated along the symmetry axis. The simulations seem to yield $f^2 \sim \sqrt{1 - B_E / B_E^{cr}}$.

References

- Bostwick, J. B. & Steen, P. H. 2009. Capillary oscillations of a constrained liquid drop. *Phys. Fluids* 21(3), 032108.
- Higuera, F. J. et al. 2013b. Pulsating emission of droplets from an electrified meniscus. *J. Aerosol Sci.* 66, 193–208.

- Noblin, X., Buguin, a., & Brochard-Wyart, F. 2004. Vibrated sessile drops: Transition between pinned and mobile contact line oscillations. *Eur. Phys. J. E* 14(4), 395–404.
- Rayleigh, L. 1882. XX. On the equilibrium of liquid conducting masses charged with electricity. *Philos. Mag.* 14(87), 184–186.
- Rayleigh, L. 1879. “On the capillary phenomena of jets”. *Proc. R. Soc. London.* Vol. 29. 196-199, pp. 71–97.
- Strani, M. & Sabetta, F. 1984. Free vibrations of a drop in partial contact with a solid support. *J. Fluid Mech.* 141, 233.

Chapter 6

Conclusions and future work

Contents

6.1	Conclusions	75
6.2	Future work	77
	References	78

6.1 Conclusions

This thesis deals with some aspects of the electro-hydrodynamic atomization (EHD) that are relevant to practical processes that require the generation of monodisperse droplets, in the micron size regime, in a host medium that may be a gas or vacuum or a liquid, but avoiding the use of micron sized nozzles, tubes or holes. In particular, this work focuses in regimes where a meniscus anchored to a tube oscillates periodically, and for the appropriate parametrical range, it emits a single droplet, substantially smaller than the diameter of the tube holding the oscillating meniscus, in each oscillation. Therefore, the body of the manuscript considers different problems where oscillating, electrified menisci are involved.

Chapter 2 collects the experimental analysis of the so-called oscillating axial mode II (Juraschek et al. 1998), also termed electric microdripping, in which the electrified meniscus of a low viscosity, highly conducting liquid, oscillates periodically in air, such that a single droplet noticeable smaller than the meniscus is emitted in each oscillation. As it oscillates, the meniscus stretches and develops a ligament that, eventually detaches from the meniscus, thus forming a droplet. Interestingly, the tip of the ligament develops a Taylor cone-electrospray for a non-negligible part of its life. Nevertheless the mass emitted by this electrospray is negligible compared to the mass of the droplet. The process is controlled by two dimensionless parameters, the Electric Bond Number B_E and the dimensionless liquid flow rate q . While $B_E \sim O(1)$, q may vary over several orders of magnitude, thus becoming the most important controlling parameter. The dimensionless oscillation frequency f , droplet diameter d_d , meniscus mean volume v_M and ligament dimensions, ℓ_s and d_s , have been characterized as q varies. The data are obtained from the analysis of digital images of the process taken with a high speed camera. It is found that $f \sim 1$ for very small flow rates and $f \sim q^{-1/2}$ as the flow rate increases, and also $f v_M \approx 0.32$ regardless of q . Regarding d_d , ℓ_s and d_s , some approximate scaling laws have been worked out. For small flow rates, the tiny ligament evolves linked to the oscillating meniscus and the pinch off time is controlled by capillary stresses leading to the scalings $d_d \sim q^{1/3}$, $\ell_s \sim q^{3/7}$ and $d_s \sim q^{2/7}$. For large flow rates, the dynamic of the ligament evolves on its own, with an interplay of the electric and the capillary stresses that, combined with the measured fact that the emitted droplets are charged to 20 % of its Rayleigh limit, suggest $d_d \sim q^{1/2}$, $\ell_s \sim q^{1/2}$ and $d_s \sim q^{1/2}$.

Chapter 3 is devoted to the modeling of the microdripping. An inviscid, perfectly conducting model liquid is considered. Neither the charged droplets nor any kind of charged aerosol that



might be emitted is considered in the model. The problem thus reduces to determining the velocity potential for the liquid and the electric potential outside of it. The Boundary Element Method (BEM) is used to transform the Laplace equation of both potentials into integrals on the boundaries. The numerical results describes qualitatively well the microdripping process. When compared with the experiments described in Chapter 2, the simulations reproduce well the meniscus oscillation frequency and mean volume. However, the details of the ligament dynamics are not fully captured by the model. A more detailed analysis of the tip of the simulated ligaments, which are forced to be rounded, appears to be the reason of the inability of the model to reproduce the details of the microdripping process, in particular the Taylor cone that forms at the tip of the ligaments observed in the experiments. The condition imposed at the tip causes spurious stresses at the ligament tip that leads to the spontaneous emissions of mass at very high frequencies from the tip of the simulated ligaments, which are not observed in the experiments. As a consequence, the simulations predict ligaments that are longer, thinner and have smaller volumes than the experimental ones, and also droplets smaller than those obtained experimentally. The disagreement increases as the flow rates are reduced. Nevertheless, the trend of the ligament length and diameter with the liquid flow rate are recovered by the simulations. On the other hand, the computed frequency combined with total mass conservation provides the correct droplets size.

Chapter 4 collects the experimental characterization of the so-called electro-coflow, a novel microfluidic implementation for simultaneously combining hydro and electro-hydrodynamic forces to form emulsions. The device comprises an inner tube 1, through which the liquid to be atomized flows, axially immersed in another tube 2 through which a dielectric liquid, immiscible with the previous one, flows. A third tube is immersed inside tube 2, facing opposite to tube 1, through which a conducting liquid, immiscible with the previous one, flows. The liquids flowing through tube 2 and 3 form a steady interface inside tube 2 that acts as an electric collector. The electric forces appear when a potential difference is set between liquids 1 and 3. Microfluidic devices made of glass have been built. In particular, the work focuses on conditions in which the electric forces are dominant. In this scenario, and for a given pair of liquids, the controlling parameters are the flow rates of liquids 1 and 2, \hat{q}_i and \hat{q}_o respectively, and the voltage difference between liquid 1 and 3, $\hat{\phi}_0$. It is found that \hat{q}_o has no effect. Seven different zones have been identified as function of \hat{q}_i and $\hat{\phi}_0$. Zone I stands for dripping. Zone II stands for oscillating menisci; a ligament forms at the tip of the meniscus, a thin jet is issued from the tip of the ligament as it forms (in most part of zone II), while in subsequent times there is no jet and the ligament breaks in a bimodal type break up. In the higher voltages of zone II the jet is continuously emitted from the ligament tip, and the ligament break up is multimodal, yielding droplets smaller than the tip diameter. This zone also covers the transition from dripping regimes to jetting regimes. In zone III, the first jetting zone, the highly charged jet experiences an in plane whipping: the wavy jet is always contained in an axial plane that may rotate at a slow frequency. This type of whipping, to our knowledge, has not been reported in the literature. In zone IV the electrified jet develops a three-dimensional whipping, forming an spiral whose diameter increases as the jet approaches the liquid collector. Finally, in zone V the jet becomes stable and remains straight until it reaches the liquid collector. For the liquid used, we have not seen a cone-jet structure that breaks up into droplets before the whipping sets in. The oscillating regimes, zone II, resembles the microdripping in air studied in Chapters 2 and 3. While the oscillation frequency for microdripping in air is of the order of the capillary frequency, in the case of electro-coflow, however, the corresponding oscillation frequencies are two orders smaller than the capillary frequency. Analysis of the viscous effect of the outer liquid on the dynamics of the ligament leads to an estimated oscillation frequency in terms of the viscosity of the outer liquid, the interfacial tension, and the length and diameter of the ligament that provides the correct order of magnitude of the oscillation frequency. Approximate scaling laws have been worked out for the ligament length and width when the inner flow rate increases, $\hat{l}_s \sim \hat{q}_i^{2/5}$ and $\hat{d}_s \sim \hat{q}_i^{7/15}$, assuming that the period of the meniscus oscillation is of the order of

the formation time of the ligament, and observing that the frequency of the oscillation scales as $\hat{q}_i^{-1/3}$.

Finally, in Chapter 5 the numerical scheme developed in Chapter 3 to simulate the microdripping regime has been used to compute the natural frequencies of electrified and non electrified pinned droplets, supported on different geometrical shapes. The dimensionless parameter controlling the process is the dimensionless droplet volume. For uncharged droplets, the geometry used to support the droplets has been found to affect its first eigenfrequency only for sub-hemispherical droplets. For sub-hemispherical droplets supported on a bowl the dimensionless frequency remains constant whereas for sub-hemispherical droplets on a flat plate the dimensionless frequency goes as the dimensionless drop volume to $1/2$ as the drop volume decreases. For super-hemispheric droplets the shape of the holder has almost no effect on the first natural frequency of the droplets. Experiments carried out with sub-hemispheric droplets confirm the numerical results. It is interesting to note that for doing these experiments the droplets were initially deformed with an electric field, a much more convenient way than mechanical excitation. For electrified droplets, hemispherical droplets in a plate-to-plate or cylinder-to-plate electrode configuration have been considered. The controlling parameters are the droplets dimensionless volume and the Electric Bond Number B_E , although we have fixed the dimensionless volume in the computations. When B_E is normalized with critical Electric Bond Number, B_E^{cr} , which is that at which the meniscus emits mass, the first dimensionless eigenfrequency for both electrode configuration are practically the same. For $B_E / B_E^{cr} < 0.8$ the frequency evolves as that of the charged free droplet, $f^2 - f_{ne}^2 = -C_g B_E / B_E^{cr}$, where f_{ne} is the first natural frequency of the same non-electrified droplet and C_g is a geometrical factor. When $0.8 < B_E / B_E^{cr} < 1$ the simulations seem to yield $f^2 \sim \sqrt{1 - B_E / B_E^{cr}}$

6.2 Future work

There are many possible ways to improve and to move forward the body of work described in this thesis. In regard of the electric microdripping in air or vacuum, two potential directions of advance are proposed. On one hand, the controlled generation of monodisperse, electrically charged, droplets in the micron size range might be very useful for 3D printing if the liquid were a molten material, such as molten alloys or metals, or if it were a material capable of solidifying very fast under a proper excitation, such as photopolymers. The interesting features are the high degree of monodispersity in size, control of the droplet size, and the possibility of easily driving the charged droplets to the desired spot by using external electric fields. This requires studying the solidification process and redesigning the set up accordingly to the new requirements.

On the other hand, it might be very interesting to try forming core-shell droplets by injecting two immiscible fluids such as the oscillating meniscus, composed of these two liquids, ejects a compound droplet. This requires studying the rapid dynamics of the compound meniscus or, perhaps, the dynamic of a meniscus covered by a thin layer of another liquid. This would open a new way to form liquid capsules in just one shot.

Any progress in understanding the electric microdripping must go through a better process modeling. Improvements of the proposed model needs to take into account the viscosity and the finite liquid conductivity to extend the study to liquids with other properties. Those, perhaps, might be more easily included in the 1-D lubrication approximation of the meniscus-ligament, as done by Hohman et al. 2001 for example. But most important, it is necessary to analyze the formation of the Taylor cone, and the electrospray it emits, on the evolution of the ligament. Perhaps, for highly conducting liquids, the scale disparity between the cone-jet and the rest of the geometrical lengths allows for an asymptotic treatment.

Further research also needs to be done to improve the robustness of the emulsion generation process in electro-coflow. The high sensitivity of the steady interface of the liquid collector to perturbations in the pressure of the outer and collector liquids makes it difficult to use this

technique for controlled production. A potential improvement, already tested in our lab, is to generate the interface of the liquid collector forcing it to coflow with the dielectric liquid instead of being counterflow. On the other hand, extension of the model to handle two low viscosity fluids or, perhaps, two very viscous (Stokes regime) might help to understand the electro-coflow process.

References

- Hohman, M. M. et al. 2001. Electrospinning and electrically forced jets. I. Stability theory. *Physics of fluids* 13(8), 2201–2220.
- Juraschek, R. & Röllgen, F. 1998. Pulsation phenomena during electrospray ionization. *Int. J. Mass Spectrom.* 177, 1–15.

Appendix A

Equipment description

Contents

A.1	Microdripping experiments in air	79
A.2	Coflowing experiments	80

A.1 Microdripping experiments in air

The equipment listed in Table A.1 has been used to perform the experiments of Chapter 2.

Instrument	Model	Manufacturer
Syringe pump	KDS-100-CE	Kd Scientific
High voltage power supply	Bertan 205B-10R	Spellman
High speed camera	Fastcam APX-RS	Photron
Tv screen	701N	Samsung
Data acquisition card	6024-E	National Instruments
Fiber optic illuminator	4000-1	Volpi
Ring tensiometer	Sigma 702	KSV
Conductimeter	TB84	ABB
Pycnometer 10 mL	PYC3-010-002	labbox
Laser Doppler velocimeter	miniLDV-G5-240	MSE Inc.

Table A.1: List of equipment used in experiments of Chapter 2.

The syringe pump has been used with plastic syringes, manufactured by Becton & Dickinson company, from 1 mL up to 5 mL of capacity, depending on the flow rate, in such a way that the stepping frequency of the pump doesn't affects the meniscus dynamics during the microdripping regime. A stainless steel tube connects the syringe to the tube where the meniscus is anchored through PEEK connectors, so that the system is rigid enough to have a quick answer to changes in the flow rate imposed by the pump.

The optical system for the high speed camera has been formed coupling different optics to obtain a spatial resolution ranging from 2.3 μm per pixel up to 12.5 μm per pixel. Each combination of optics used has been calibrated using a graduated microscope calibration slide. Both, x and y axis have been calibrated, and the distortion introduced by the lenses has been checked to be minimal.

A fiber optic illuminator has been used to illuminate the scene in the videos recorded with the high speed camera. The illuminator uses a halogen lamp of 90 W, and back-illuminates the tube's tip and the meniscus through a fiber optic cable, so that the lamp is far from the setup. The temperature in the meniscus has been measured with a thermocouple when the



illumination is connected. The temperature of the liquid at the meniscus is maintained reasonably constant during the experiments, at about 25°C, so that Marangoni effects are not considered. The illumination is enough to perform high speed recordings with exposition times as low as 2 μ s.

The current signal at the collector plate has been obtained using a data acquisition card by measuring the voltage drop at a shunt resistor of 1 M Ω . The current measured in the microdripping experiments is in the range of 100×10^{-9} A, so the effect of the current in the resistance of the shunt resistor is negligible and a standard resistor can be used. The ground of all the instruments and all the metallic parts of the setup not connected to high voltage were connected to the same ground to avoid ground loops.

Distilled water has been used as reference liquid to measure the density of the aqueous solution used in the experiments of Chapter 2 with the pycnometer at 25°C. Distilled water was also used as reference liquid in a homemade Ostwald viscometer, where the liquid, which viscosity wants to be measured, flows from an upper reservoir to a lower reservoir through a long tube when the levels of both reservoirs are maintained practically constant. The measured viscosity, μ_m , is then $\mu_m = K\rho_m t/M$, where ρ_m is the viscosity of the liquid, M is the mass of liquid which flows through the tube in a time t , and K is a constant which is determined using the reference liquid, $K = \mu_w M_w / (\rho_w t_w)$, when a mass M_w of distilled water, with viscosity μ_w and density ρ_w , flows through the same viscometer during a time t_w .

A.2 Coflowing experiments

The equipment listed in Table A.2 has been used to perform the experiments of Chapter 4. These experiments were performed during a stay at the Soft Condensed Matter Laboratory, in the School of Physics of the Georgia Institute of Technology, Georgia, USA.

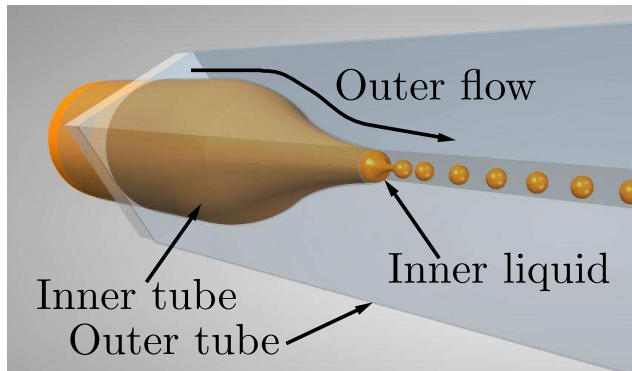
Instrument	Model	Manufacturer
High voltage power supply	Bertan 205B-10R	Spellman
High speed camera	Phantom v7.1	Vision Research
picoammeter	6485	Kethley
Pressure regulators	4ZM14	Speedaire
Inverted microscope	Axio-observer.A1	Carl Zeiss
Puller	P-97	Sutter Instruments
Microforge	MF-830	Narishige

Table A.2: List of equipment used in experiments of Chapter 4.

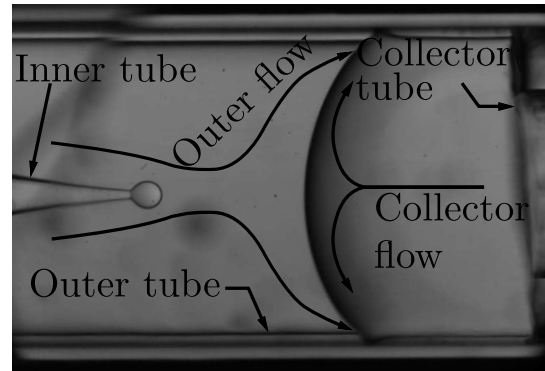
The puller indicated in the Table A.2 has been used to create micropipettes from borosilicate glass tubes of circular section with an outer diameter of 2 mm and an inner diameter of 1.16 mm. The stretched tip of the micropipettes has been cut and polished with the microforge equipment at a diameter of about 50 μ m. This tube, labeled as inner tube in Figure A.1, is introduced into a borosilicate glass tube, the outer tube, of square section and inner side of 2 mm as sketched in Figure A.1(a). Another glass tube, the collector tube, of circular section and outer diameter of 2 mm is introduced through the opposite side of the outer tube, to create the configuration shown in Figure A.1(b). Those tubes are glued with epoxy to a glass slide. PEEK tubes are also glued to the inlets of the inner, outer and collector tubes; and to the outlet of the outer tube. Hence, a microdevice with three inlets and an outlet is formed.

The glass microdevice is placed in an inverted microscope, where is connected a high speed camera to record high speed videos of the experiments. Objectives with zooms of 5x, 10x and 20x were used in the experiments.

Three pressurized reservoirs have been used to feed the inner, outer, and collector tubes. Pressure regulators are used to fix the pressure in each reservoir, which is maintained constant



(a) Sketch of the concentric configuration of the pulled inner tube and the square outer tube.



(b) Image of the inner, outer and collector tubes in the glass microdevice. The collector flow rate is settled to create a liquid collector at a distance of 1 mm from the tip of inner tube.

Figure A.1: Configuration of the inner, outer and collector tubes in the glass microdevices used in the experiments of Chapter 4.

during the experiments. The outer flow rate is then measured by weighting the amount of outer liquid, which is immiscible with the collector and inner liquids, used during each experiment.

The inner flow rate is determined by measuring in the videos the volume of a number of droplets emitted in electrodrizzling regime during a time t .

Appendix B

Image processing and measurement procedure of high speed videos

Contents

B.1	Contour detection in images	83
B.2	Subpixel detection algorithm	84
B.3	Region classification	85
B.4	Extraction of characteristics and measurements	88
	References	88

The videos recorded in Chapter 2 have been analyzed to extract information from them such as volume and trajectories of the emitted droplets and volume and curvature of the meniscus, among others. The oscillation frequency of the meniscus, although can also be measured from the videos, has been obtained with higher precision from the current signal measured at the collector plate with the data acquisition card.

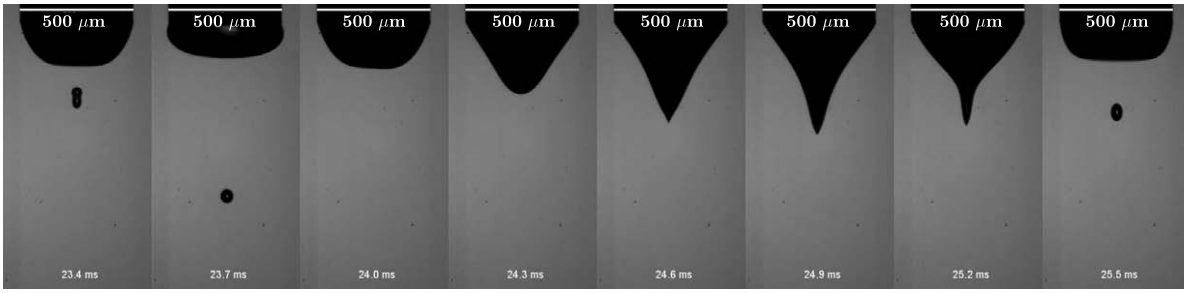
In the present Appendix, the procedure used to extract information from the high speed videos recorded in the experiments is described. A contour detection procedure is used to detect gradients in the gray level of the images. Once the contours of the black regions of the images are detected, these contours are smoothed with a subpixel detection algorithm. The different regions detected are then classified as meniscus or droplets using a classification algorithm based on invariant moments of image pixels. Once the droplets and meniscus are automatically recognized in the images, different characteristics are extracted from them, like shape, sizes, velocities or curvature.

B.1 Contour detection in images

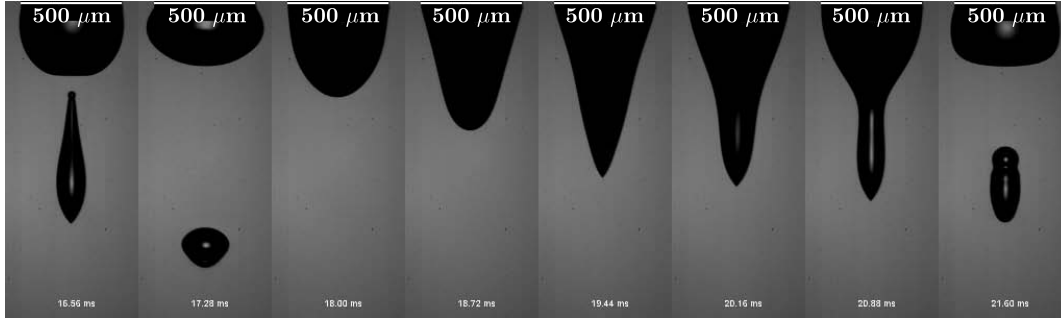
In the images of the recorded videos there is two clearly distinguishable regions with dark level of gray due to the back-illumination and the low exposition time used to record the videos, which corresponds to the droplets and the meniscus area in the images (see Figure B.1). Therefore, an algorithm which detects gradients in gray level, that is, transitions from dark to white gray levels, in the images is appropriate to detect the position of the contour of droplets and meniscus. Nevertheless, there is other transitions of gray level that are detected with this method which are not actual boundaries of the droplets or meniscus. Those non-interest contours are due, mainly, to a non-homogeneous background gray level or to the lens effects in rounded meniscus or stretched ligaments, and need to be identified and discarded. (see Figure B.1(b)).

The Canny algorithm (Canny 1986) has been used to perform the contour detection in the images. This algorithm looks for local maxima of the gradient of gray levels in the images. It uses an adaptive thresholding with hysteresis to detect these maximums. A 20 % and a 50 % of





(a) Tube's outer diameter $D = 500 \mu\text{m}$, flow rate $\hat{q} = 0.5 \text{ mL/h}$, voltage $\hat{\phi}_0 = 2.95 \text{ kV}$, and tube tip to collector distance $L = 9 \text{ mm}$.



(b) Tube's outer diameter $D = 500 \mu\text{m}$, flow rate $\hat{q} = 10 \text{ mL/h}$, voltage $\hat{\phi}_0 = 2.95 \text{ kV}$, and tube tip to collector distance $L = 9 \text{ mm}$.

Figure B.1: Recorded images of the meniscus and droplet emission during a period of the oscillation in electric microdripping regime for different flow rates.

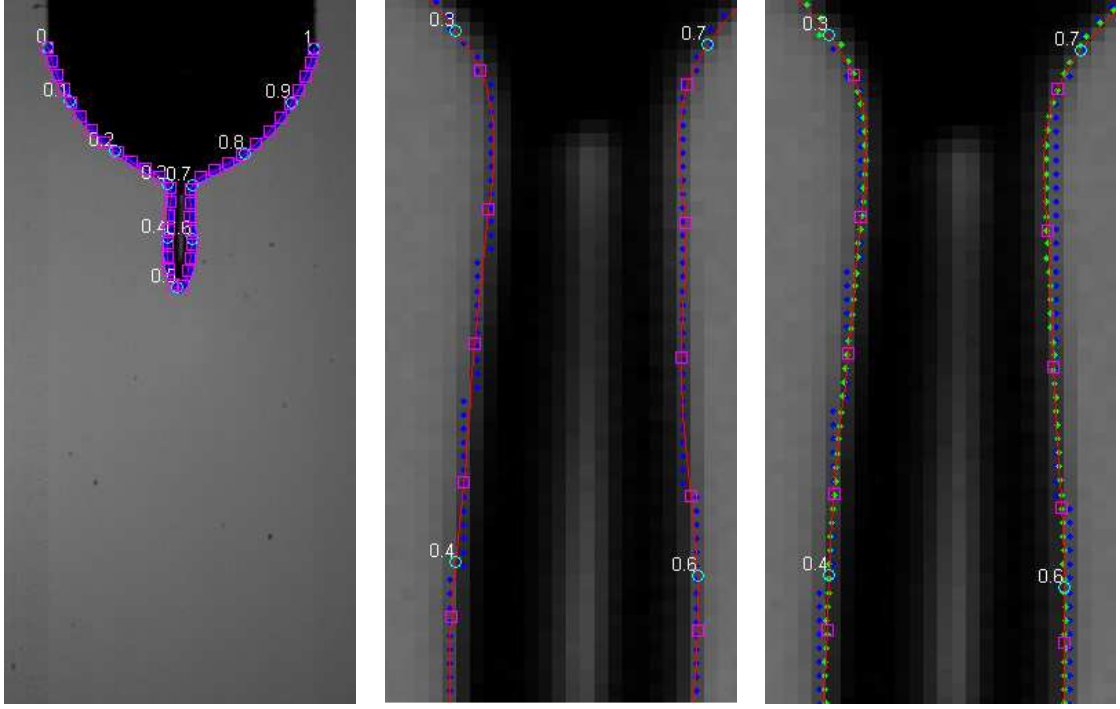
the maximum gradient value have been used, respectively, as minimum and maximum threshold values for the algorithm. The gradient of the gray level of the images is calculated by using the derivative of the Gaussian filter with a standard deviation of 1.6.

In Figure B.2 are shown the pixels detected by the Canny edge detector which correspond to the meniscus (dots). To smooth the boundary detected a cubic spline has been adjusted by least squares method using the points marked with squares as collocation points (see Figure B.2(b) for a closer detail at the ligament). This algorithm has produced a unique and precise detection of the meniscus and droplets contours in all the videos recorded in the experiments, with little adjustments needed due to changes in the illumination condition.

Similar detection techniques have been satisfactorily used in the literature to detect liquid interfaces (see Acero et al. 2013 and Song et al. 1996) such as pendant or sessile drop contours.

B.2 Subpixel detection algorithm

The precision of the edge detection performed by the Canny algorithm is determined, at first, by the pixel size in the images. Nevertheless, a subpixel analysis of the images has been done to correct the position of the edges detected by the Canny detector, giving thus a position of the meniscus and droplets contours with a resolution higher than such of the image. This subpixel analysis consists on adjusting a sigmoid function, equation B.1, to the gray level of the image pixels, $g(x)$, in the direction of the gradient, x , through the transition from a dark level, g_1 , inside a droplet of meniscus to a white level, g_2 , at the other side of the contour, as sketched in Figure B.3(a). The adjustment gives as result the parameters g_1 , g_2 , W and x_0 , where x_0 is the actual position of the edge at a subpixel level. In Figure B.3(b) the gray level at the position of the pixels in the direction of the gradient around the edge are represented by circles. The function B.1 is fitted to those points, and a more precise position of the contour, between pixels, is determined, marked with an asterisk in the figure.



(a) Meniscus contour detected by the Canny algorithm, dots, with a spline adjusted by least squares method, line, using as collocation points those marked with square symbols.

(b) Closer view of the contour detection of the ligament neck. Contour detected by the Canny algorithm, dots. Adjusted spline by least squares method, line. Collocation points for the spline adjustment, squares.

(c) Subpixel correction of the contour detection at the neck of the ligament, green dots. And spline adjusted to the corrected points, line.

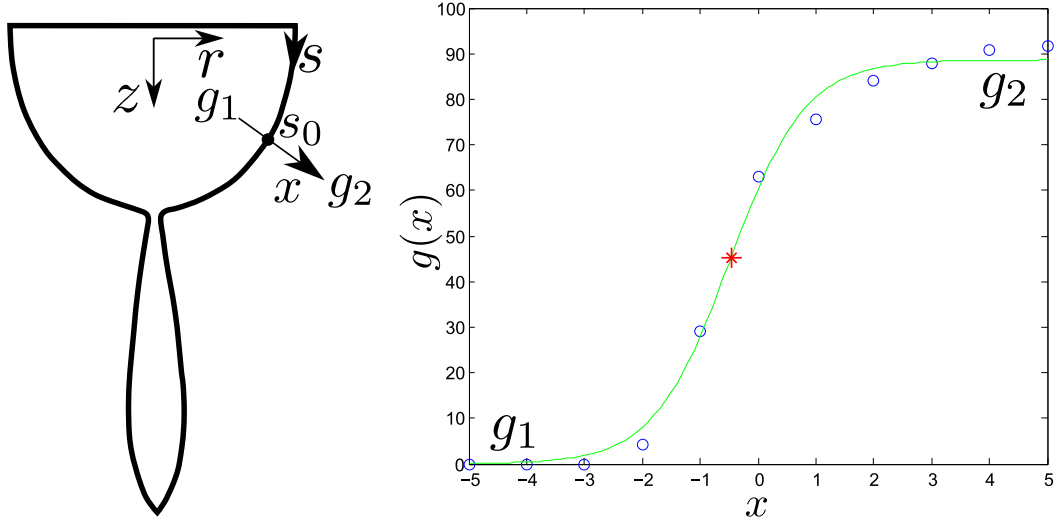
Figure B.2: Contour detection. Tube's outer diameter $D = 500 \mu\text{m}$, flow rate $\hat{q} = 1.0 \text{ mL/h}$, voltage $\hat{\phi}_0 = 2.95 \text{ kV}$, and tube tip to collector distance $L = 9 \text{ mm}$. As a reference, the normalized arc length, s , with values from 0 to 1, is represented (circles) in the images.

A cubic spline adjusted by least squares method to the edges detected by the Canny algorithm and corrected with the subpixel analysis allows a precise and smooth detection of the contours of droplets and meniscus, as shown in Figure B.2(c), where the edge detected by the Canny algorithm is represented by blue dots, the subpixel correction gives the green dots, and the solid line is the spline adjustment.

$$\epsilon(x) = \frac{g(x) - g_2}{g_1 - g_2} = \frac{1}{1 + e^{(x-x_0)/W}}. \quad (\text{B.1})$$

B.3 Region classification

Before obtaining the volume, velocity and sizes of droplets and meniscus from the images in the recorded videos, it is necessary to distinguish which of those detected contours corresponds to a droplet, to a meniscus, or if they are not actual boundaries of droplets or meniscus but non-interest contours. This classification is done using the invariant moments of the different groups of pixels detected, known as regions, which corresponds with edges in the images. These invariant moments, known as Hu moments (Hu 1962), are invariant to the scale, position, rotation and reflexion of the region considered, so basically they can be used to detect shapes. Those moments consist in a vector of seven numbers, from hu_1 to hu_7 in equations B.2 to B.8, that are used to classify each detected region.



(a) Sketch of the meniscus with x indicating the direction of the gradient of gray level in the images from gray level g_1 , dark, to gray level g_2 , clear.

(b) Non-linear adjustment of a sigmoid function, $\epsilon(x)$, (solid line) to the gray level, $g(x)$, of the pixels in the images (circles) through the direction of the gradient, x . g_1 and g_2 are, respectively, the gray level inside and outside the droplets or meniscus. The point $(x_0, \epsilon(x_0))$ of the sigmoid function, marked with an asterisk, indicates the position of the contour at a subpixel level.

Figure B.3: Detection subpixel.

$$hu_1 = u_{20} + u_{02}, \quad (\text{B.2})$$

$$hu_2 = (u_{20} - u_{02})^2 + 4u_{11}^2, \quad (\text{B.3})$$

$$hu_3 = (u_{30} - 3u_{12})^2 + (3u_{21} - u_{03})^2, \quad (\text{B.4})$$

$$hu_4 = (u_{30} + u_{12})^2 + (u_{21} + u_{03})^2, \quad (\text{B.5})$$

$$hu_5 = (u_{30} - 3u_{12})(u_{30} + u_{12})((u_{30} + u_{12})^2 - 3(u_{21} + u_{03})^2) + (3u_{21} - u_{03})(u_{21} + u_{03})(3(u_{30} + u_{12})^2 - (u_{21} + u_{03})^2), \quad (\text{B.6})$$

$$hu_6 = (u_{20} - u_{02})((u_{30} + u_{12})^2 - (u_{21} - u_{03})^2 + 4u_{11}(u_{30} + u_{12})(u_{21} + u_{03})), \quad (\text{B.7})$$

$$hu_7 = (3u_{21} - u_{03})(u_{30} + u_{12})((u_{30} + u_{12})^2 - 3(u_{30} + u_{12})^2) + (u_{30} - 3u_{12})(u_{21} + u_{03})(3(u_{30} + u_{12})^2 - (u_{21} + u_{03})^2), \quad (\text{B.8})$$

where $u_{ij} = \mu_{ij}/\mu_{00}^{1+(i+j)/2}$ are the normalized form of the central moments μ_{ij} of the region form by the pixels of the contour detected. With $\mu_{ij} = \sum_{y=1}^N \sum_{x=1}^N (x - \mu_x)^i (y - \mu_y)^j$, being N and (μ_x, μ_y) the number of pixels and the centroid of the region, respectively, and (x, y) the coordinates in the image of each pixel.

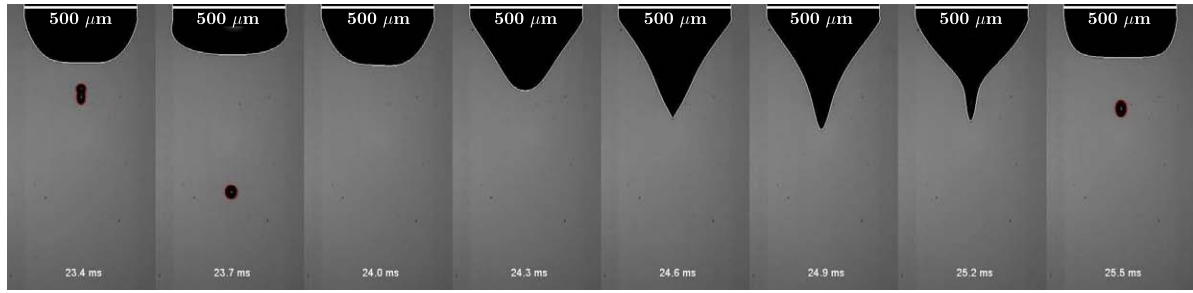
The space formed by the seven Hu moments have been analyzed to search zones in that space corresponding to meniscus or droplets. As a result of this analysis a region is classified as a meniscus if $hu_3 > \delta$, where δ is a number between 100 and 400, depending on the flow rate. And a region is classified as a droplet if the criteria B.9 to B.11 are fulfilled. The rest of the regions are classified as regions non-interest.

$$hu_1 > |(hu_2, hu_3, hu_4, hu_5, hu_6, hu_7)| \quad \text{or} \quad \max(hu_1, hu_2, hu_3) > |(hu_4, hu_5, hu_6, hu_7)|, \quad (\text{B.9})$$

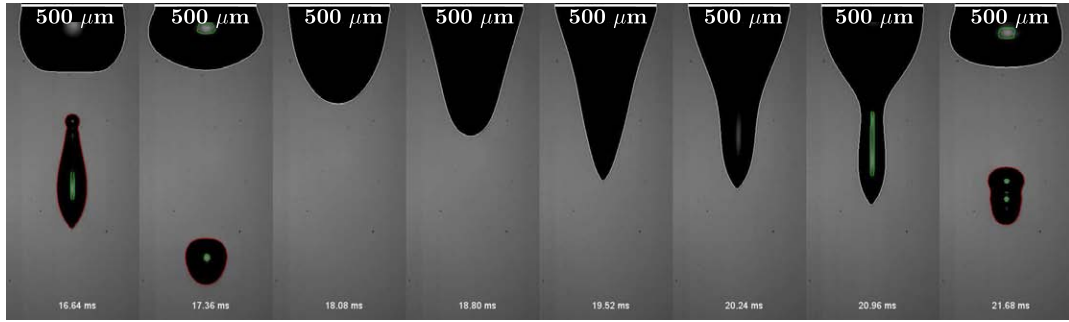
$$\min(hu_1, hu_2, hu_3, hu_4, hu_5, hu_6, hu_7) > 2, \quad (\text{B.10})$$

$$hu_3 < \delta. \quad (\text{B.11})$$

In Figure B.4 can be observed how the different regions detected have been classified in the recorded videos. The regions detected as meniscus or droplets are marked with a white or red line,



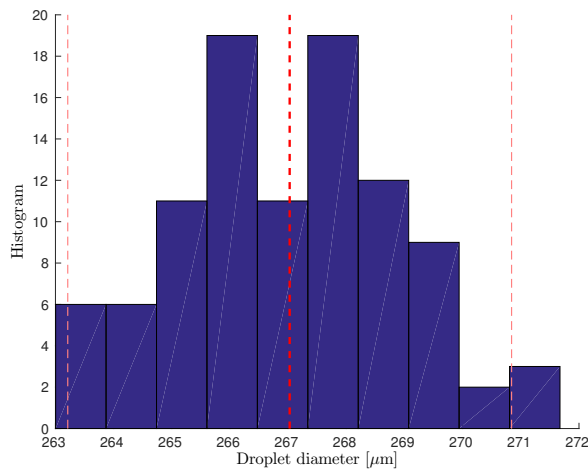
(a) Tube's outer diameter $D = 500 \mu\text{m}$, flow rate $\hat{q} = 0.5 \text{ mL/h}$, voltage $\hat{\phi}_0 = 2.95 \text{ kV}$, and tube tip to collector distance $L = 9 \text{ mm}$.



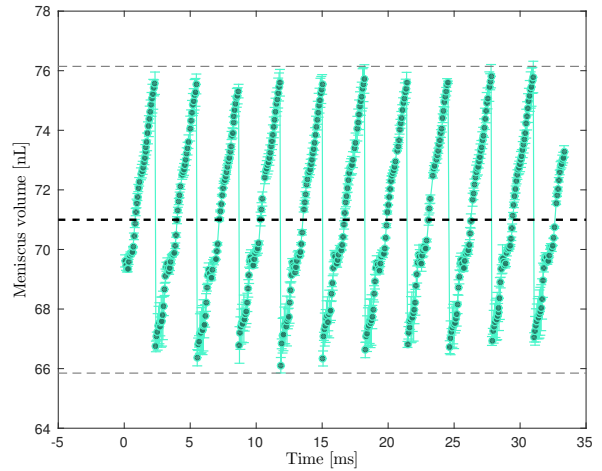
(b) Tube's outer diameter $D = 500 \mu\text{m}$, flow rate $\hat{q} = 10 \text{ mL/h}$, voltage $\hat{\phi}_0 = 2.95 \text{ kV}$, and tube tip to collector distance $L = 9 \text{ mm}$.

Figure B.4: Region classification during an oscillation period of the microdripping regime for different flow rates. Region detected as meniscus are marked with white line, those detected as droplet are marked with red line and the regions without interest are marked with green line.

respectively. The meniscus are detected and classified in practically all the frames independently on if it is in an elongated or retracted stage (see Figures B.4(a) and B.4(b)). Droplets are also accurately detected and classified even after the detachment of the ligament, when they have a non-spherical shape (see the first image of the sequence in Figure B.4(b)). Other detected regions which are not actual boundaries, like the transitions between black and white due to the lens effect inside droplets and meniscus are accurately discarded and marked with green lines in Figure B.4.



(a) Histogram of droplet diameter measured from the detected droplets in the video.



(b) Evolution of the meniscus volume versus time, for the meniscus detected in the video.

Figure B.5: Characteristics extracted from video analysis. Tube's outer diameter $D = 500 \mu\text{m}$, flow rate $\hat{q} = 10 \text{ mL/h}$, voltage $\hat{\phi}_0 = 2.95 \text{ kV}$, and tube tip to collector distance $L = 9 \text{ mm}$.

B.4 Extraction of characteristics and measurements

Once detected and classified, droplets and meniscus are tracked independently through the different frames of the videos, and the evolution with time of their shape, size and volume, among other characteristics, are obtained.

As an example, some of those characteristics obtained from video analysis are shown in Figure B.5. The histogram of droplet diameter, Figure B.5(a), measured from the same video than the sequence of images of Figure B.4(b), indicates a quite monodisperse droplet emission process, characteristic of the microdripping regime. The volume of the meniscus versus time, Figure B.5(b), has a shape of saw-tooth graphic where the meniscus volume grows linearly with time during its elongation, because the flow rate is maintained constant, and when the ligament is detached there is a sudden reduction of the volume of the meniscus.

References

- Acero, A. et al. 2013. Experimental analysis of the evolution of an electrified drop following high voltage switching. *Eur. J. Mech. B* 38, 58–64.
- Canny, J. 1986. A computational approach to edge detection. *IEEE Trans. Pattern Anal. Machine Intell.* (6), 679–698.
- Hu, M.-K. 1962. Visual pattern recognition by moment invariants. *IEEE Trans. Inf. Theory* 8(2), 179–187.
- Song, B & Springer, J. 1996. Determination of Interfacial Tension from the Profile of a Pendant Drop Using Computer-Aided Image Processing2. Experimental. *J. Colloid Interface Sci.* 184, 77–91.

Appendix C

Boundary Element Method and validation of the simulations

Contents

C.1	Laplace's equation for the velocity potential	89
C.2	Laplace's equation for the electric potential	92
C.3	Validation	93
	References	94

C.1 Laplace's equation for the velocity potential

Using Boundary Element Methods, BEM, the Laplace's equation, $\nabla^2\phi = 0$ for the velocity potential, valid inside the liquid, can be transformed into the boundary integral equation C.1, which is solved exclusively on the boundary that encloses the liquid, C_1 , including the droplet interface, $f(z, r, t) \equiv r - r(z, t) = 0$, the tube walls, and the injection tube, see Figure C.1(a). To solve equation C.1, the boundary C_1 is discretized in N linear elements of length l_i , see Figure C.1(b), where the potential, ϕ_i , and the normal component of the gradient of the potential, the normal velocity v_{ni} , are constant in each element i .

$$\phi(z_0, r_0) = -2 \int_{C_1} G(z, r, z_0, r_0) v_n(z, r) r dl + 2 \int_{C_1}^{PV} \phi(z, r) G_n(z, r, z_0, r_0) r dl, \quad (C.1)$$

where G is the appropriate Green function, $G_n = \nabla G \cdot \mathbf{n}$, PV stands for the Cauchy principal value of the integral, the normal vector \mathbf{n} points inside the liquid, and (z, r) and (z_0, r_0) are two points of the boundary. The boundary conditions are,

$$\begin{aligned} v_n &= 0, & \text{at the walls,} \\ \phi &= \phi^{int}, & \text{at the interface,} \\ v_n &= \frac{4}{\pi} q, & \text{at the injection zone.} \end{aligned}$$

From the solution of the boundary equation C.1, the normal velocity at the interface, v_n^{int} and the velocity potential at the injection tube and tube walls, ϕ^{tube} are obtained.

Using the middle points of the elements, (z_{0i}, r_{0i}) , as collocation points, the Equation C.1 can be written as



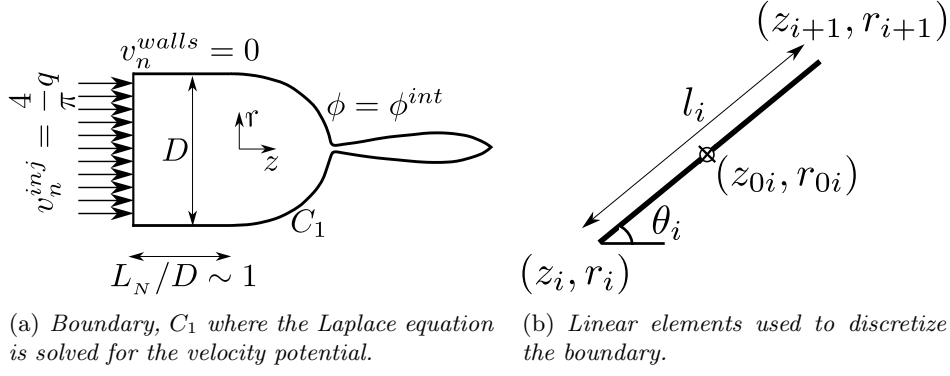


Figure C.1: Boundary of the domain discretized with linear elements, where the Laplace equation for the velocity potential is solved.

$$\phi(z_0, r_0) = -2 \sum_{i=1}^N \alpha_i(z_0, r_0) v_{ni} + 2 \sum_{i=1}^N \beta_i^{PV}(z_0, r_0) \phi_i, \quad (C.2)$$

with $\alpha_i(z_0, r_0) = \int_i G(z, r, z_0, r_0) r dl$ and $\beta_i^{PV} = \int_i^{PV} G_n(z, r, z_0, r_0) r dl$ for points (z, r) on the element i of the boundary. These integrals are approximated using Gauss-Legendre quadrature with N_q quadrature base points as

$$\alpha_i(z_0, r_0) \approx \frac{l_i}{2} \sum_{k=1}^{N_q} G(z_k, r_k, z_0, r_0) r_k \omega_k, \quad (C.3)$$

$$\beta_i^{PV}(z_0, r_0) \approx \frac{l_i}{2} \sum_{k=1}^{N_q} [n_{zi} \partial_z G(z_k, r_k, z_0, r_0) r_k \omega_k + n_{ri} \partial_r G(z_k, r_k, z_0, r_0) r_k \omega_k], \quad (C.4)$$

where (n_{zi}, n_{ri}) are the normal components of the boundary at element i , ω_k are the weights of the Gauss-Legendre quadrature, and (z_k, r_k) are N_q points at element i , with $z_k = z_{0i} + (l_i/2)\xi_k \cos(\theta_i)$ and $r_k = r_{0i} + (l_i/2)\xi_k \sin(\theta_i)$. $\xi_k \in [-1, 1]$ is the k -th root of the Legendre's polynomial of order N_q , $L_{N_q}(\xi)$.

Equation C.1 is hence written in a matrix form,

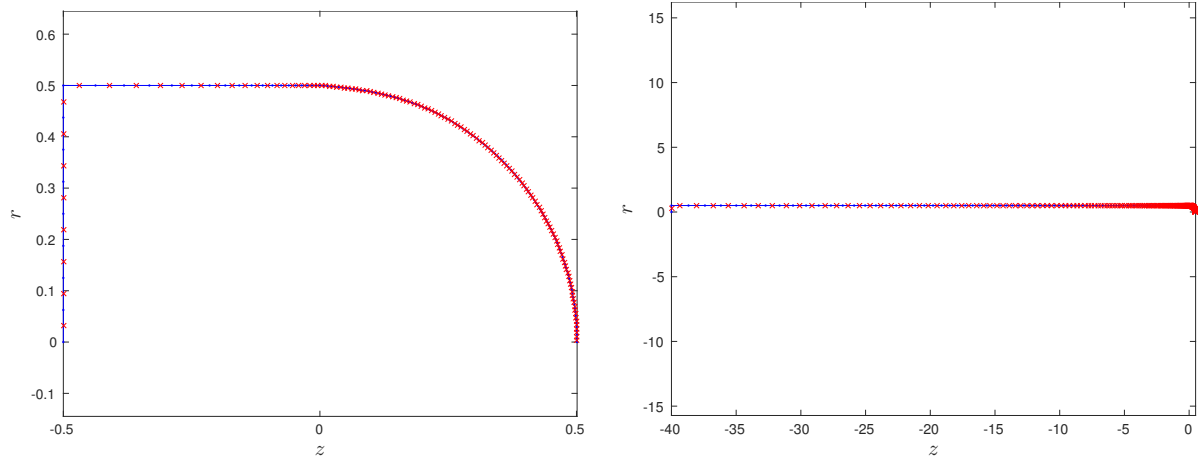
$$Av_n = (B - \frac{1}{2}I)\phi, \quad (C.5)$$

where A and B are matrices which components A_{ji} and B_{ji} are integrals $\alpha_i(z_{0j}, r_{0j})$ and $\beta_j^{PV}(z_{0j}, r_{0j})$ along element i with (z_{0j}, r_{0j}) the middle point of element j . Matrix I is the identity matrix, and ϕ and v_n are vectors with the velocity potential and normal velocity at the elements of the boundary.

The velocity potential is known at the interface, ϕ^{int} and unknown at the tube walls and injection, ϕ^{tube} . Similarly, the normal velocity is known at the tube walls and injection, v_n^{tube} and unknown at the interface, v_n^{int} . So the linear system C.5 is reordered as,

$$\begin{pmatrix} A^{int,int} & -M^{int,tube} \\ A^{tube,int} & -M^{tube,tube} \end{pmatrix} \begin{pmatrix} v_n^{int} \\ \phi^{tube} \end{pmatrix} = \begin{pmatrix} -A^{int,tube} & M^{int,int} \\ -A^{tube,tube} & M^{tube,int} \end{pmatrix} \begin{pmatrix} v_n^{tube} \\ \phi^{int} \end{pmatrix} \quad (C.6)$$

where $M = B - (1/2)I$. The linear system C.6 is solved and the normal velocity at the interface, v_n^{int} , is obtained.



(a) Points at the extremes (points) and the middle (crosses) of the linear elements used to discretize the boundary C_1 to solve the Laplace's equation for the velocity potential.

(b) Points at the extremes (points) and the middle (crosses) of the linear elements used to discretize the boundary C_2 to solve the Laplace's equation for the electric potential.

Figure C.2: Discretization.

Linear elements of equal length are distributed along the interface, a minimum of 100 elements, and the injection zone of the tube, and the tube walls are discretized with 20 elements in such a way that there is not brusque jumps in element length, as observed in Figure C.2(a). The length of the element i in the tube walls is then $l_i = L f_s^{(i-1)/(N-1)} (1 - f_s^{1/(N-1)}) / (1 - f_s^{N/(N-1)})$, where $N = 20$ is the number of elements in the tube walls, L is the length of the tube walls and equal to the tube's Diameter and f_s is the spacing factor, calculated in such a way that the elements at the extremes of the tube have equal length that the elements of the interface and injection zone, respectively.

Finally, the Green function and its gradient used to solve the Laplace's equation, for the axisymmetric case, are (see Pozrikidis 2002),

$$G(z, r, z_0, r_0) = \frac{F(k)}{\pi \sqrt{(z - z_0)^2 + (r + r_0)^2}}, \quad (\text{C.7})$$

$$\partial_z G(z, r, z_0, r_0) = -\frac{z - z_0}{4\pi} I_{30}, \quad (\text{C.8})$$

$$\partial_r G(z, r, z_0, r_0) = -\frac{1}{4\pi} (r I_{30} - r_0 I_{31}), \quad (\text{C.9})$$

where,

$$k = \sqrt{\frac{4rr_0}{(z - z_0)^2 + (r + r_0)^2}},$$

$$I_{30} = \frac{4}{((z - z_0)^2 + (r + r_0)^2)^{3/2}} \frac{E(k)}{1 - k^2},$$

$$I_{31} = \frac{4}{((z - z_0)^2 + (r + r_0)^2)^{3/2}} \frac{1}{k^2} \left(-2F(k) + \frac{2 - k^2}{1 - k^2} E(k) \right).$$

$F(k)$ and $E(k)$ are the complete elliptic integrals of the first and second kind, respectively. Singular points, $(z, r) = (z_0, r_0)$, are avoided in Integrals C.3 and C.4 evaluating the Green function and its gradient in points, $(z, r) = (z_k, r_k)$, distributed as the zeros of the Legendre's polynomial of order 4, $N_q = 4$, in each element, and the poles, (z_0, r_0) , in the middle points of the elements.

C.2 Laplace's equation for the electric potential

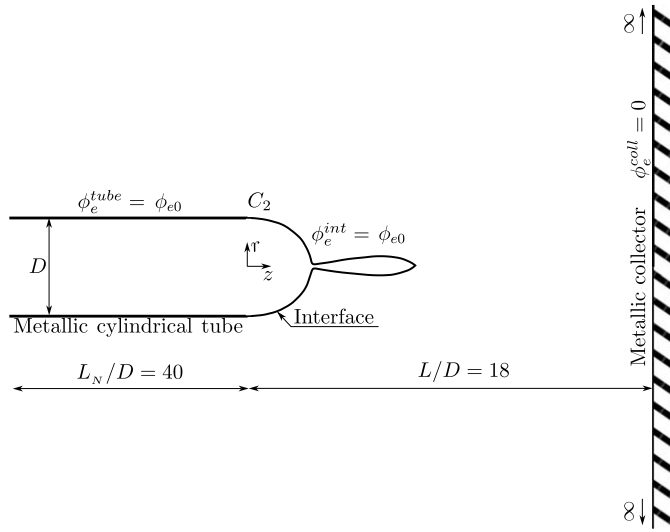


Figure C.3: Domain where the Laplace's equation is solved for the electric potential. Boundary C_2 includes the tube and the interface

The Laplace's equation $\nabla^2 \phi_e = 0$ for the electric potential, ϕ_e , is solved outside the liquid. Using Boundary Element Methods this Laplace's equation can be reduced to a boundary equation, Equation C.10, as in the case of the velocity potential, but solved in the boundary C_2 , which includes the interface and the metallic tube, and the collector plane, considering that the boundary is closed between the collector and the tube by walls located infinitely far from the interface (see Figure C.3). The infinite collector plane can be avoided making use of the Method of the Images, equivalent to adding a boundary similar to C_2 placed symmetrically respect to the collector and connected to an electric potential $\phi_e = -\phi_{e0}$. In practice, only the original boundary C_2 is discretized using a Green function G^* and its gradient (G_z^* , G_r^*). The value of ϕ_{e0} depends on the different non-dimensionalization made in Chapters 3 and 5, being $\phi_{e0} = \ln(4L/D)$ and $\phi_{e0} = 1$, respectively.

$$\phi_e(z_0, r_0) = 2 \int_{C_2} G^*(z, r, z_0, r_0) E_n(z, r) r \, dl + 2 \int_{C_2}^{PV} \phi_e(z, r) G_n^*(z, r, z_0, r_0) r \, dl, \quad (C.10)$$

with $\phi_e = \phi_{e0}$ at the tube walls and interface. The boundary condition at the collector, $\phi_e = 0$, is satisfied applying the Method of Images. The boundary is discretized with linear elements and the electric potential and normal electric field, $E_n = -\nabla \phi_e \cdot \mathbf{n}$, is constant in each element. The interface has been discretized with 100 elements of the same length, and the elements in the tube walls have a length $l_i = L f_s^{(i-1)/(N-1)} (1 - f_s^{1/(N-1)}) / (1 - f_s^{N/(N-1)})$, where at least $N = 150$, and f_s is determined to guarantee that the element close to the interface has the same length that the elements at the interface.

The boundary equation C.10 is reduced to the linear system in the same way than in Section C.1,

$$A E_n = (B - \frac{1}{2} I) \phi_e, \quad (C.11)$$

where A and B are matrices with components $A_{ji} = \frac{l_i}{2} \sum_{k=1}^{N_q} G^*(z_k, r_k, z_0, r_0) r_k \omega_k$ and $B_{ji} = \frac{l_i}{2} \sum_{k=1}^{N_q} [n_{zi} \partial_z G(z_k, r_k, z_0, r_0) r_k \omega_k + n_{ri} \partial_r G(z_k, r_k, z_0, r_0) r_k \omega_k]$, respectively.

The Green function and its gradient components are,

$$\begin{aligned} G^*(z, r, z_0, r_0) &= G(z, r, z_0, r_0) - G(z, r, z_0^{im}, r_0^{im}), \\ G_z^*(z, r, z_0, r_0) &= G_z(z, r, z_0, r_0) - G_z(z, r, z_0^{im}, r_0^{im}), \\ G_r^*(z, r, z_0, r_0) &= G_r(z, r, z_0, r_0) - G_r(z, r, z_0^{im}, r_0^{im}), \end{aligned}$$

with G , G_z and G_r such of Equations C.7, C.8 and C.9, and considering the point (z_0, r_0) and its image (z_0^{im}, r_0^{im}) , where $z_0^{im} = 2L/D - z_0$ and $r_0^{im} = r_0$.

C.3 Validation

The numerical scheme presented in this Appendix, along with the scheme presented in Appendix D to advance in time the interface, are validated here by the simulation of the resonance of inviscid free droplets in vacuum when the droplets have an electric surface charge, \hat{C}_s , assuming the drop is a perfect conductor. This problem has analytical solution for small perturbations following the linear theory presented by Rayleigh (See Rayleigh 1882). The perturbed shape of the droplet can be written as a function of spherical harmonics as $R_p(\theta) = 1 + \sum(\epsilon e^{i2\pi ft} P_n(\cos(\theta)))$, where R_p is the radial position of the droplet interface for a given unperturbed spherical droplet of radius R , $\epsilon \ll 1$ is the amplitude of the oscillations, f the frequency of the oscillations and $P_n(\cos(\theta))$ the Legendre's polynomial of order n (See Figure C.4(a)). The frequency f , non-dimensionalized with the capillary time, $t_c = \sqrt{\rho R^3/\gamma}$ can be expressed as a function of the Electric Bond number, $B_E = \hat{C}_s^2 R/(\epsilon_0 \gamma)$,

$$f = \frac{1}{2\pi} \sqrt{n(n-1)(n+2) - B_E n(n-1)}, \quad (\text{C.12})$$

for any integer $n \geq 2$.

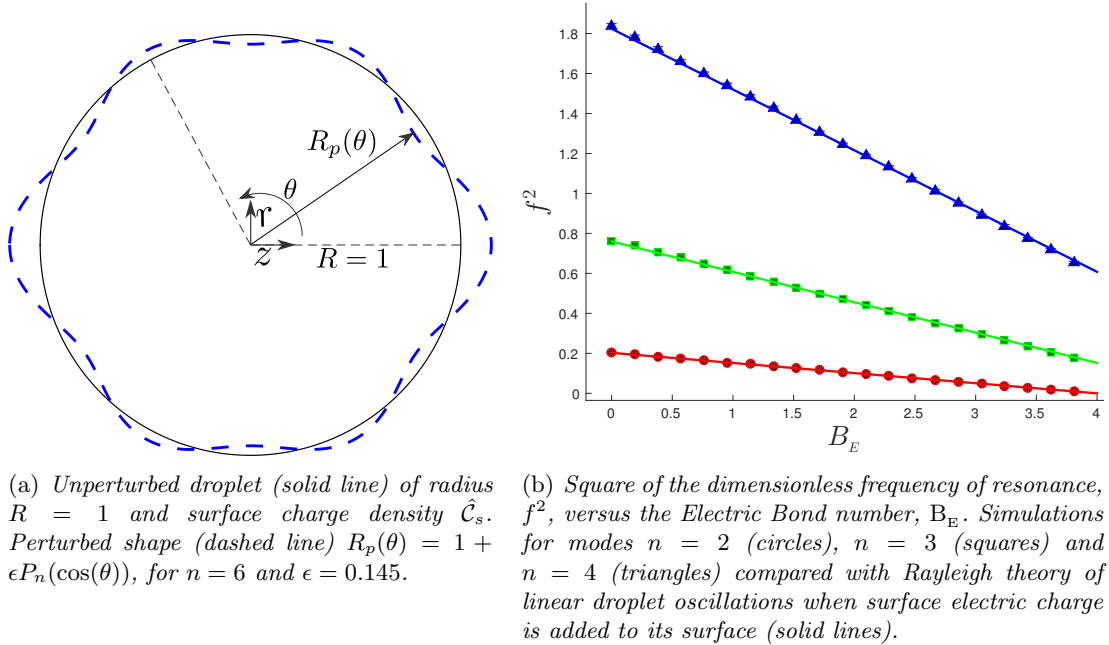


Figure C.4: Validation. Resonance of free charged droplets.

To perform the simulations half of the interface has been discretized in 100 linear elements of equal size, with $z = 0$ the axis of symmetry. The axisymmetric Boundary Element Method presented in Sections C.1 and C.2 have been used to solve the Laplace's equation for the velocity

potential inside the droplet, and the Laplace's equation outside the droplet for electric potential. As boundary conditions, the dimensionless electric potential on the droplet's surface is $\phi_e = 1$, taking as characteristic voltage $\phi_0 = \hat{C}_s R / \epsilon_0$, and $\phi_e = 0$ infinitely far from the droplet. The initial shape of the droplet is a hemisphere of radius $R = 1$ perturbed as $R_p(\theta) = 1 + 0.001 \text{rand}(\theta)$, where $\text{rand}(\theta)$ is a function which gives a normally distributed random number between -1 and 1 for each θ . The position (z, r) of the droplet's interface and its velocity potential, ϕ , is evolved in time using the adaptive scheme of Appendix D for 200 capillary times.

The first three frequencies of resonance, obtained from the Fourier transform of the axial position versus time at the point $(z, r = 0)$ of the interface, are represented in Figure C.4(b) respect to the Electric Bond number for $n = 2$ (circles), $n = 3$ (squares) and $n = 4$ (triangles). The results agree very well with Rayleigh theory, Equation C.12 (solid lines), and the droplet becomes unstable when $B_E = 4$, that is, when the total charge of the droplet is the Rayleigh charge $C_R = 8\pi\sqrt{\epsilon_0\gamma R^3}$.

References

- Pozrikidis, C. 2002. *A practical guide to boundary element methods with the software library BEMLIB*. CRC Press, Inc. Boca Raton, FL, USA.
- Rayleigh, L. 1882. XX. On the equilibrium of liquid conducting masses charged with electricity. *Philos. Mag.* 14(87), 184–186.

Appendix D

Adaptive Runge-Kutta method

Contents

References	97
----------------------	----

An adaptive Runge-Kutta-Fehlberg method (Mathews et al. 1999) has been used to advance in time the simulations of Chapters 3 and 5. The problem to solve on the liquid meniscus can be written in a compact form as $\mathbf{dy}/dt = \mathbf{f}(t, \mathbf{y}, E_n, v_n)$, where the normal velocity v_n and the normal electric field E_n are obtained solving the respective Laplace equations for the velocity and electric potential, ϕ and ϕ_e . The vector \mathbf{y} stands for $\mathbf{y} = (r, z, \phi)$, with z and r the axial and radial component of the position of a set of points equally spaced along the meniscus interface. The vector \mathbf{f} is $\mathbf{f} = (v_r, v_z, 1/2(v_n^2 + v_s^2) + 1/2 B_E E_n^2 + Bz - k_u + c(t))$, with $v_s = d\phi/ds$ the tangential velocity, $k_u = -d\theta/ds + \cos(\theta)/r$ the curvature of the interface, B_E the Electric Bond number, and B the Bond number. s is the arc length and θ the slope angle, with $\tan(\theta) = dz/dr$. The singularity in the curvature at $r = 0$ is solved taking in account that $k_u \rightarrow -2d\theta/ds$ when $r \rightarrow 0$. The constant $c(t)$ from the dynamic condition at the interface can be taken to impose that $\phi = 0$ at the junction of the interface and the tube or supporting surface.

Given the solution, \mathbf{y}_n , at the current time, t_n , and a time step, Δt , the solution at a time $t_n + \Delta t$, \mathbf{y}_{n+1} , can be estimated with an error of the order of Δt^4 and Δt^5 with Equations D.1 and D.2, respectively.

$$\mathbf{y}_{n+1}^{(4)} = \mathbf{y}_n + \Delta t \left(\frac{25}{216} K_1 + \frac{1408}{2565} K_3 + \frac{2197}{4104} K_4 - \frac{1}{5} K_5 \right), \quad (\text{D.1})$$

$$\mathbf{y}_{n+1}^{(5)} = \mathbf{y}_n + \Delta t \left(\frac{16}{135} K_1 + \frac{6656}{12825} K_3 + \frac{28561}{56430} K_4 - \frac{9}{50} K_5 + \frac{2}{55} K_6 \right), \quad (\text{D.2})$$

where:

$$\begin{aligned} K_1 &= \mathbf{f}(t_n, \mathbf{y}_n), \\ K_2 &= \mathbf{f}\left(t_n + \frac{1}{4}\Delta t, \mathbf{y}_n + \frac{1}{4}\Delta t K_1\right), \\ K_3 &= \mathbf{f}\left(t_n + \frac{3}{8}\Delta t, \mathbf{y}_n + \frac{3}{32}\Delta t K_1 + \frac{9}{32}\Delta t K_2\right), \\ K_4 &= \mathbf{f}\left(t_n + \frac{12}{13}\Delta t, \mathbf{y}_n + \frac{1932}{2197}\Delta t K_1 - \frac{7200}{2197}\Delta t K_2 + \frac{7296}{2197}\Delta t K_3\right), \\ K_5 &= \mathbf{f}\left(t_n + \Delta t, \mathbf{y}_n + \frac{439}{216}\Delta t K_1 - 8\Delta t K_2 + \frac{3680}{513}\Delta t K_3 - \frac{845}{4104}\Delta t K_4\right), \\ K_6 &= \mathbf{f}\left(t_n + \frac{1}{2}\Delta t, \mathbf{y}_n - \frac{8}{27}\Delta t K_1 + 2\Delta t K_2 - \frac{3544}{2565}\Delta t K_3 + \frac{1859}{4104}\Delta t K_4 - \frac{11}{40}\Delta t K_5\right). \end{aligned}$$



The local error of the solution is then estimated as $RKE = |\mathbf{y}_{n+1}^{(5)} - \mathbf{y}_{n+1}^{(4)}|$. And the time step Δt is modified if RKE is higher than a certain tolerance. More specifically, a parameter $E = \|RKE/(Tol_r|\mathbf{y}_{n+1}^{(4)}| + Tol_{abs})\|$ is defined and if $E > 1$ the time step is reduced, $\Delta t = \Delta t/1.2$ and the iteration repeated, if $E < 0.05$ the time step is increased, $\Delta t = 1.2\Delta t$, or maintained otherwise. Tol_r and Tol_{abs} are the relative and absolute tolerances, which have been fixed to 1×10^{-4} and 1×10^{-7} in the simulations, and the symbol $\|\cdot\|$ stands for the 2-norm of a vector.

This adaptive approach allows to automatically reduce the time step during the simulations, specially when the pinch-off of the droplets emitted from the meniscus is about to occurs, and increased afterwards when the meniscus is receding or elongating.

Once evolved the interface, the new points (z, r) are first filtered (Pozrikidis 2002) using the five points averaging formula D.3 and D.4, to avoid the growth of numerical instabilities, and them re-sampled using cubic spline interpolation, to assure that the points are equally distributed in arc length.

$$z_j = \frac{1}{16} (-z_{j-2} + 4z_{j-1} + 10z_j + 4z_{j+1} - z_{j+2}), \quad (D.3)$$

$$r_j = \frac{1}{16} (-r_{j-2} + 4r_{j-1} + 10r_j + 4r_{j+1} - r_{j+2}), \quad (D.4)$$

where the subindex j goes from 1 to N sweeping the different points on the interface.

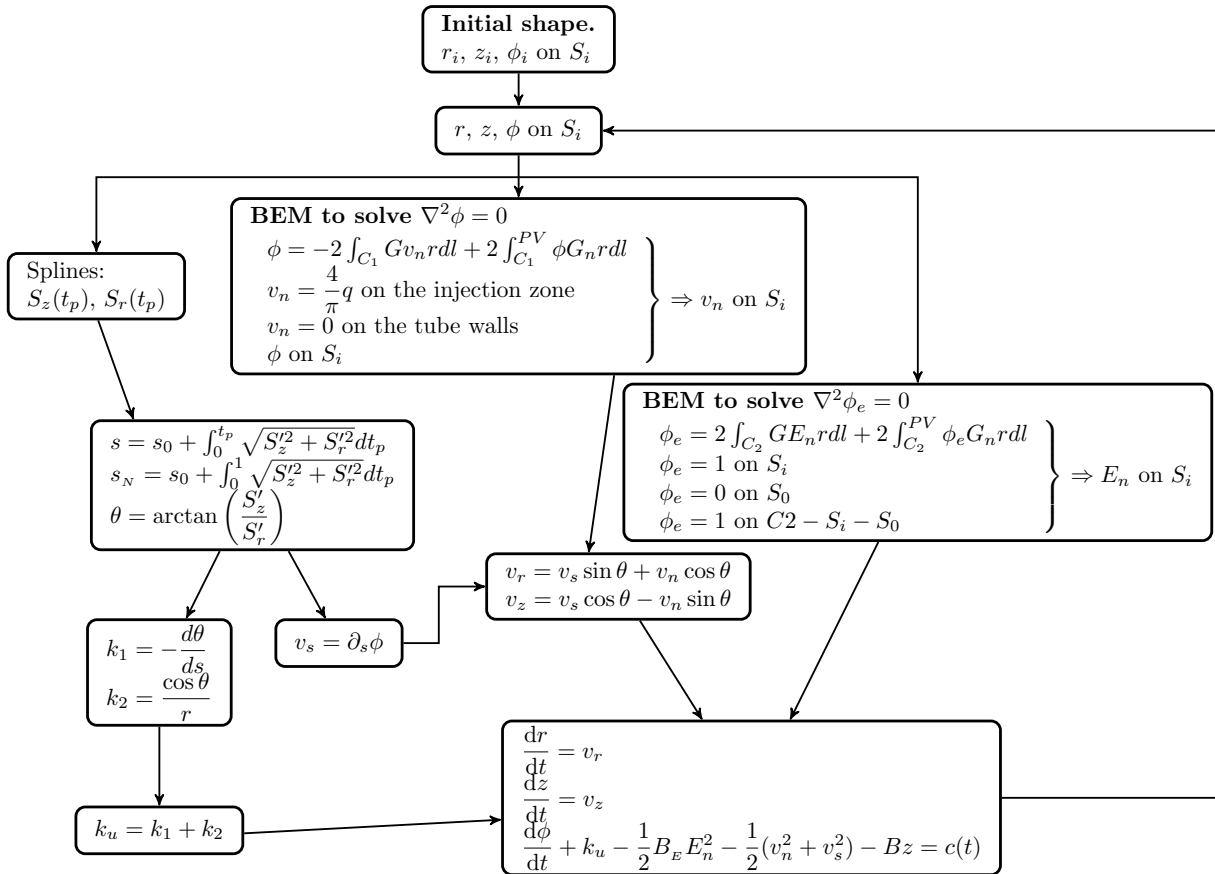


Figure D.1: Simulations flow chart.

The chart of Figure D.1 shows the different steps followed to advance in time the simulations once solved, respectively, the Laplace equations for the electric field, on the boundary C_2 , and for the velocity potential, on the boundary C_1 . In this chart S_i is the part of boundaries C_1 and C_2 that corresponds with the interface, and S_0 the part of C_2 connected to ground voltage, $\phi_e = 0$. $S_z(t_p)$ and $S_r(t_p)$ are the cubic splines used to re-sample the interface, as a function

of a parameter t_p which goes from $t_p = 0$ at the connection of the meniscus and the tube, to $t_p = 1$ at the meniscus tip. k_1 and k_2 are, respectively, the in-plane and azimuthal curvature, being $k_2(r \rightarrow 0) = k_1(r \rightarrow 0)$.

References

- Mathews, J. H. & Fink, K. D. 1999. *Numerical methods using MATLAB*. Vol. 31. Prentice hall Upper Saddle River, NJ.
- Pozrikidis, C. 2002. *A practical guide to boundary element methods with the software library BEMLIB*. CRC Press, Inc. Boca Raton, FL, USA.



Appendix E

Analytical solution of the resonance frequency of a droplet pinned to a circle without outer medium

Contents

E.1 Non electrified droplets	99
E.2 Electrified droplets	101
References	102

E.1 Non electrified droplets

Consider an unperturbed droplet of radius R presented in the sketch of Figure E.1. This droplet is pinned to a circle of radius $a = 1$ indicated by the dots. The inner liquid is considered inviscid and incompressible, there is no outer medium, and gravity is neglected. In this geometry it is studied the evolution of small axisymmetric deformation, $\eta(t, \alpha)$, in a similar way than in Bostwick et al. 2009, but for the lack of an outer medium here.

The velocity field may be expressed as $\mathbf{v} = \nabla\phi$, and thus the Laplace's equation for the velocity potential ϕ must be solved,

$$\nabla^2\phi = \partial_r^2\phi + \frac{2}{r}\partial_r\phi + \frac{1}{r^2}\partial_\alpha^2\phi + \frac{1}{r^2\tan\alpha}\partial_\alpha\phi = 0 \quad (\text{E.1})$$

expressed in spherical coordinates (r, α, φ) , with $\alpha \in [0, \pi]$. The kinematic and dynamic conditions must be satisfied on the droplet's surface,

$$\frac{df_c}{dt} = 0, \quad (\text{E.2})$$

$$\partial_t\phi + \frac{1}{2}(\nabla\phi \cdot \nabla\phi) = -k_u + C, \quad (\text{E.3})$$

where t is the time, $f_c = r - R - \eta(t, \alpha)$, $k_u = \nabla \cdot (\nabla f_c / |\nabla f_c|)$ the curvature, and C a constant. Equations E.1 to E.3 are subjected to the following boundary conditions: *i*) the surface is pinned at the point (R, α_0) and then $\eta(t, \alpha_0) = 0$, *ii*) symmetry condition, $1/r\partial_\alpha\phi|_{\alpha=0,\pi} = 0$, and *iii*) the solution must be finite at the center of the droplet, $|\phi(t, r = 0, \alpha) < \infty|$

All the equations are written in dimensionless form, following the non-dimensionalization of chapter 5. In this context a solution of the form E.4 to E.5 is proposed, with $\omega = 2\pi f$, being f the dimensionless frequency, ϵ the small amplitude of the perturbation, and $f_1(t)$, $g_1(\alpha)$, and $g_2(r)$ unknown functions of t , α , and r , respectively.

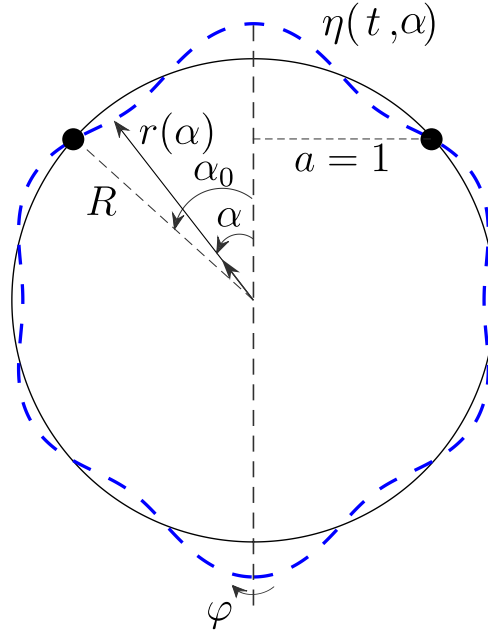


Figure E.1: Sketch of a droplet of radius R pinned to a circle of radius $a = 1$.

$$\eta(t, \alpha) = \epsilon e^{i\omega t} g_1(\alpha), \quad (\text{E.4})$$

$$\phi(t, r, \alpha) = \epsilon f_1(t) g_1(\alpha) g_2(r). \quad (\text{E.5})$$

Applying now the cinematic condition E.2 the function $f_1(t)$ is obtained as,

$$f_1(t) = \frac{i\omega}{g_2'(R) + g_2''(R)\eta} e^{i\omega t}, \quad (\text{E.6})$$

with $g_2'(R)$ denoting $dg_2(r)/dr|_{r=R}$. And using E.4 to E.5, the Laplace's equation E.1 can be transformed to two separate equations, one in r and other in α :

$$\frac{g_1''}{g_1} + \frac{1}{\tan \alpha} \frac{g_1'}{g_1} = -l(l+1), \quad (\text{E.7})$$

$$r^2 \frac{g_2''}{g_2} + 2r \frac{g_2'}{g_2} = l(l+1), \quad (\text{E.8})$$

with l a constant. Equation E.7 can be identified as the Legendre's equation, and has a general solution $g_1(\alpha) = C_1 P_l(\cos \alpha) + C_2 Q_l(\cos \alpha)$, and equation E.8 has solution $g_2(r) = C_3 r^l + C_4 r^{-l-1}$. Where C_1 to C_4 are constants, P_l is the Legendre function of first kind and Q_l the Legendre function of second kind.

$$\eta = \epsilon e^{i\omega t} P_l(\cos \alpha), \quad (\text{E.9})$$

$$\phi = \epsilon f_1(t) P_l(\cos \alpha) r^l, \quad (\text{E.10})$$

$$P_l(\cos \alpha_0) = 0 \Rightarrow l = l_1, l_2, l_3, \dots \quad (\text{E.11})$$

$$f_1(t) = \frac{i\omega}{lR^{l-1}} e^{i\omega t}. \quad (\text{E.12})$$

Using now the boundary conditions, the constant l are the zeros of the Legendre function $P_l(\cos \alpha_0) = 0$, from the pinning condition to the circle at $\alpha = \alpha_0$; and the constants C_2 and

C_4 are $C_2 = 0$ and $C_4 = 0$ due, respectively, to symmetry condition, and that the center of the droplet requires that $|\phi(t, r = 0, \alpha) < \infty|$. The solution for η and ϕ can now be written as:

$$k_u = \frac{2}{r} - \epsilon \frac{\sin^2 \alpha}{r^2} e^{i\omega t} P_l''(\cos \alpha) + \epsilon \frac{\cos \alpha}{r^2} e^{i\omega t} P_l'(\cos \alpha). \quad (\text{E.13})$$

Making now use of this solution and applying the dynamic condition at the droplet's surface, equation E.3, where the curvature can be written as E.13 for small perturbations, allows to obtain the compact expression of equation E.14 for the resonance frequency f of an inviscid droplet of radius R pinned to a circle of radius a .

$$f = \frac{1}{2\pi} R^{-3/2} \sqrt{l(l-1)(l+2)}. \quad (\text{E.14})$$

E.2 Electrified droplets

Considering now the droplet of section E.1 as a perfect conductor, and connecting it to a dimensionless voltage $\phi_e = 1$ respect to a concentric spherical counter electrode of radius $R + b$ connected to a voltage $\phi_e = 0$, as sketched in Figure E.2, the solutions E.9 to E.12 are valid, because the unperturbed shape of the droplet continues being a sphere of radius R due to spherical symmetry. But now a new term appears on the right hand side of equation E.3:

$$\partial_t \phi + \frac{1}{2} (\nabla \phi \cdot \nabla \phi) = \frac{1}{2} B_E E_n^2 - k_u + C, \quad (\text{E.15})$$

with B_E the Electric Bond number and E_n the normal electric field to the droplet's surface. To obtain the electric field at the droplet's surface, the Laplace's equation for the electric potential ϕ_e is solved subjected to the boundary conditions,

$$\phi_e(t, R + \eta, \alpha) = 1, \quad (\text{E.16})$$

$$\phi_e(t, R + b, \alpha) = 0, \quad (\text{E.17})$$

and assuming a solution of the form,

$$\phi_e(t, r, \alpha) = \Phi_e(r) + \epsilon e^{i\omega t} h_1(\alpha) h_2(r), \quad (\text{E.18})$$

with $h_1(\alpha)$ and $h_2(r)$ unknown functions of α and r , respectively.

The Laplace's equation for the electric potential can be solved in a similar way than the Laplace's equation for the velocity potential in section E.1, satisfying the boundary conditions E.16 to E.17 and taking into account small perturbations and that the solution must be axisymmetric, the following solution for the electric potential is obtained:

$$\phi_e(t, r, \alpha) = \frac{R(R+b)}{rb} - \frac{R}{b} + \epsilon e^{i\omega t} P_l(\cos \alpha) (A_1 r^l + A_2 R^{-1-l}), \quad (\text{E.19})$$

where A_1 and A_2 are geometric constants:

$$A_1 = -\frac{R^l(R+b)}{b^2(R+b)^{2l} + Rb(R+b)^{2l} - bR^{2l+1}}, \quad (\text{E.20})$$

$$A_2 = -\frac{(R+b)^{l+1}}{Rb \left[\frac{R^l}{(R+b)^{l+1}} - \frac{(R+b)^l}{R^{l+1}} \right]}. \quad (\text{E.21})$$

The electric field at the droplet's surface, obtained from making $E_n = \sqrt{(\partial_r \phi_e)^2 + (1/r \partial_\alpha \phi_e)^2}|_{r=R+\eta}$, is introduced in the dynamic condition at the interface,

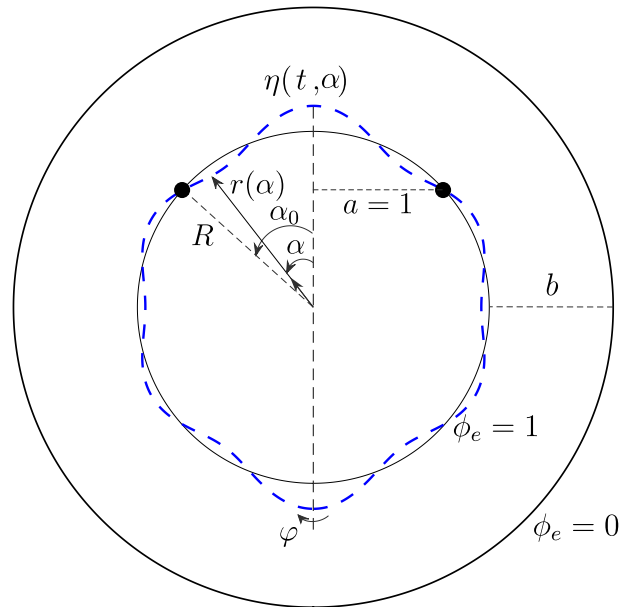


Figure E.2: Sketch of an electrified droplet of radius R pinned to a circle of radius $a = 1$.

equation E.15, and an expression for the resonance frequency of electrified droplets is obtained, when the unperturbed shape of the droplet is a sphere:

$$f = \sqrt{\frac{1}{4\pi^2 R^3} [l(l-1)(l+2)] - B_E \frac{A_3}{4\pi^2}}, \quad (\text{E.22})$$

with A_3 a geometric constant,

$$A_3 = l \frac{R^2 + R + b}{R^2 b} \left[-\frac{2(R+b)}{R^2 b} - A_1 l R^{l-1} + A_2 (1+l) R^{-2-l} \right]. \quad (\text{E.23})$$

The expression E.22 can be rewritten as,

$$f^2 = f_{ne}^2 - B_E \frac{A_3}{4\pi^2}, \quad (\text{E.24})$$

where f is the resonance frequency of the electrified droplet, and f_{ne} is the resonance frequency of the same non-electrified droplet.

References

- Bostwick, J. B. & Steen, P. H. 2009. Capillary oscillations of a constrained liquid drop. *Phys. Fluids* 21(3), 032108.

Alphabetical list of references

- Acero, A. et al. 2013. Experimental analysis of the evolution of an electrified drop following high voltage switching. *Eur. J. Mech. B* 38, 58–64.
- Alexander, M. S. 2008. Pulsating electrospray modes at the liquid-liquid interface. *Appl. Phys. Lett.* 92(14), 144102.
- Allmaier, G. 1997. Picoliter to nanoliter deposition of peptide and protein solutions for matrix-assisted laser desorption/ionization mass spectrometry. *Rapid Commun. Mass Spectrom.* 11, 1567–1569.
- Ashley, S. 1995. Rapid prototyping is coming of age. *Mech. Eng.* 117, 62–68.
- Barrero, A. & Loscertales, I. G. 2007. Micro- and nanoparticles via capillary flows. *Annu. Rev. Fluid Mech.* 39, 89–106.
- Barrero, a. et al. 2004. Steady cone-jet electrosprays in liquid insulator baths. *J. Colloid Interface Sci.* 272(1), 104–108.
- Basaran, O, Gao, H, & Bhat, P. 2013. Nonstandard inkjets. *Annu. Rev. Fluid Mech.* 45(1), 85–113.
- Basaran, O. A. 2002. Small-scale free surface flows with breakup: Drop formation and emerging applications. *AIChE Journal* 48(9), 1842–1848.
- Basaran, O. A. & Scriven, L. 1990. Axisymmetric shapes and stability of pendant and sessile drops in an electric field. *J. Colloid Interface Sci.* 140(1), 10–30.
- Bostwick, J. B. & Steen, P. H. 2009. Capillary oscillations of a constrained liquid drop. *Phys. Fluids* 21(3), 032108.
- Calvo, A. M. GAÑÁN & Gordillo, J. M. 2001. Perfectly monodisperse microbubbling by capillary flow focusing. *Phys. Rev. Lett.* 87(27), 274501.
- Canny, J. 1986. A computational approach to edge detection. *IEEE Trans. Pattern Anal. Machine Intell.* (6), 679–698.
- Castro-Hernández, E. et al. 2009. Scaling the drop size in coflow experiments. *New J. Phys.* 11(7), 075021.
- Castro-Hernández, E. et al. 2011. Microbubble generation in a co-flow device operated in a new regime. *Lab on a Chip* 11(12), 2023–2029.

- Celestini, F. & Kofman, R. 2006. Vibration of submillimeter-size supported droplets. *Phys. Rev. E: Stat., Nonlinear, Soft Matter Phys.* 73(2006), 1–6.
- Chen, C. H., Seville, D. a., & Aksay, I. a. 2006. Scaling laws for pulsed electrohydrodynamic drop formation. *Appl. Phys. Lett.* 89(12), 2005–2007.
- Chen, X. et al. 2005. Spraying modes in coaxial jet electrospray with outer driving liquid. *Phys. Fluids* 17(3), 032101.
- Choi, H. K. et al. 2008. Scaling laws for jet pulsations associated with high-resolution electrohydrodynamic printing. *Appl. Phys. Lett.* 92(12), 2006–2009.
- Clift, R., Grace, J. R., & Weber, M. E. 2005. *Bubbles, drops, and particles*. Courier Corporation.
- Cloupeau, M. & Prunet-Foch, B. 1994. Electrohydrodynamic spraying functioning modes: a critical review. *J. Aerosol Sci.* 25(6), 1021–1036.
- Cohen, I. 2001. Using Selective Withdrawal to Coat Microparticles. *Science* 292(5515), 265–267.
- Cox, W. R. et al. 2000a. “Micro-jet printing of refractive microlenses”. *OSA Diffractive Optics and Micro-Optics Topical Meeting, Kailua-Kona, Hawaii*.
- Cox, W. R. et al. 2000b. Microjet printing of micro-optical interconnects. *Int. J. Microcircuits Electronic Packaging* 23, 346–352.
- Dulikravich, G. S. & Lynn, S. R. 1997. Unified Electro-Magneto-Fluid (EMFD): A Survey of Mathematical Models. *Int. J. Nonlinear Mech.* 32(5), 923–932.
- ElShafei, G. M. et al. 2010. Environmentally friendly pesticides: Essential oil-based w/o/w multiple emulsions for anti-fungal formulations. *Industrial Crops and Products* 31(1), 99–106.
- Englert, D. 2000. Production of microarrays on porous substrates using noncontacting piezoelectric dispensing. *Microarray Biochip Technology*, 231–246.
- Fenn, J. B. et al. 1989. Electrospray ionization for mass spectrometry of large biomolecules. *Science* 246, 64–71.
- Fernández Fera, R. 2001. *Mecánica de fluidos*. Universidad de Málaga / Manuales.
- Fernández de la Mora, J. 2007. The Fluid Dynamics of Taylor Cones. *Annu. Rev. Fluid Mech.* 39(1), 217–243.
- Fernández de la Mora, J. & Loscertales, I. G. 1994. Current emitted by highly conducting Taylor cones. *J. Fluid Mech.* 260, 155–184.
- Freitas Jr., R. A. 1999. *Nanomedicine, Volume I: Basic capabilities*. Landes Bioscience, Georgetown, TX.
- Gabriel, G. C. 1999. Microarrays: Existing and evolving genomic platforms. *Biomed. Prod.* 10, 26.

- Gallier-Beckley, A et al. 2015. Characterization of a novel oil-in-water emulsion adjuvant for swine influenza virus and Mycoplasma hyopneumoniae vaccines. *Vaccine* 33(25), 2903–2908.
- Galliker, P. et al. 2012. Direct printing of nanostructures by electrostatic autofocussing of ink nanodroplets. *Nat. Commun.* 3(May), 890.
- Galus, S. & Kadzińska, J. 2015. Food applications of emulsion-based edible films and coatings. *Trends in Food Science & Technology* 45(2), 273–283.
- Gao, F. Q. & Sonin, A. A. 1994. Precise deposition of molten microdrops: The physics of digital microfabrication. *Proc. R. Soc. London A* 444, 533–554.
- Glampedaki, P. & Dutschk, V. 2014. Stability studies of cosmetic emulsions prepared from natural products such as wine, grape seed oil and mastic resin. *Colloids Surf., A* 460, 306–311.
- Guerrero, J. et al. 2014. Whipping of electrified liquid jets. *Proc. Natl. Acad. Sci. U.S.A.* 111(38), 13763–13767.
- Guillot, P. et al. 2007. Stability of a jet in confined pressure-driven biphasic flows at low Reynolds numbers. *Phys. Rev. Lett.* 99(10), 104502.
- Gundabala, V. R., Vilanova, N., & Fernández-Nieves, A. 2010. Current-Voltage characteristic of electrospray processes in microfluidics. *Phys. Rev. Lett.* 105(October), 1–4.
- Gundabala, V. et al. 2013. “Method and Electro-Fluidic Device to produce emulsions and particle suspensions”. Patent US 2013/0277461 A1 (US).
- Hayes, D. J., Wallace, D. B., & Cox, W. R. 1999. “Microjet printing of solder and polymers for multi-chip modules and chip-scale packages”. *Proceedings IMAPS 99, Chicago*.
- Hayes, D. J., Cox, W. R., & Grove, M. E. 2001. Low-cost display assembly and interconnects using ink-jet printing technology. *J. Society Information Display* 9, 9–13.
- Higuera, F. J. 2003. Flow rate and electric current emitted by a Taylor cone. *J. Fluid Mech.* 484, 303–327.
- Higuera, F. J. et al. 2013a. Pulsating emission of droplets from an electrified meniscus. *J. Aerosol Sci.* 66, 193–208.
- Higuera, F. J. et al. 2013b. Pulsating emission of droplets from an electrified meniscus. *J. Aerosol Sci.* 66, 193–208.
- Hill, R. & Eaves, L. 2010. Vibrations of a diamagnetically levitated water droplet. *Phys. Rev. E: Stat., Nonlinear, Soft Matter Phys.* 81(5), 056312.
- Hill, R. & Eaves, L. 2012. Shape oscillations of an electrically charged diamagnetically levitated droplet. *Appl. Phys. Lett.* 100(11), 114106.
- Hohman, M. M. et al. 2001. Electrospinning and electrically forced jets. I. Stability theory. *Physics of fluids* 13(8), 2201–2220.

- Hu, M.-K. 1962. Visual pattern recognition by moment invariants. *IEEE Trans. Inf. Theory* 8(2), 179–187.
- Hulett, H. et al. 1969. Cell sorting: automated separation of mammalian cells as a function of intracellular fluorescence. *Science* 166, 747–749.
- Jaworek, a. & Krupa, A. 1999. Classification of the modes of EHD spraying. *J. Aerosol Sci.* 30(7), 873–893.
- Jiménez-Colmenero, F. 2013. Potential applications of multiple emulsions in the development of healthy and functional foods. *Food research international* 52(1), 64–74.
- Juraschek, R. & Röllgen, F. 1998. Pulsation phenomena during electrospray ionization. *Int. J. Mass Spectrom.* 177, 1–15.
- Kang, D. K. et al. 2011. Electrohydrodynamic pulsed-inkjet characteristics of various inks containing aluminum particles. *J. Aerosol Sci.* 42(10), 621–630.
- Kelvin, L. 1890. Mathematical and physical papers. 3, 384.
- Kim, J., Oh, H., & Kim, S. S. 2008. Electrohydrodynamic drop-on-demand patterning in pulsed cone-jet mode at various frequencies. *J. Aerosol Sci.* 39(9), 819–825.
- Kling, J. 2001. MALDI chip shot. *Anal. Chem.* 73, 68A–70A.
- Krasodomska, O. & Jungnickel, C. 2015. Viability of fruit seed oil O/W emulsions in personal care products. *Colloids Surf., A* 481, 468–475.
- Krupa, A & Jaworek, A. 1999. Spherical Probe for Measuring Aerosol Mass Flow Rate. *J. Aerosol Sci.* 30(1), 377–378.
- Lamb, H. 1932. *Hydrodynamics*. Cambridge University Press, Cambridge, England.
- Landau, L. D. et al. 1984. *Electrodynamics of continuous media*. Vol. 8. elsevier.
- Landau, L. D. & Lifshitz, E. 1987. *Fluid Mechanics; 2nd Edition*. Vol. 6. Butterworth-Heinemann.
- Larriba, C. & Fernández de la Mora, J. 2011. Production of monodisperse submicron drops of dielectric liquids by charge-injection from highly conducting liquids. *Phys. Fluids* 23(10), 102003.
- Lee, M. W. et al. 2012. A study of ejection modes for pulsed-DC electrohydrodynamic inkjet printing. *J. Aerosol Sci.* 46, 1–6.
- Lee, S. et al. 2008. Pole-type ground electrode in nozzle for electrostatic field induced drop-on-demand inkjet head. *Sensors Actuators A: Physical* 141, 506–514.
- Li, L., Breedveld, V., & Hess, D. W. 2012. Creation of superhydrophobic stainless steel surfaces by acid treatments and hydrophobic film deposition. *ACS Appl. Mater. Interfaces* 4(9), 4549–4556.

- Li, Y., Chen, P.-S., & Huang, S.-D. 2013. Water with low concentration of surfactant in dispersed solvent-assisted emulsion dispersive liquid-liquid microextraction for the determination of organochlorine pesticides in aqueous samples. *J. Chromatogr., A* 1300, 51–57.
- Litborn, E., Stjernström, M., & Roeraade, J. 1998. Nanoliter titration based on piezoelectric drop-on-demand technology and laser-induced fluorescence detection. *Anal. Chem.* 70, 4847–4852.
- Marginean, I., Nemes, P., & Vertes, A. 2007. Astable regime in electrosprays. *Phys. Rev. E* 76, 026320.
- Marginean, I. et al. 2006a. How much charge is there on a pulsating Taylor cone? *Appl. Phys. Lett.* 89(6), 064104.
- Marginean, I., Nemes, P., & Vertes, A. 2006b. Order-chaos-order transitions in electrosprays: The electrified dripping faucet. *Phys. Rev. Lett.* 97(6), 064502.
- Mathews, J. H. & Fink, K. D. 1999. *Numerical methods using MATLAB*. Vol. 31. Prentice hall Upper Saddle River, NJ.
- Miao, P., Balachandran, W., & Xiao, P. 2002. Formation of ceramic thin films using electrospray in cone-jet mode. *IEEE Trans. Ind. Appl.* 38(1), 50–56.
- Miller, C. a. & Scriven, L. E. 1968. The oscillations of a fluid droplet immersed in another fluid. *J. Fluid Mech.* 32(03), 417.
- Mishra, S. et al. 2010. High-speed and drop-on-demand printing with a pulsed electrohydrodynamic jet. *J. Micromech. Microeng.* 20, 095026.
- Nitsche, M. & Steen, P. H. 2004. Numerical simulations of inviscid capillary pinchoff. *Journal of Computational Physics* 200(1), 299–324.
- Noblin, X., Buguin, a., & Brochard-Wyart, F. 2004. Vibrated sessile drops: Transition between pinned and mobile contact line oscillations. *Eur. Phys. J. E* 14(4), 395–404.
- Orme, M. et al. 2000. Electrostatic charging and detection of nonconventional droplet streams formed from capillary stream breakup. *Phys. Fluids* 12, 2224–2235.
- Patrascioiu, A et al. 2011. Liquids microprinting through a novel film-free femtosecond laser based technique. *Appl. Surf. Sci.* 257(12), 5190–5194.
- Pozrikidis, C. 2002. *A practical guide to boundary element methods with the software library BEMLIB*. CRC Press, Inc. Boca Raton, FL, USA.
- Prosperetti, A. 1980. Free oscillations of drops and bubbles: the initial-value problem. *J. Fluid Mech.* 100(02), 333.
- Ramos, A & Castellanos, A. 1994. Equilibrium shapes and bifurcation of captive dielectric drops subjected to electric fields. *J Electrostat* 33(1), 61–86.
- Rayleigh, L. 1882. XX. On the equilibrium of liquid conducting masses charged with electricity. *Philos. Mag.* 14(87), 184–186.

- Rayleigh, L. 1879. "On the capillary phenomena of jets". *Proc. R. Soc. London*. Vol. 29. 196-199, pp. 71-97.
- Ren, H. & Wu, S.-T. 2010. Optical switch using a deformable liquid droplet. *Opt. Lett.* 35(22), 3826-3828.
- Riboux, G. et al. 2011. Whipping instability characterization of an electrified visco-capillary jet. *J. Fluid Mech.* 671, 226-253.
- Roux, J. M., Achard, J. L., & Fouillet, Y. 2008. Forces and charges on an undeformable droplet in the DC field of a plate condenser. *J Electrostat* 66(5), 283-293.
- Saville, D. A. 1997. ELECTROHYDRODYNAMICS: The Taylor-Melcher Leaky Dielectric Model. *Annu. Rev. Fluid Mech.* 29(1962), 27-64.
- Schober, A. et al. 1993. Accurate high-speed liquid handling of very small biological samples. *BioTechniques* 15, 324-329.
- Song, B & Springer, J. 1996. Determination of Interfacial Tension from the Profile of a Pendant Drop Using Computer-Aided Image Processing2. Experimental. *J. Colloid Interface Sci.* 184, 77-91.
- Steijn, V. VAN et al. 2013. Block-and-break generation of microdroplets with fixed volume. *Biomicrofluidics* 7(2), 1-8.
- Stone, H. A., Stroock, A. D., & Ajdari, A. 2004. Engineering flows in small devices: microfluidics toward a lab-on-a-chip. *Annu. Rev. Fluid Mech.* 36, 381-411.
- Strani, M. & Sabetta, F. 1988. Viscous oscillations of a supported drop in an immiscible fluid. *J. Fluid Mech.* 189, 397-421.
- Strani, M. & Sabetta, F. 1984. Free vibrations of a drop in partial contact with a solid support. *J. Fluid Mech.* 141, 233.
- Sutanto, E. et al. 2012. A multimaterial electrohydrodynamic jet (E-jet) printing system. *J. Micromech. Microeng.* 22(4), 045008.
- Taylor, G. 1969. Electrically Driven Jets. *Proc. R. Soc. London A* 313(1515), 453-475.
- Taylor, G. 1964. "Disintegration of water drops in an electric field". *Proc. R. Soc. London A*. Vol. 280. 1382. The Royal Society, pp. 383-397.
- Theriault, T. P., Winder, S. C., & Gamble, R. C. 1999. Application of ink-jet printing technology to the manufacture of molecular arrays. *DNA Microarrays: A Practical Approach*, 101-119.
- Tisone, T. C. 1998. Dispensing systems for miniaturized diagnostics. *IVD Technology* 4, 40-46.
- Tran, S. B. Q. et al. 2011. Semianalytical study of hemispherical meniscus oscillation with an anchored edge on a conductive flat plate under an ac electric field. *Phys. Fluids* 23(2), 022006.
- Tsakonas, C. et al. 2014. Electric field induced deformation of hemispherical sessile droplets of ionic liquid. *J Electrostat* 72(6), 437-440.

- Udey, R. N., Jones, A. D., & Farquar, G. R. 2013. Aerosol and Microparticle Generation Using a Commercial Inkjet Printer. *Aerosol Sci. Technol.* 47(4), 361–372.
- Utada, A. S. et al. 2007. Dripping, Jetting, Drops, and Wetting: The Magic of Microfluidics. *MRS Bulletin* 32(09), 702–708.
- Utada, A. et al. 2005. Monodisperse double emulsions generated from a microcapillary device. *Science* 308(5721), 537–541.
- Vancauwenberghe, V., Di Marco, P., & Brutin, D. 2013. Wetting and evaporation of a sessile drop under an external electrical field: A review. *Colloids Surf., A* 432, 50–56.
- Vladisavljević, G. T. 2015. Recent advances in the production of controllable multiple emulsions using microfabricated devices. *Particuology*.
- Wallace, D. B. 1989. Automated electronic circuit manufacturing using ink-jet technology. *Trans. ASME J. Electronic Packaging* 111, 108–111.
- Wang, Y. et al. 2012. Electrospray cone-jet breakup and droplet production for electrolyte solutions. *Europhys. Lett.* 99(6), 64003.
- Wohlhuter, F. K. & Basaran, O. A. 1992. Shapes and stability of pendant and sessile dielectric drops in an electric field. *J. Fluid Mech.* 235, 481–510.

